ION BEAM ANALYSIS OF NOVEL MATERIALS AND DEVICES INVOLVING SILICON CARBIDE AND BISMUTH SELENIDE

by

CAN XU

A Dissertation submitted to the

Graduate School-New Brunswick

Rutgers, the State University of New Jersey

In partial fulfillment of the requirements

For the degree of

Doctor of Philosophy

Graduate Program in Physics and Astronomy

Written under the direction of

Torgny Gustafsson

And approved by

_____

_____

_____

_____

_____

New Brunswick, New Jersey

October, 2015

ABSTRACT OF THE DISSERTATION

ION BEAM ANALYSIS OF NOVEL MATERIALS AND DEVICES INVOLVING SILICON CARBIDE AND BISMUTH SELENIDE

By CAN XU

Dissertation Director:

Torgny Gustafsson

The properties of single crystals, thin films and their surfaces and interfaces have a critical impact on the electrical performance of devices. Analysis of the crystallinity of single crystals, the composition of thin films, surface and interface defects greatly assist the improvement of devices. Ion beams is a unique probe that provides quantitative measures of those properties. In this dissertation, ion beam techniques including Medium Energy Ion Scattering (MEIS), Rutherford Backscattering Spectrometry (RBS), Nuclear Reaction Analysis (NRA) and Helium Ion Microscopy (HIM) are used to analyze silicon carbide and bismuth selenide based structures.

The 4H polytype of silicon carbide (SiC) is a promising candidate for high temperature and high power metal-oxide-semiconductor device applications due to its wide bandgap. In such applications high quality surfaces and interfaces are critical. Aspects of surface quality can be determined by backscattering spectrometry with ion channeling, where the channeling energy loss spectrum depicts the surface peaks of the crystal. We find that the SiC surface peaks are in good agreement with theoretical predictions, when including correlations of the thermal vibrations of the atoms.

Hydrogen passivation of interface defects by annealing in H_2 is a well-established process in silicon technology. Unfortunately this process is not effective in silicon carbide based structures. Another way of inducing hydrogen at the interface is through water vapor exposure. Nuclear Reaction Analysis (NRA) is used to measure the deuterium content in the SiC/SiO_2 system induced by heavy water (D_2O) anneal. Deuterium uptake in Si/SiO_2, $SiC(0001)/SiO_2$, $SiC(000\text{-}1)/SiO_2$ and $SiC(11\text{-}20)/SiO_2$ are being compared and the amount of deuterium at the interface is correlated with the electrical properties.

The structure and chemical compatibility of In_2Se_3 (a band insulator) and Bi_2Se_3 (a 3D topological insulator) suggests possible promising applications of $In_2 Se_3/Bi_2Se_3$ devices. Indiffusion of indium into Bi_2Se_3 will affect the transport properties. We have grown In_2Se_3/Bi_2Se_3 thin films on sapphire by Molecular Beam Epitaxy at different temperatures and correlated the indium diffusion with growth temperature and mobility.

DEDICATION

To my beloved family and friends

献给我的父母

ACKNOWLEDGEMENT

I am grateful to all those beloved people I met in the long way to my Ph.D. They make my life at Rutgers a joy and will be a wonderful memory in the rest of my life. I would not be able to stay here and finish my work without their kindness help, both in academia and personal life.

I own the deepest appreciation to my thesis advisor, Professor Torgny Gustafsson. His support and extreme patience make the group a family. My research work is really motivated not only by the amazing science but also the enjoyable work environment. I still remember the first day I met him when I were a fresh undergraduate who was afraid of life in America. It was the kindly smile on his face that gave me the courage to start my Ph.D. life. I do not remember how many times I came out from frustration because of his warm voice. His guidance on the research especially on ion beam analysis arise my interests in this field and supports me all the way to today. He read and corrected every single sentence in this thesis and commented on gramma and science. I really do not know what else to ask for from an advisor.

The same appreciation should be given to my unofficial advisor, Professor Leonard C. Feldman. He introduced me to the silicon carbide field. He is the man who really enjoys science and has the passion to analysis data, look up reference and calculate with a pen and a piece of paper for many hours out of his fully filled schedule. His passion and attitude to work set up a model for me.

I own many thanks to Professor Eric Garfunkel. He brings the physics, chemistry and engineering group together for us to get exposed to new fields and ideas.

I am grateful to the committee members at Rutgers, Professor Seongshik Oh, Professor Natan Andrei and Professor Steve Schnetzer for interest in my work and valuable comments. Professor Seongshik Oh gave lots of nice ideas on Bi_2Se_3. Professor Steve Schnetzer gave me a nice lecture on quantum mechanics. Professor Natan Andrei gave nice discussions in solid state physics.

I would like to thank Dr. Matt Copel for kindly agreeing to be my outside committee member. His excellent work on ion scattering brought us many new ideas.

I own much thanks to the ion beam group members for the wonderful work environment and friendship. Dr. Tian Feng and Dr. Hangdong Lee taught me every detail about the Medium Energy Ion Scattering machine. Many projects could not be done without the nice discussions and help from Dr. Hangdong Lee. I thank Dr. Samir Shubeita for the discussion of vibration. They are not only my teachers in the academia but also my older brothers in my personal life.

The same appreciation is to the silicon carbide group members. Dr. Yi Xu and Dr. Gang Liu taught me everything about silicon carbide material and devices. Dr. Yi Xu helped me on the X-ray photoelectron spectroscopy. Dr. Gang Liu taught me device fabrication and I-V, C-V measurements. They are also my real friends in every aspect who make the long Ph.D. life colorful.

I want to thank the group members. Dr. Hao Wang, Mr. Slava Manichev, Dr. Voshadhi Amarasinghe, Dr. takane kobayashi and Mr. eduardo pitthan for the discussions and nice work. I am especially grateful to Dr. Boris Yakshinskiy for the great Nuclear Reaction and RBS measurement.

I thank the Bi_2Se_3 group members, Dr. Matthew Brahlek and Mr. Nikesh Koirala for their great expertise in topological insulators.

I thank Professor Ronald Gilman, Shirley Hinds, Nancy Pamula and Gwen Chupka for their great assistance in the department. Bill Schneider and his team at the machine shop made high quality parts. Yuri Streltsov solved the electronics problems.

I would also like to thank my fellow graduate students, Wenhu Xu, Yuanjun Zhou, Wei Dai, Xueyun Wang, Bin Gao, Feixiang Luo and Aleksandra Biedron. They make my life in Rutgers fun.

Last but not the least; my greatest appreciation is to my parents. They want to see me every single day but they never complained that I spent 6 years in another half of the earth and last time I visited them was almost 4 years ago. I also thank my girlfriend for every day we are together, happy or frustrated.

I do think I am blessed to know so many nice people. My time at Rutgers is a great joy with all of them.

Table of Contents

List of figures

List of tables

List of acronyms

AFM	Atomic Force Microscope
MBE	Molecular Beam Epitaxy
MCP	Micro Channel Plate
MEIS	Medium Energy Ion Scattering
MOSCAP	Metal Oxide Semiconductor (MOS) Capacitor
MOSFET	Metal Oxide Semiconductor Field Effect Transistor
NRA	Nuclear Reaction Analysis
RBS	Rutherford Backscattering Spectroscopy
SRIM	Stopping and Range of Ions in Matter
TI	Topological Insulator
u.c.	unit cell
XPS	X-ray Photoelectron Spectroscopy

Chapter 1 introduction

1.1 General introduction

This thesis focus on surface and interface analysis of novel materials including wide band gap semiconductor SiC and topological insulator (TI) Bi_2Se_3. Various elemental and structural analysis techniques are used to study SiC and Bi_2Se_3 based structures and the physical analyses are correlated to electrical performance of the devices.

This dissertation is organized as follows:

Chapter 1 includes a general introduction of the background of surface science, applications of SiC wide band gap semiconductors and an overview of topological insulators. Chapter 2 discusses Medium Energy Ion Scattering (MEIS) which is used to study the distribution of surface and interface atoms. Chapter 3 is devoted to a study of SiC crystals with MEIS channeling. From our channeling data of the surface peak we obtain results for the surface vibrational amplitudes. Chapter 4 discusses the effect of water annealing on SiC MOSCAP. We measure the physical distribution of deuterium induced by heavy water annealing with nuclear reaction analysis (NRA). The deuterium content is correlated with capacitance-voltage (C-V) measurements. In chapter 5 we analyze the In_2Se_3/Bi_2Se_3 interface using MEIS in an attempt to determine the extent of indium diffusion into Bi_2Se_3 and the indium content is correlated with the electron mobility in in the Bi_2Se_3 layer.

1.2 A brief discussion of surface and interface science

Surface science is a branch of solid state physics. The goal of solid state physics is to understand the macroscopic properties of solid such as mobility, heat transfer or magnetism based on the behavior and interactions of individual atoms. A problem of understanding solid is that a solid contains many atoms, ~$10^{23}/cm^3$. It is technically impossible to solve quantum or classical equations of so many atoms. The way out is make use of the fact that many solids are periodic which greatly assists the solution of this problem. The existence of surface breaks the symmetry of the solid in the direction perpendicular to the surface. Therefore, it could lead to new properties that are sometimes different from those of the bulk. Physically, the atoms at the surface have fewer neighbor atoms to bond with than the bulk atoms. This gives rise to various types of surface phenomena. The "surface" in this thesis is the top few layers of atoms affected by the existence of the boundary.

To minimize the energy, the atoms at the surface have to re-order themselves to compensate the change of the binding states. This leads to surface relaxation or reconstruction. Chapters 3 and 4 of this thesis discuss the materials properties of SiC and devices.

There are many applications that can benefit from a study of surface science. One that has motivated this thesis is the application of surface science on semiconductor device fabrication. To make devices at lower cost and higher performance, their size has to shrink following Moore's law. Cutting edge semiconductor devices are today at the

10nm range and are approaching 7nm technology. As the lateral scale of the devices decreases, the ratio of the surface size to that of the bulk is higher and change from bulk to surface devices. The MOSFET is one of the most important surface devices. When the MOSFET is turned on, the carriers in the MOSFET flow in a channel at the surface of the semiconductor. Therefore, the properties of the surface are critical.

For most of the surface science studies, Ultra High Vacuum (HUV) with a chamber pressure better than 10^{-10} torr is required to keep a stable surface free from contamination.

Many surface properties can be characterized nowadays with surface analysis techniques. Probes to characterize the surface are usually electrons (LEED, SEM et al.), ions (RBS, MEIS, HIM) and X-ray (XPS). The following is a list of most of the surface analysis techniques used in this thesis research.

X-ray photoelectron spectroscopy (XPS) is a surface sensitive technique used for quantitative elemental information and for determining binding states. XPS spectra are obtained by irradiating X-ray on the target and measuring the intensity and kinetic energy of electrons generated by the X-ray. The electron binding energy is determined by the equation 1.2.1.

$$E_{binding} = E_{photon} - (E_{kinetic} + \varphi) \qquad \text{Equation (1.2.1)}$$

In which $E_{binding}$ is the binding energy of the electron, E_{photon} is the energy of the X-ray, $E_{kinetic}$ is the kinetic energy of the emitted electrons and φ is the work function of the material. A monochromatic aluminum K-alpha X-ray of energy 1486.7eV is used in this

work and the energy resolution is 0.2-0.4eV. The electrons generated usually has low energy and short attenuation length. The Si $2p_{3/2}$ photoelectron attenuation length in SiC is calculated to be 2.2nm [1]. This makes XPS analysis extremely surface sensitive.

Rutherford backscattering spectroscopy (RBS) gives quantitative elemental analysis for thin films from a few tens of nanometer to a few micron meter. A high energy ion beam (usually 2MeV He^+) is the probe and the backscattered ions are detected and energy analyzed. The energy for a backscattered He+ ion is related to the mass of the species in the film, which gives RBS mass specific sensitivity. The number of back scattered particles is proportional to the areal density. Detailed calculations are in chapter 2.

Medium energy ion scattering (MEIS) is a lower energy version of RBS and is an advanced technique for thin and ultra-thin film analysis. Chapter 2 is a detailed discussion about MEIS.

Nuclear reaction analysis (NRA) measures quantitative content and depth profile. It relies on the nuclear reaction of the incident particles and the target atoms. It is discussed in detail in chapter 4.

Helium ion microscopy (HIM) provides an image of the surface of the sample by scanning it with a focused (~0.5nm) He^+ 30 keV beam. When the beam interacts with the target secondary elections are generated and collected by a detector. Its advantage over SEM is in imaging insulating samples without a deposited metal layer. Also, a helium ion beam has a higher secondary electron yield than that of an electron beam [2].

In this thesis, those physical surface analysis methods are combined with electrical measurements to study how the surface and the interface properties and change in these would affect device electrical performances.

1.3 Basics of MOSFETs

Figure 1.3.1 is the basic MOSFET structure. It is composed of a gate layer, a gate oxide and a semiconductor body. The gate is usually a metal or polysilicon. The source and drain region in a n-channel MOSFET is highly doped n+ Si while the semiconductor is regular doped p-type. The most widely used semiconductor substrate is silicon due to the low cost. Another advantage of using Si as substrate is its native oxide SiO_2. The Si/SiO_2 interface has very few electrical defects. The band alignment of SiO_2 and Si form a high enough energy barrier to prevent electrons from tunneling through. However, the maximum working temperature for standard commercial Si based devices is 150^o [3]. For higher temperature applications, wide band semiconductor devices are needed. In chapter 3 and chapter 4 of this thesis, SiC as a wide band gap semiconductor substrate is discussed. One of the important advantage of SiC over other wide bandgap candidates is that its native oxide is SiO_2, just as that of Si. Therefore the SiC device processing is similar to that of Si.

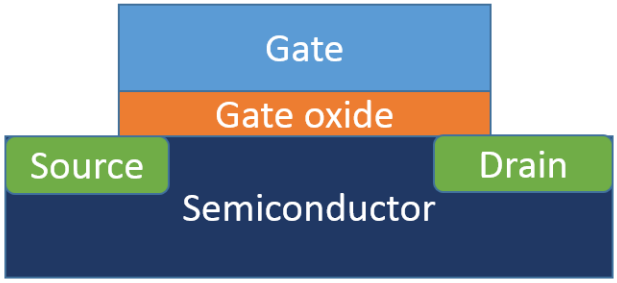

Figure 1.3.1, schematic of a MOSFET structure.

The MOSFET is used as a switching device. The device ON/OFF state is controlled by the gate voltage V_G. When V_G is zero, the source, the substrate and the drain form an n-p-n junction that electrons cannot tunnel through. This is the OFF state of an n-channel MOSFET. When V_G is applied, it generates a potential across the oxide and electrons in the semiconductor are attracted to the semiconductor/oxide interface. When V_G reaches the threshold value V_t, the near interface semiconductor layer becomes n-type due to the electrons attracted by V_G. A current I_D can then flow between source and drain driven by a voltage across them. This is the device ON state. The near interface layer inverts from a p-type to an n-type in the ON state, and this is referred as the inversion channel. In a SiC MOSFET, the SiO_2/SiC interface is not abrupt. The dangling bonds and defects near the interface act like electron traps [4]. Therefore the electron channel mobility in a SiC based MOSFET is low. A detailed discussion of this issue and its solution is discussed in chapter 4.

1.4 Advantages of SiC devices

Si has been and will continue to be the dominant semiconductor substrate. In some applications, devices have to work at high switch speed and high voltage up to 20kV. In such conditions, Si based devices are too bulky and inefficient [5]. The main approach to this application is to use a wide band gap (WBG) semiconductor. SiC have a band gap of 3.2eV which is almost 3 times of that of Si, and critical field of 2.0MV/cm which is about 7 times of that of Si. This allows SiC to be fabricated in much thinner layers than Si devices. The device ON state resistance is inversely proportional to the critical field cubed [6]. Therefore the high critical SiC field results in a lower ON resistance and lower power loss. In addition, the ON-OFF switch delay time is proportional to the depletion layer width of a diode which can be short when the critical field is high. As a result, SiC based power devices switch much faster than Si based power devices. SiC Schottky barrier diodes have been commercialized by Cree and Infineon in 2001 and can sustain 600V[7]. 1.2 kV SiC MOSFETs became available in early 2011 from Cree. Those devices have lower ON state resistance and faster switch speed. A more detailed discussion about SiC material and devices is in chapter 4.

1.5 Introduction of topological insulators

The work in chapter 5 involves topological insulators. Topological insulators are a new class of materials that recently have been a hot topic in condensed matter. They are of the interests because of its electrically insulating bulk states and the exotic conducting surface states [8, 9]. The surface states are protected by the time reversal symmetry. Its

strong spin-orbital coupling makes the spin of the surface electrons correlated with their momentum. More importantly, transport of the electrons on the surface is immune to non-magnetic impurities because those impurities cannot change the spin. Therefore impurities on the surface cannot scatter electrons 180 degrees. This property could be useful for spintronic applications [9].

Topological insulator based functional devices are of current interest. The most obvious application of topological insulator is that its high surface mobility enables energy efficient devices with low joule heating. The topological protection reduces the electron backscattering and small angle scattering can theoretically be further reduced by fabricating topological insulators to 1D channels [10]. Interfacing topological insulators with superconductors creates Majorana fermions [11](a fermion that its antiparticle is itself) which may help the development of quantum computers. Topological insulator is also a good candidate for thermoelectric devices. The performance of thermoelectric devices is measured by the ratio of the electrical conductivity (affected by the surface of the topological insulator) and the thermal conductivity (a bulk property) [12]. Those two are decoupled in the topological insulator.

References

1. Xu, Y., *Structure and chemistry of defect passivation at the interface between silicon oxide and silicon carbide*, in *Chemistry and Chemical Biology*. 2014, Rutgers University.
2. Ramachandra, R., B. Griffin, and D. Joy, *A Study of Helium ion induced Secondary Electron Emission.* Microscopy and Microanalysis, 2008. **14**(SupplementS2): p. 1192-1193.
3. Willander, M., M. Friesel, Q.-u. Wahab, and B. Straumal, *Silicon carbide and diamond for high temperature device applications.* Journal of Materials Science: Materials in Electronics, 2006. **17**(1): p. 1-25.
4. Casady, J.B. and R.W. Johnson, *Status of silicon carbide (SiC) as a wide-bandgap semiconductor for high-temperature applications: A review.* Solid-State Electronics, 1996. **39**(10): p. 1409-1422.
5. Qingchun, Z., R. Callanan, M.K. Das, R. Sei-Hyung, A.K. Agarwal, and J.W. Palmour, *SiC Power Devices for Microgrids.* Power Electronics, IEEE Transactions on, 2010. **25**(12): p. 2889-2896.
6. Zetterling, C.M. and I.o.E. Engineers, *Process Technology for Silicon Carbide Devices*. 2002: INSPEC.
7. Friedrichs, P. and R. Rupp. *Silicon carbide power devices - current developments and potential applications*. in *Power Electronics and Applications, 2005 European Conference on*. 2005.
8. Hasan, M.Z. and C.L. Kane, *Topological insulators.* Reviews of Modern Physics, 2010. **82**(4): p. 3045-3067.
9. Moore, J.E., *The birth of topological insulators.* Nature, 2010. **464**(7286): p. 194-198.
10. Chen, Y.P., *Topological insulator-based energy efficient devices.* Proceedings of the SPIE, 2012. **8373**: p. 83730B.
11. Qi, X.-L. and S.-C. Zhang, *Topological insulators and superconductors.* Reviews of Modern Physics, 2011. **83**(4): p. 1057-1110.
12. Vineis, C.J., A. Shakouri, A. Majumdar, and M.G. Kanatzidis, *Nanostructured thermoelectrics: big efficiency gains from small features.* Adv Mater, 2010. **22**(36): p. 3970-80.

Chapter 2

Medium Energy Ion Scattering

2.1 Introduction

Electronic device performance relies on the properties of thin films, surfaces and interfaces. Issues to be investigated include thermal stability, surface composition, interface reactions and the influence of defects. An experimental knowledge of these properties allows improvement in fabrication and can guide a more accurate theoretical analysis. Energetic ions provide a unique way of analyzing such systems. It can give quantitative results and are easy to control.

Medium Energy Ion Scattering (MEIS) is a variant of Rutherford backscattering spectrometry (RBS) with lower projectile energies and more complicated and higher resolution detection system [1-4]. In an MEIS experiment, ions, usually H^+ or He^+, with an energy of 100-200keV are incident on the sample target as a probe. The energies of the backscattered ions depend on the masses of the atoms in the target. The backscattered ion intensity is also related to the areal density target atoms. Ions travelling in the solid lose energy due to interaction with electrons and small angle deflection when interacting with nuclei. The energy loss is propositional to the path length. As a result, the energy of the scattered ions is also related to the depth at which the collision events happen. To summarize, the energy spectrum of the scattered ions reveals the masses of the sample atoms, the areal density of each element, and their depth distribution.

Compared with Rutherford backscattering spectrometry (RBS) with high energy ion beam in the range of 0.5~2meV, MEIS provides better energy resolution and better depth resolution thanks to its advanced detection system and the beam energy.

2.2 Principles of MEIS

2.2.1 Ion-solid interaction

For a 100keV H+ beam, the velocity of H particles is 4.4 x 10^8 cm/s, almost 2 orders smaller than c, the speed of light. Its De Broglie wave length is about 0.001Å, much smaller than the atomic spacing of solid. Therefore, neither quantum mechanics nor relativity has to be considered when modeling the MEIS ion-solid interaction. The closet approach of 100keV H^+ beam incident head-on to atoms in a Silicon nucleus in the target is ~100fm, which is larger than the sum of the nuclear radii of H^+ and Si, but smaller than the sum of their atomic radii. Two kinds of interactions therefor have to be considered: elastic collisions between the two nuclei and inelastic collisions involving the projectile and the electrons. The elastic collision opens the discussion of the k factor (2.2.2) and the cross section (2.2.3). An inelastic collision results in energy loss, which is discussed in section 2.2.4.

2.2.2 The Kinemics factor K

As discussed above, in an MEIS measurement, the mass of the target atoms is related to energy of the scattered ions. The collision processes of ions in MEIS energy range are modeled as classical elastic two body collisions. In figure 2.2.1, a particle of mass m_1 moving with kinetic energy E_0 collides with a stationary particle with mass m_2. E_1 is the final energy of the ion, and α is the scattering angle. The target atom is considered as stationary during in this process since the vibration velocity of the target atoms is negligible compared to the velocity of incident ions.

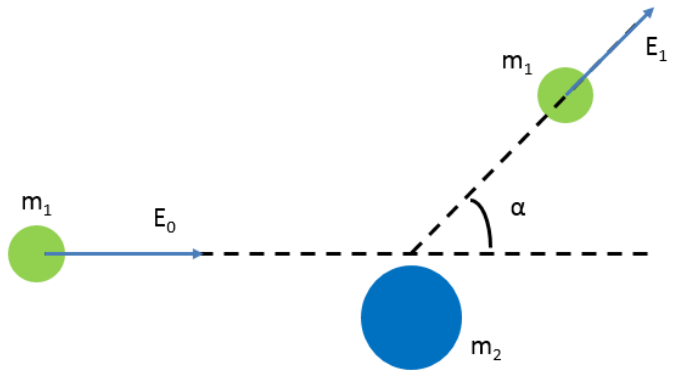

Figure 2.2.1, Two body collision. m_1 and m_2 are the masses of the incident ion and target atom, respectively. E_0 and E_1 are the initial and final energy of the ion, α is the scattering angle.

The ratio of the final energy after the collision E_1 and the initial energy E_0 is defined as the kinematic factor k. The k factor can be derived from conservation of energy and momentum.

$$k \equiv \frac{E_1}{E_0} = \left[\frac{\sqrt{m_2^2 - m_1^2 \sin^2(\alpha)} + m_1 \cos(\alpha)}{m_1 + m_2}\right]^2 . \qquad \text{(Equation 2.2.1)}$$

The k factor is a function of m_2 and α so that an ion scattering energy spectrum is actually a mass spectrum.

If a target contains two types of atoms that differ in their masses by a small amount Δm_2, to distinguish the two kinds of atoms, it is important to ensure that the difference of measured backscattered ion energy ΔE_1 is large enough to resolve the two masses. Quantitatively,

$$\Delta E_1 = E_0 \left(\frac{dk}{dm_2}\right) \Delta m_2 \qquad \text{(Equation 2.2.2)}$$

In a backscattering event, usually $m_2 >> m_1$. Equation 2.2.2 is then further reduced to [3]

$$\Delta E_1 = E_0 [4 - (\pi - \alpha)^2] \left(\frac{m_1}{m_2^2}\right) \Delta m_2 \qquad \text{(Equation 2.2.3)}$$

Mathematically, from equation 2.2.3, several parameters can be adjusted to improve ΔE_1 for a better mass resolution:

1) Increase E_0, energy of the incident ions.
2) Use heavier incident ions (larger m_1). A He^+ beam is often used in ion beam spectroscopy for better mass resolution.
3) Make the scattering angle close to 180^o. However, in a real backscattering setup, it is impossible to make 180^o scattering angle because of physical limitations. In our MEIS system, the maximum scattering angle is 135^o due to the size of the detection system.
4) The mass resolution is better for light target elements (small m_2).

2.2.3 cross section **σ**

The Cross section is the probability that a collision contributes to a detected backscattered particle. In an ion scattering experiment, a total dose of Q ions incident on a target with volume density of N and thickness t. The number of ions detected is then

$$Y = \sigma Q(Nt) \qquad \text{(Equation 2.2.4)}$$

The total beam dose Q is counted with a mesh in from of the sample; to measure the areal density Nt of certain element from the detected yield Y, a quantitative calculation of the cross section is required.

The Cross section has the units of area. A simple explanation of cross section is taking it as a small area on each nucleus, and every small area does not overlap. A projectile ion impinging on this area will result in a collision that generates a count in the detector. Given the interaction potential, the differential cross section can be calculated. As discussed above, in the MEIS beam energy range, the differential cross section using the Coulomb potential is:

$$\left(\frac{d\sigma}{d\Omega}\right) = \left[\frac{Z_1 Z_2 e^2}{4E\sin^2\left(\theta/2\right)}\right]^2 \qquad \text{(Equation 2.2.5)}$$

This expression is in center of mass coordinates. Here Z_1 and Z_1 are atomic number of projectile atoms and target atoms respectively; E is energy of projectile atom before interaction; $d\Omega$ is the area of the detector corresponding to the differential cross section.

From equation (2.2.5) [5]:

1) The differential cross section is proportional to Z_1^2 and Z_2^2. So that ion scattering

method is more sensitive to heavy elements, with heavy projectile ions.

2) The cross section is inversely proportional to E_0^2. So that the detected yield increases as incident energy decrease.

3) The cross section is proportional to $\sin^{-4}\left(\frac{\theta}{2}\right)$. At angles close to 180°, backscattering is more effective.

Differential cross section in lab frame can be expanded if $m_1 << m_2$ to the following series:

$$\frac{d\sigma}{d\Omega} \approx \left(\frac{Z_1 Z_2 e^2}{4E}\right)^2 \left[\sin^{-4}\left(\frac{\theta}{2}\right) - 2\left(\frac{m_1}{m_2}\right)^2 + \cdots\right] \qquad \text{(Equation 2.2.6)}$$

The cross section, more precisely, average cross section, is the average of differential cross section over the entire detector with solid angle Ω:

$$\sigma \equiv (1/\Omega) \int \left(d\sigma/d\Omega\right) d\Omega \qquad \text{(Equation 2.2.7)}$$

The previous calculations are based on the Coulomb potential. In our MEIS system, the energy of the incident particles is in the range of hundreds of keV. Ions in this energy range cannot reach the target nuclei so that the screening effect by the inner shell electrons must be taken into consideration. Screened Coulomb potentials have been derived as [6]:

$$V = \frac{Z_1 Z_2 e^2}{r} \phi\left(\frac{r}{a}\right) \qquad \text{(Equation 2.2.8)}$$

where $\phi\left(\frac{r}{a}\right)$ is the screening function and a is the screening length. In the Molière potential, the screening function and screening length are:

$$\phi(x) = 0.35e^{-0.3x} + 0.55e^{-1.2x} + 0.10e^{-6.0x}$$

$$a = \frac{0.8853 a_0}{(\sqrt{Z_1}+\sqrt{Z_2})^{2/3}} \qquad \text{(Equation 2.2.9)}$$

The screened cross section is then:

$$\frac{\sigma}{\sigma_R} = \frac{1}{1+\frac{V_1}{E}} \qquad \text{(Equation 2.2.10)}$$

In which V_1 can be estimated as the magnitude of the decrease in the potential energy due to screening, which is estimated by the first term in the Taylor series of equation (2.2.8)

$$V_1 = \frac{Z_1 Z_2 e^2}{a}\dot{\phi}(0) \qquad \text{(Equation 2.2.11)}$$

For 100 keV protons incident upon Al and Au, V_1 is of the order of 1 and 10 keV, respectively.

2.2.4 Electronic Energy loss

In an ion scattering experiment, only a small portion of the ions are elastically scattered from the nuclei. As the cross section for large angle scattering is small, more than 90% of the incident particles penetrate into the solid. As particles penetrate into the target, they lose energy due to excitation and ionization in inelastic collisions, The energy loss ΔE in the distance Δx that the ions travel in the target depends on the mass of the incident ion, its energy, and the target properties. Microscopically, the energy loss due to excitation and ionization of the target electrons is a discrete process. Macroscopically, as the energy losses are small compared to those corresponding to a backscattering event, it is a good assumption that the moving ions lose energy continuously.

Theoretically, the energy loss has 2 regimes, fast collisions and slow collisions. The critical velocity is the mean orbital velocity of the atomic or molecular electrons in the shell or sub shell of a given target atom. In the fast collision case, the velocity of the incident particles is much greater than that of the orbital electron of the target. The collision produces a sudden transfer of energy from the projectile to the target electron. The stopping cross section decreases with increasing velocity because the particle spends less time in the vicinity of the atoms. In the slow collisions, the velocity of the projectiles is not enough to completely strip elections off from them. Therefore the average charge of the projectile becomes lower, resulting in less electron excitation. It is found that the stopping power is proportional to the velocity when the incident particles travel slower than the critical velocity. Due to the two competing processes, the energy loss has a maximum value at an intermediate energy. Figure 2.2.2 [3]shows the energy loss dE/dx as a function of incident energy for H and He in Al. The maximum energy loss for H^+ and He^+ beam is at the energy range of few hundreds keV. MEIS requires beam energy in this range for the best energy resolution.

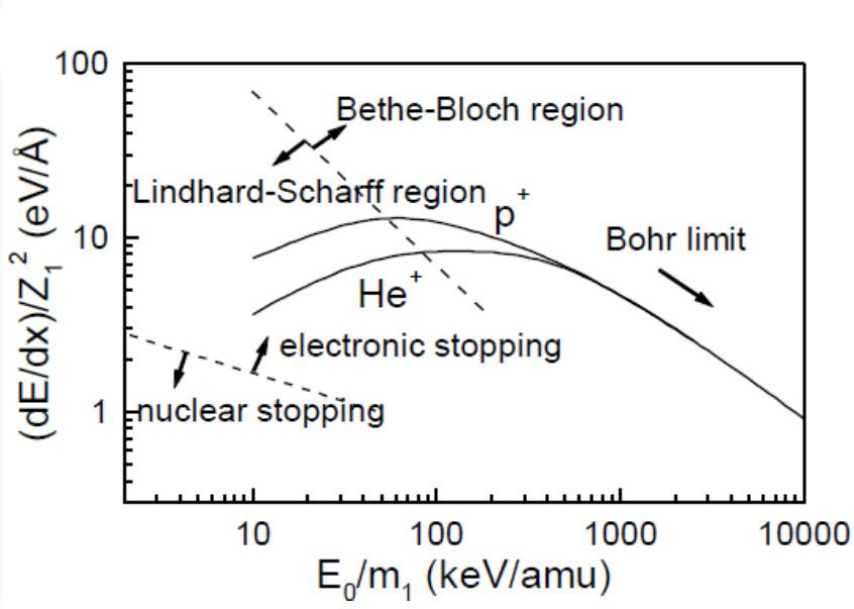

Figure 2.2.2 [3] The energy loss rate for H^+ and He^+ ions in Al.

Bethe-Bloch-formula gives an expression of stopping which agrees with experiment well in energy beyond the maximum of the dE/dx curve, that is to say, a fast collision condition:

$$\frac{dE}{dx} = NZ_2(Z_1e^2)^2 f(E/m_1) \quad \text{(Equation 2.2.12)}$$

Where $f(E/m_1)$ is a function that depends only on the target elements. From the formula, dE/dx is proportional to the density N, to Z_1^2, and to Z_2. The Bethe-Bloch-formula implies some useful results, but it is not a microscopic expression. Electronic stopping depends on the electronic configuration of the target atoms. Chemical bonds should also contribute to the stopping process. These effects are ignored in The Bethe-Bloch formula.

At fast collisions, the incident particle is effectively stripped off electrons. However, as the projectile particle slows down, the probability that electrons are captured by the moving ions increases, and its effective charge decreases. As a result, dE/dx increases less rapidly with decreasing energy. When the velocity of the incident particle is less than a critical velocity, dE/dx decreases with falling E as the probability of electron capture by the ions increases. In this energy range, called The Lindhard-Scharff region, the electronic energy loss becomes proportional to the velocity of the incident particles. Ions also transfer energy to the nuclei of the solid through small angle scattering events. This component contributes to the total energy loss is called the nuclear energy loss.

The nuclear energy loss is much smaller than the electronic loss. It becomes another major component of the energy loss only at very low energies. For H and He as projectiles, the nuclear stopping is negligible everywhere except at the very end of the projectile range in the material.

Accurate calculation of the stopping cross sections from theory is difficult. Lots of possible interactions can take place during the ion path in the material. The most trustworthy values of dE/dx are therefore from experimental data.

In thin film analysis, it is reasonable to assume that the energy loss is proportional to the path length. The energy of a particle penetrates into a depth t is

$$\mathrm{E(t)} = E_0 - (\mathrm{dE/dx})_{\mathrm{in}}\ \Delta \mathrm{t} \qquad \text{(Equation 2.2.13)}$$

where E_0 is the initial energy of the ions, $\mathrm{dE/dx}$ is the energy loss rate and Δt is the path length from the surface.

The energy loss process contains three portions as shown in Figure 2.2.3. The energy loss during the incoming path ΔE_{in}, the energy transfer due to elastic collision ΔE_s and the energy loss in the outgoing path $\Delta E_{out.}$ Assuming normal incidence, the energy of ions scattered from the depth t is:

$$\mathrm{E_1(t)} = \mathrm{KE(t)} - \frac{\mathrm{t}}{|\cos\theta|}\left(\frac{\mathrm{dE}}{\mathrm{dx}}|_{\mathrm{out}}\right) = \mathrm{KE_0} - \mathrm{t}(\mathrm{K(dE/dx)_{in}}\ + \frac{1}{|\cos\theta|}(\mathrm{dE/dx})_{\mathrm{out}})$$

(Equation 2.2.14)

The depth information is obtained from the exiting energy. The deeper an atom is, the lower an energy it will appear at in the energy spectrum. Backscattering energy spectrum is a depth profile because of quantitative understanding of energy loss.

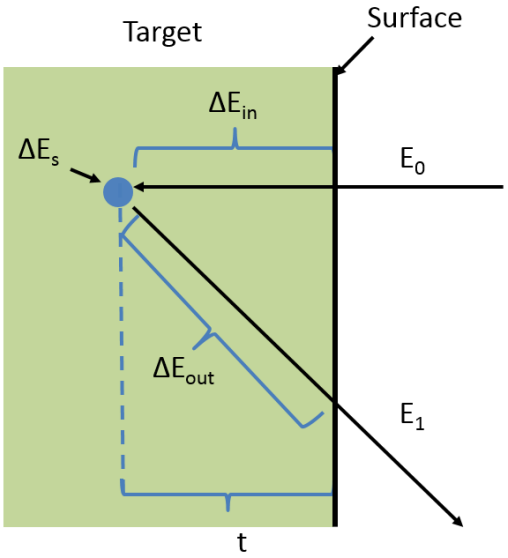

Figure 2.2.3 The Energy loss process. ΔE_{in} is energy loss before collision with target, ΔE_{out} is energy loss after backscattering. ΔE_s is energy loss when during collision which is equal to $(1-k)E_t$ assuming normal incidents.

2.2.5 Depth Resolution and Energy-Loss Straggling

Incident particles lose energy when passing through a target because of inelastic collisions. This process, even considered above as continuous, is determined by many individual encounters. The number of collisions is large, so statistical fluctuations must be taken into account in the stopping process. That is to say, identical particles with identical energy may not lose the same energy after passing through target with thickness Δt. This phenomenon is called energy straggling. It sets a limit on depth resolution, as it broadens the energy distribution of both the incoming and outgoing

ions. The dominant contribution to energy straggling is the statistical fluctuations in these electronic interactions. The distribution of energy loss ΔE for many particles is approximately Gaussian. In the Gaussian region, the probability of finding an energy loss ΔE±dE is:

$$\mathrm{P(dE)} = \exp\left[-\mathrm{dE}^2/2\Omega_\mathrm{B}^2\right]/(2\Omega_\mathrm{B}^2\pi)^{\frac{1}{2}} \qquad \text{(Equation 2.2.15)}$$

Where ΔE is the mean of the energy loss, dE is a small deviation from ΔE and Ω_B^2 is the variance of the energy loss. The variance is also referred as the energy straggling. Bohr derived an expression for Ω_B^2, the mean square derivation. Bohr value of energy straggling is:

$$\Omega_\mathrm{B}^2 = 4\pi \mathrm{Z}_1^2 \mathrm{e}^4 \mathrm{N Z}_2 \mathrm{t} \qquad \text{(Equation 2.2.16)}$$

Bohr's theory predicts that straggling does not depend on the energy of the incident particle.

Chu et al, estimated the energy straggling as a function of energy loss [5]:

$$\Omega_B/\Delta E = (\bar{E}\,/\Delta E)^{1/2} \times 10^{-2} \qquad \text{(Equation 2.2.17)}$$

With this expression, when a 2MeV He ion pass through a target and lose 200keV, the standard deviation of the energy loss is 6.3keV.

The above discussion is based on the assumption of fully ionized incident particles with energies in the MeV range. However, in the MEIS regime, the ion energy is few hundred keV. In this energy range, the projectile velocities are roughly comparable with the electronic velocities. For this region, the fully ionizated assumption needs to be corrected. The local electronic density and the velocity distribution of the electrons must be taken into account. Using the Thomas-Fermi model, Lindhard and Scharff

extended Bohr's treatment. Their result is expressed in terms of the Bohr straggling as [7]:

$$\frac{\Omega^2}{\Omega_B^2} = \begin{cases} \frac{1}{2}L(y), y \leq 3 \\ 1, y > 3 \end{cases} \qquad \text{(Equation 2.2.18)}$$

$$y = \frac{\left(\frac{v}{v_0}\right)^2}{Z_2} \qquad L(y) = 1.36y^{1/2} - 0.016y^{3/2}$$

Energy straggling sets a finite limit to energy resolution. The energy resolution is normally composed of two contributions: the detector resolution δEd and the energy straggling δEs. If the two contributions are independent, the total resolution, δE, is given by

$$(\delta E)^2 = (\delta E_d)^2 + (\delta E_s)^2 \qquad \text{(Equation 2.2.19)}$$

Assuming normal incidence, the limitation to the depth resolution δt in the backscattering spectrometry is given by the equation

$$\delta t = \frac{\sqrt[2]{(\delta E_d)^2 + (\delta E_s)^2}}{K(dE/dx)_{in} + \frac{1}{|\cos\theta|}(dE/dx)_{out}} \qquad \text{(Equation 2.2.20)}$$

For a given detector energy resolution, the depth sensitivity is optimum by maximizing the energy loss associated with scattering from a given depth into the sample [8]. In general, this is done by grazing-angle techniques so that the path length and hence the energy loss is the maximum.

2.2.6 Channeling

Channeling of energetic ions occurs when the beam is carefully aligned with a major symmetry direction of a single crystal. Atomic rows and planes will steer energetic ions along the channels between rows and planes. The steering action is effective and can

lead to hundredfold reduction in the yield of backscattered particles [4]. Figure2.2.4 (adopted from reference [3])shows a side view of this process in which most of incident particles go through a channel formed by rows of atoms. Channeled particles cannot get close enough to the atomic nuclei; hence, scattering from the substrate is drastically reduced.

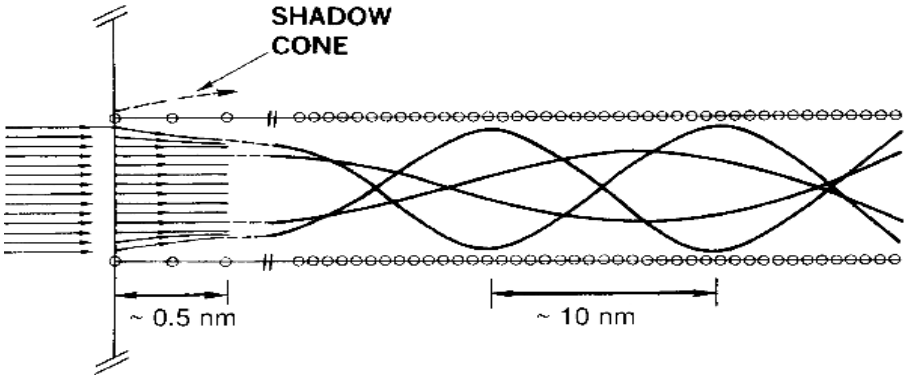

Figure 2.2.4 (adopted from reference [3]) Side view of incident particles scattering at surface and channeling inside crystal.

There is always full interaction with the first monolayer of the target. Figure 2.2.5 (adopted from reference [9]) shows the deflection of ions from the first atom along the row leads to formation of a shadow cone, thereby greatly reduce the chance of scattering from deeper atoms [9].

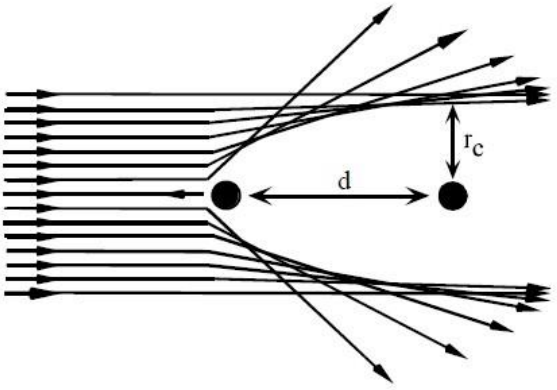

Figure 2.2.5 (adopted from reference [9]) Shadow cone formed by the first atom in an atom row.

However, the process of channeling is not perfect due to surface rearrangement and thermal vibration. A useful parameter to evaluate the shadow effect is to compare the shadow cone radius (r_c in figure 2.2.5) to the vibration amplitudes of the atoms. A simple expression for r_c for the bare Coulomb interaction is [10]:

$$r_c = 2\sqrt{\frac{Z_1 Z_2 e^2 d}{E}} \qquad \text{(Equation 2.2.21)}$$

The ratio of shadow cone radius and vibration amplitude is a measure of how much the atoms under the surface layer contribute to the backscattering signal. This part is discussed in detail in chapter 3.

For most of incident channeled particles, the energy spectrum shows a clear surface peak. Figure 2.2.6 shows the energy spectra of 100 keV protons scattered from SiC. In the channeling spectrum, most of incident channeled particles do not scatter back. Only the top few layers contribute to the peak in the energy spectrum, and there is a severe reduction in scattering from beyond the inside layers below the surface. However, in a random spectrum, the incident ion beam has a chance to collide with every atom in the bulk, resulting in a high count plateau.

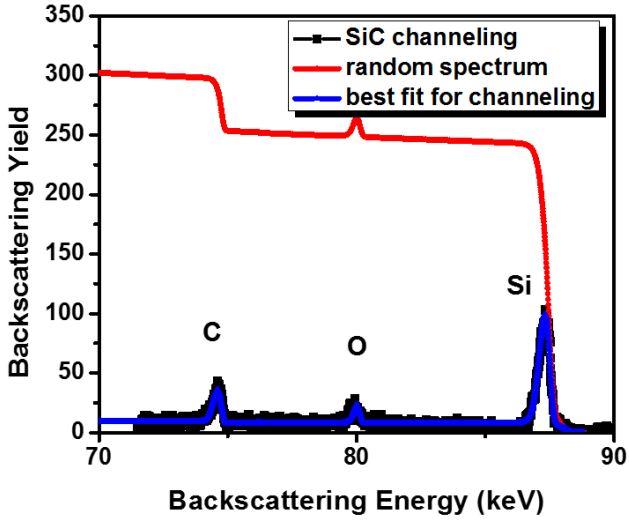

Figure 2.2.6 random and aligned spectra of a SiC crystal.

2.3 Instrumentation

MEIS requires a very high energy resolution, which implies a very stable accelerator, and a complicated detection system. This section focuses on a brief explanation of such instrumentation.

Figure 2.3.1 is a schematic of our MEIS system. The He or H_2 gas are ionized by electrons emitted from a high current filament, and a plasma forms inside the ion source. The filament current used for plasma formation is usually 25~30A. A 30kV acceleration voltage is applied between the ion source and magnet to pre accelerate the ion beam. The He (H_2) plasma contains He gas, radicals, He^+, He^{++}. The mass selection magnet lets only He^+ pass through. The selected He^+ beam is then accelerated to the desired beam energy, usually 80keV ~ 200keV. The variation of beam energy is less than 10eV

measured by a voltage meter, so that the beam energy variation is not a limiting factor. After acceleration, a magnet is used to steer the ion beam into the desired beam line. Two sets of lenses are used to confine the beam. Two beam confinement slits of 0.1mmx0.01mm are placed roughly 1.5m away from each other to minimize the angular divergence. The angular span of the ion beam is less than 0.1 degrees.

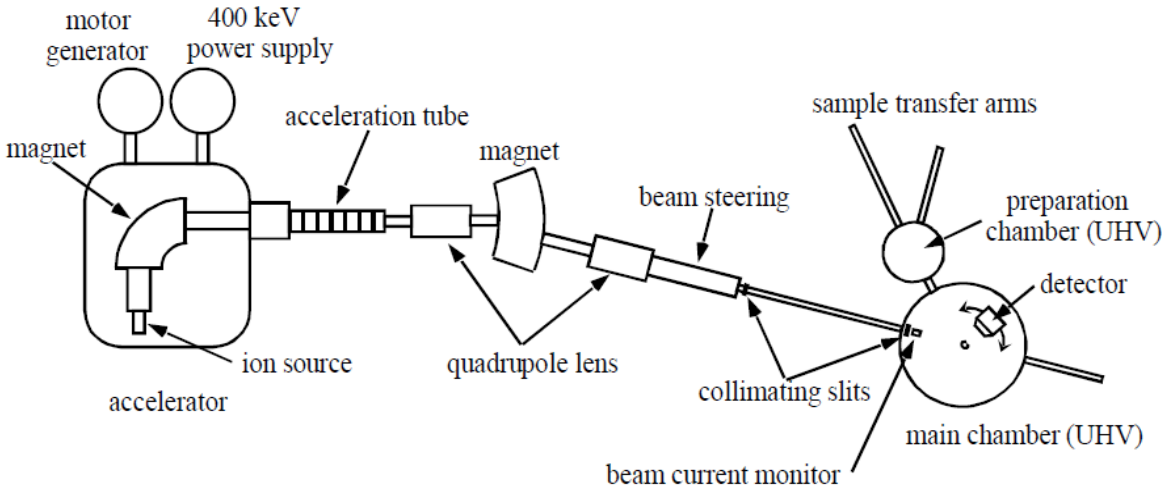

Figure 2.3.1 Schematics of MEIS system

The analysis chamber is under ultra-high vacuum of the order of 2~3 x 10^{-9} torr. A detailed schematic of the detection system is shown in figure 2.3.2.

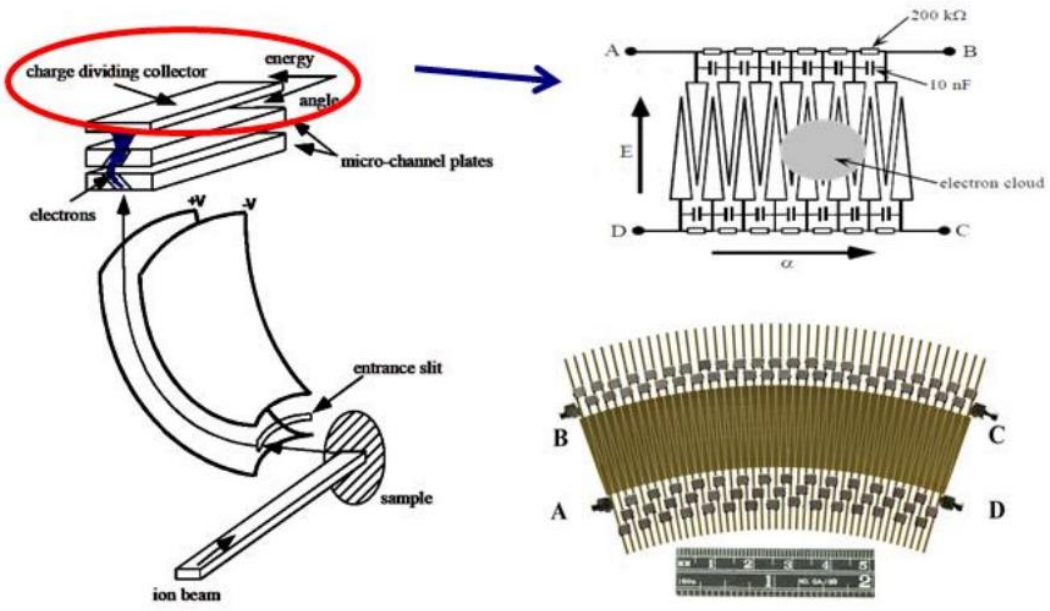

Figure 2.3.2 The MEIS detection system. A detailed picture of the PSD is on the right.

The detection system involves in a toroidal electrostatic analyzer (TEA), one pair of chevron-mounted micro channel plates (MCP), and a 2-D position sensitive detector (PSD). The scattered ion beam enters the detection system through the entrance slit. The long direction of the slit is in the scattering plane. The angular detection range is 22 degrees. The geometrical dimensions of the TEA is optimized for the desired resolution [11]. The center energy passing the TEA is determined by the voltage applied to the TEA

electrodes. E_{pass}=V/0.06, in which E_{pass} is in keV and V is in kV. The height of the slit is 0.1mm. It sets the range of energy accepted ~0.01949E_{pass}. For a 100keV beam, the voltage applied on the TEA electrodes is about 6kV, and the energy accepted is roughly E_{pass} ±1keV.

For each individual ion passing through the TEA and reaching the channel plates, roughly ~10^6 electrons are generated. The channel plate voltages are carefully adjusted for a reasonable efficiency and negligible image distortion [12]. The total voltage applied on the two channel plates is 1.5kV, among which 100V is applied between the detector and the channel plates set and 700V on each channel plate.

The electron cloud creates an electrical signal to the PSD, and the E and α of the center of the electron cloud coordinate in figure 2.3.2 is determined by analyzing the pulse from the four electrodes of the PSD.

$$\mathrm{E} = \frac{B+C}{A+B+C+D}, \quad \alpha = \frac{A+B}{A+B+C+D} \qquad \text{(Equation 2.3.1)}$$

Between electrode A and D there are 44 resistors, 200kΩ each, and 44 capacitors each with the capacitance of 10 μF. 45 resistors and 45 capacitors with the same resistance and capacitances are placed between B and C. The top and bottom electrodes are isolated [13].

A 2D energy spectrum is taken by changing the pass energy from the lower limit of the desired energy range to the higher limit. In angular direction, one degree is represented by 6 pixels in the energy window. For most of the MEIS analysis discussed in this thesis, an angular span of 1.6 degree (10 pixels) is used. This is a tradeoff between statistics and resolution.

2.4 Summary

Medium Energy Ion Scattering offers quantitative measurement of thin and ultrathin films. Its high energy resolution ensures sensitive elemental analysis and depth profile. Clearly resolved energy spectra of ^{12}C and ^{13}C has been reported[14]. This superb mass resolution is critical in surface science. The detection sensitivity is ~10^{14} atoms/cm^2, on the order of 0.1 monolayer or lower. The depth resolution near the surface is sub nanometer. Compared to SIMS and XPS depth profile, the ion beam is a non-destructive probe and has been used to study many surface and interface issues [15].

References:

1. T. Gustafsson, *Medium Energy Ion Scattering for Near Surface Structure and Depth Profiling*, in *Ion Beams in Nanoscience and Technology*. 2010, Springer Berlin Heidelberg. p. 153-167.
2. R. Hellborg, H.J. Whitlow, and Y. Zhang, *Ion Beams in Nanoscience and Technology*. 2010.
3. L.C. Feldman and J.W. Mayer, *Fundamentals of surface and thin film analysis.* North Holland, Elsevier Science Publishers, 1986.
4. L.C. Feldman, J.W. Mayer, and S.T. Picraux, *Materials analysis by ion channeling: submicron crystallography*. 2012: Academic Press.
5. W.K. Chu, J.W. Mayer, and M.A. Nicolet, *Backscattering spectrometry*. 1978: Academic Press.
6. E. Huttel, W. Arnold, H. Baumgart, and G. Clausnitzer, *Screening corrections to the Rutherford cross section.* Nuclear Instruments and Methods in Physics Research Section B: Beam Interactions with Materials and Atoms, 1985. **12**(2): p. 193-199.
7. J.R. Tesmer and M.A. Nastasi, *Handbook of modern ion beam materials analysis*. 1995: Materials Research Society.
8. W.H. Schulte, B.W. Busch, E. Garfunkel, T. Gustafsson, G. Schiwietz, and P.L. Grande, *Limitations to depth resolution in ion scattering experiments.* Nuclear Instruments and Methods in Physics Research Section B: Beam Interactions with Materials and Atoms, 2001. **183**(1–2): p. 16-24.
9. J.F. van der Veen, *Ion beam crystallography of surfaces and interfaces.* Surface Science Reports, 1985. **5**(5–6): p. 199-287.

10. J.F. Van Der Veen, J.B. Sanders, and F.W. Saris, *Two-atom model for the calculation of surface blocking in medium and high energy ion scattering.* Surface Science, 1978. **77**(2): p. 337-350.
11. P.M. Zagwijn, A.M. Molenbroek, J. Vrijmoeth, G.J. Ruwiel, R.M. Uiterlinden, J. ter Horst, J. ter Beek, and J.W.M. Frenken, *Two-dimensional position sensitive detection for medium-energy ion scattering.* Nuclear Instruments and Methods in Physics Research Section B: Beam Interactions with Materials and Atoms, 1994. **94**(1–2): p. 137-149.
12. H.C. Straub, M.A. Mangan, B.G. Lindsay, K.A. Smith, and R.F. Stebbings, *Absolute detection efficiency of a microchannel plate detector for kilo-electron volt energy ions.* Review of Scientific Instruments, 1999. **70**(11): p. 4238-4240.
13. R.M. Tromp, M. Copel, M.C. Reuter, M. Horn von Hoegen, J. Speidell, and R. Koudijs, *A new two-dimensional particle detector for a toroidal electrostatic analyzer.* Review of Scientific Instruments, 1991. **62**(11): p. 2679-2683.
14. M. Copel, S. Oida, A. Kasry, A.A. Bol, J.B. Hannon, and R.M. Tromp, *Medium energy ion scattering of Gr on SiC(0001) and Si(100).* Applied Physics Letters, 2011. **98**(11): p. 113103.
15. M. Ohring, *Materials Science of Thin Films*. 2001: Elsevier Science.

Chapter 3

SiC surface vibrations by Medium Energy Ion Scattering

3.1 Introduction

3.1.1 Silicon carbide

Silicon carbide based MOS devices are a topic of research and development for high temperature and high power applications. These specific uses arise as a result of the large band gap, ~ 3.2 eV, for the 4H crystalline polytype. One of the major advantages of SiC is that, just as Si, it forms a native oxide in the form of SiO_2, making most processes developed for Si suitable also for SiC. However, the interface of SiO_2/SiC is a major obstacle for wider use, limiting the channel mobility and generally degrading their performance. One of the factors affecting the channel mobility is the crystallinity of the top most few layers of SiC. A more extensive discussion of SiC material and device properties is given in chapter 4. Here, we instead focus on the crystal structure and the thermal vibration of atoms.

3.1.2 Ion channeling in silicon carbide

Ion beam channeling is an effective and quantitative way to determine the structure of surfaces and buried interfaces. Specifically, the surface peak intensity in ion beam channeling is a measure of the physical condition of the top most few layers on the surface. When the ion beam is aligned to a crystallographic direction in a well-ordered single crystal, the back scattered particles originate from atoms almost exclusively in the

near surface region, resulting in a well-defined surface peak in the energy distribution of the backscattered ions. The intensity of the surface peak in channeling geometry not only reveals information of surface structure but is also a measure of the thermal vibration and dynamics.

The two - atom model gives a simple estimate of the channeling surface peak size [1-4]. In this model, only the first two atoms in the string contribute to the surface peak, and the size of the surface peak is determined by only one parameter, the ratio of thermal vibration amplitude ρ to the shadow cone radius R_c. The contribution of the second atom in an atomic string is given by[2]:

$$\boldsymbol{I_2 = e^{-\frac{R_c^2}{2\rho^2}}\left(1+\frac{R_c^2}{2\rho^2}\right)} \qquad \boldsymbol{R_c = 2\sqrt{\frac{Z_1 Z_2 e^2 d}{E}}} \qquad \text{Equation (3.1.1)}$$

, where Rc is the shadow cone radius of the first atom under the incident ion[4] for pure Coulomb scattering, ρ is the relative 2D rms thermal vibration amplitude, d is the atomic spacing, Z_1 and Z_2 are the atomic numbers of the incident and target atoms respectively, and E is the energy of the incident beam. In the discussion above the value of ρ is a critical factor in predicting the surface peak intensity. In the two atom model, ρ represents the relative vibration amplitudes of the first two atoms. In general, these vibrations are not independent, but are correlated in space and time because of atom-atom bonding.

3.1.3 Correlation effects in thermal vibrations

In earlier studies, the importance of correlation effects in vibrations was discussed only to a limited extent. Studies with computer simulations have shown the effect of correlated vibrations in the transverse direction (perpendicular to the atomic string) on ion beam channeling measurements. In those studies, the correlation was introduced as a reduction factor (r.f.) of the vibration amplitude [5-7].

$$r.f. = (1 - c)^{\frac{1}{2}}, \qquad \text{Equation (3.1.2)}$$

in which c represents the effect of correlation. More precisely, if only two atoms are involved, the distribution of $(x_1 - x_2)$ (the relative displacement of two atoms in x direction), follows $N[0, \sigma\sqrt{2(1-c)}]$, a normal distribution with an average of 0 and a standard deviation of $\sigma\sqrt{2(1-c)}$[6]. Therefore the effect of correlations on the relative vibrations of two atoms results in a smaller standard deviation, so that the scattering contribution of the second atom in the string to surface peak is reduced.

SiC has a high Debye temperature (1300K) and the bond between adjacent Si atom and C atom is small (1.89Å). It is expected that vibrations of this atom pair in SiC are highly correlated. Using the Debye model [8], the correlation coefficient of SiC in the longitudinal direction is calculated to be 0.93 (with 0 being completely uncorrelated and 1 completely correlated). Longitudinal correlations of other materials (Ge, AgCl, VSe, KBr, and ZnSe) have been studied by neutron scattering and x-ray techniques (EXAFS), and coefficients of 0.61 to 0.78 have been reported [9-13]. There are fewer reports of

transverse correlations due to the lack of appropriate experimental techniques. Correlated thermal vibrations in the transverse direction were studied for Cu (111) and Ni (111) by high resolution Medium Energy Ion Scattering (MEIS)[14], yielding a small correlation coefficient at room temperature of 0.2 [15]. In a study of the SiC/SiO2 interface associated with SiC MOSFET technology we have measured the surface peak of the SiC virgin surface. The results indicate a surprisingly large correlation in the transverse thermal motion of the strongly bonded SiC surface atoms.

3.2 Vibrational correlation effects in Medium Energy Ion Scattering from SiC

3.2.1 Sample description

In the present study, the surface peak of 4H-SiC, a polar material was measured with high resolution MEIS in different crystal directions for both the silicon terminated face SiC (0001) and the carbon terminated face SiC (000-1). The 4H-SiC on-axis crystals (no misscut) were obtained from Cree, Inc., with chemical mechanical planarization on the Si face (0001). A good quality carbon face (000-1) was obtained following a H_2 anneal at 1400^{o}C for 5 minutes to form a clean surface with acceptable roughness[16]. Standard RCA cleaning was done for all samples. No high temperature anneal was done on Si terminated SiC to avoid the effect of surface reconstruction [17]. MEIS channeling with the ion beam incident along the surface normal was performed with 100keV, 150keV and 200keV H^+ ion beams at room temperature, 700K and at 1000K. The samples

contain a small amount of surface carbonaceous species, presumably from contamination from the residual atmosphere. As the MEIS depth resolution is not sufficient to separate this adventitious surface carbon from the carbon in the SiC crystal, angle dependent X-ray photoelectron spectroscopy (XPS) was used [18]. Figure 3.2.1 shows the XPS spectrum of carbon 1s. The lower binding energy peak is from bulk SiC, and the higher binding energy one is from surface adventitious carbon. Our XPS measurements show that the surface adventitious carbon on the silicon terminated surface is $0.9 \times 10^{15} atoms/cm^2$, and on the carbon terminated surface $1.8 \times 10^{15} atoms/cm^2$. Those amounts have been subtracted below from the MEIS measured total carbon numbers.

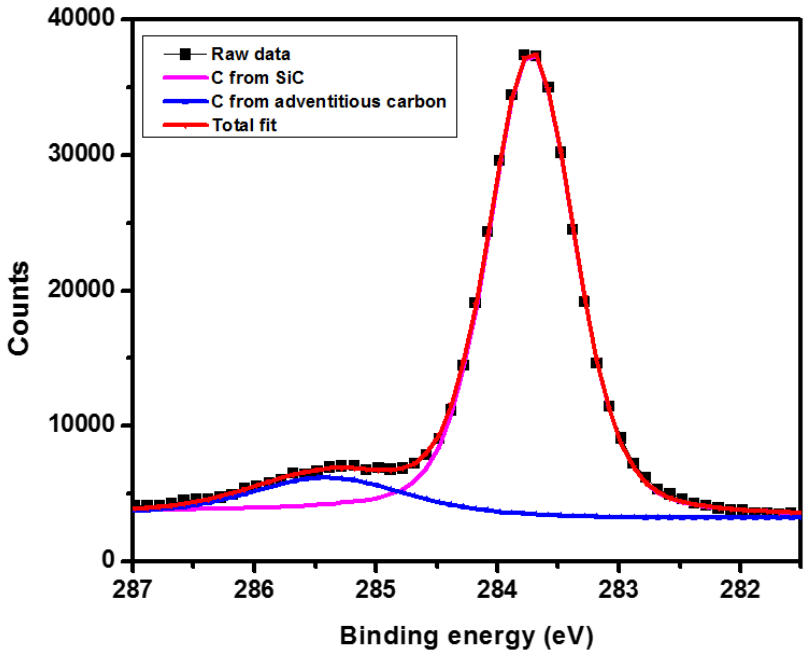

Figure 3.2.1, XPS spectrum of carbon 1s from carbon terminated SiC. The lower energy peak is the carbon signal from SiC, and the higher energy peak comes from adventitious carbon on the surface.

3.2.2 Ion beam damage in the channeling direction

Energetic ion beam collisions with crystals may induce crystal damage, displacing atoms from lattice sites and cause collision cascades. The possibility of significant ion beam induced damage needs to be carefully considered. We used well established computer simulations (TRIM[19] and MARLOWE[20]) to assess the importance of such damage.

Since TRIM is not set up for a channeling geometry, we used the following procedure. In a channeling geometry, most of the ions penetrate though the channels of the crystal and do not contribute significantly to the damage near the surface. A (small) portion of the ions incident in the channeling direction collide with the first layer of the atoms in the crystal. After the collision, those ions are deflected and travel into the crystal in different angles. TRIM simulations were done at all deflection angles and summed to be the total damage in the channeling geometry. The damage profile is summarized in Figure 3.2.2.

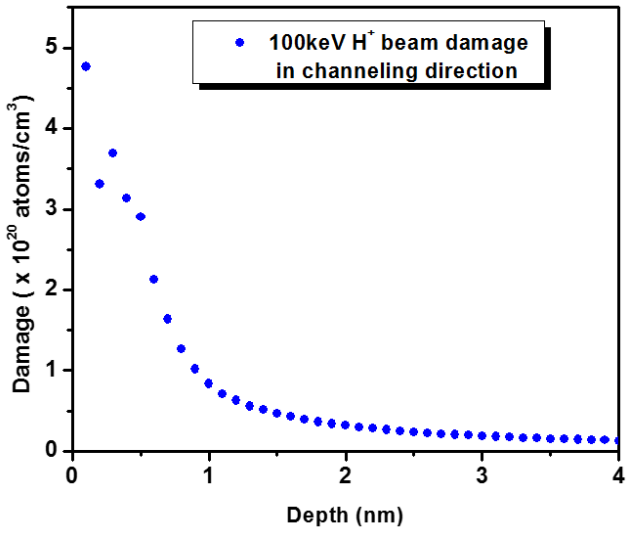

Figure 3.2.2, TRIM simulation of 100keV H^+ ion beam damage in a channeling direction normal to the Si (111) plane.

The beam dose used in this simulation is $5 \times 10^{16}\ atoms/cm^2$. Most of the beam damage for incidence in the channeling direction is concentrated within ~2nm of the surface, and the integrated beam damage is about $5 \times 10^{13}\ atoms/cm^2$. Considering that one layer of SiC consists of $1.2 \times 10^{15}\ atoms/cm^2$ of silicon and carbon atoms

each, and that the surface peak includes more than one layer, the ion beam damage in this study is therefore 2-3%, a small effect. Essentially similar results were obtained with the MARLOWE calculation.

3.2.3 VEGAS model of SiC lattice vibrations

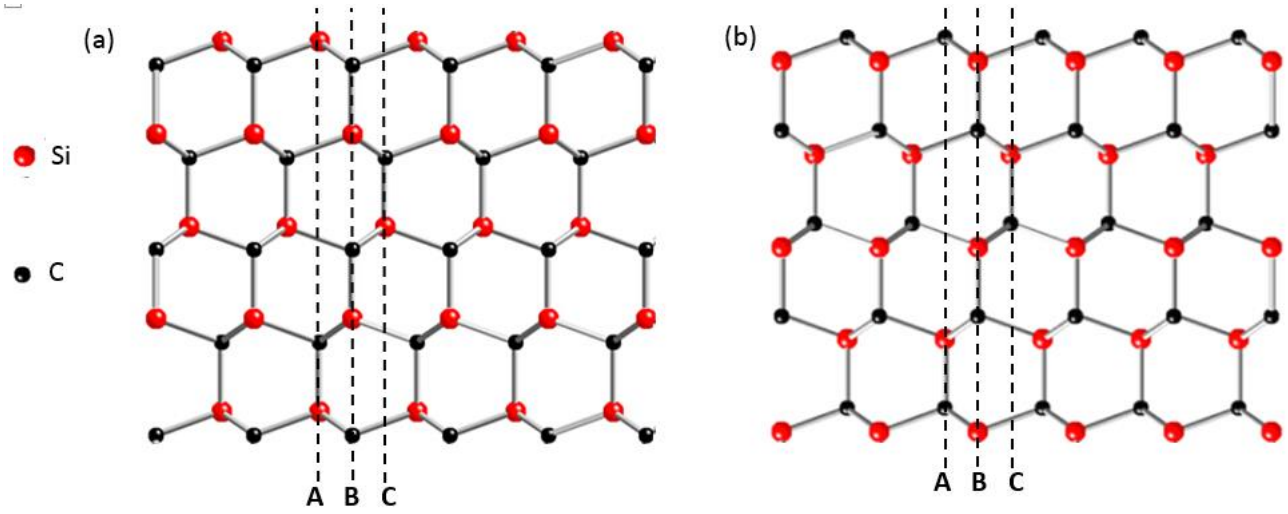

Figure 3.2.3, (a) Side view of silicon face 4-H silicon carbide. A, B and C are three inequivalent rows of atoms. (b) Side view of carbon face 4-H silicon carbide.

Figure 3.2.3 (a) shows a side view of the Si face (0001) with an H^+ ion beam incident along the normal from the top. There are three inequivalent rows of atoms, terminating in the first, second and fourth layers, respectively. An evaluation of the surface peak was done using the computer code VEGAS[21]. In the VEGAS model, each atom is given a Gaussian probability density distribution with three independent vibration amplitudes in the x, y and z directions, centered at the equilibrium position of the given atom. By

taking different values for the x, y and z vibration amplitudes, anisotropic vibrations can be modeled. In our study, we set the vibration amplitudes in three directions to be the same. To model a complete crystal, a rectangular building block representing the desired structure is created, and by taking periodic boundary conditions in the x and y directions (parallel to the surface), a complete crystal is constructed. A crystal model with 16 layers of atoms in z direction was created as the input. In each direction, the room temperature values of the vibration amplitude for carbon ρ = 0.056 Å and silicon ρ = 0.037 Å were used [22]. Compared to the two-atom model mentioned above, the VEGAS simulation estimates not just the first two atoms on a string but also calculates the contribution from deeper layers.

The ideal model for correlated vibration (two atoms) considers the center of the Gaussian representing the vibrations of the second atom to move with the top atom, according to the extent of correlation. The relative displacement of the two atoms follows another Gaussian with different standard deviation. However, in the VEGAS simulation, the center of vibration of every atom is fixed at the equilibrium position. One simple way of introducing a correlation effect in the VEGAS simulation is to renormalize the vibration amplitudes with a reduction factor as given in equation (3.1.2).

$$\rho^2_{Si(C)corr} \rightarrow (1-c)\rho^2_{Si(C)} \tag{3.2.1}$$

in which $\rho_{Si(C)\ corr}$ is the correlated vibration amplitude of the silicon atoms (carbon atoms), c is the correlation coefficient and $\rho_{Si(C)}$ is the vibration amplitude without any correlation effect. This approximation gives

$$\rho^2_{relative\ corr} = (1-c)\rho^2_{relative}. \tag{3.2.2}$$

To the ion beam, it is equivalent to the ideal model since the relative displacement follows equation (3.1.2).

3.2.4 MEIS data – room temperature

The size of the surface peak changes with ion energy as the shadow cone radius changes with ion energy. To better understand the behavior of the surface peak, three different beam energies were used. Figure 3.2.4 (a) shows the measured surface peak size and the VEGAS simulation of the silicon surface peak for the Si face SiC (0001). There are significant differences between simulation and measurements, the measured value being far smaller than the calculated value. Most studies of clean surfaces show either good agreement with calculation or values larger than the calculation. Values in excess of the calculated value are often indicative of a surface reconstruction or enhanced surface thermal vibration amplitude. Experimental results below the expected values are very rare, especially of the magnitude shown here. These results therefore suggest that the effect of correlated vibrations should be taken into consideration.

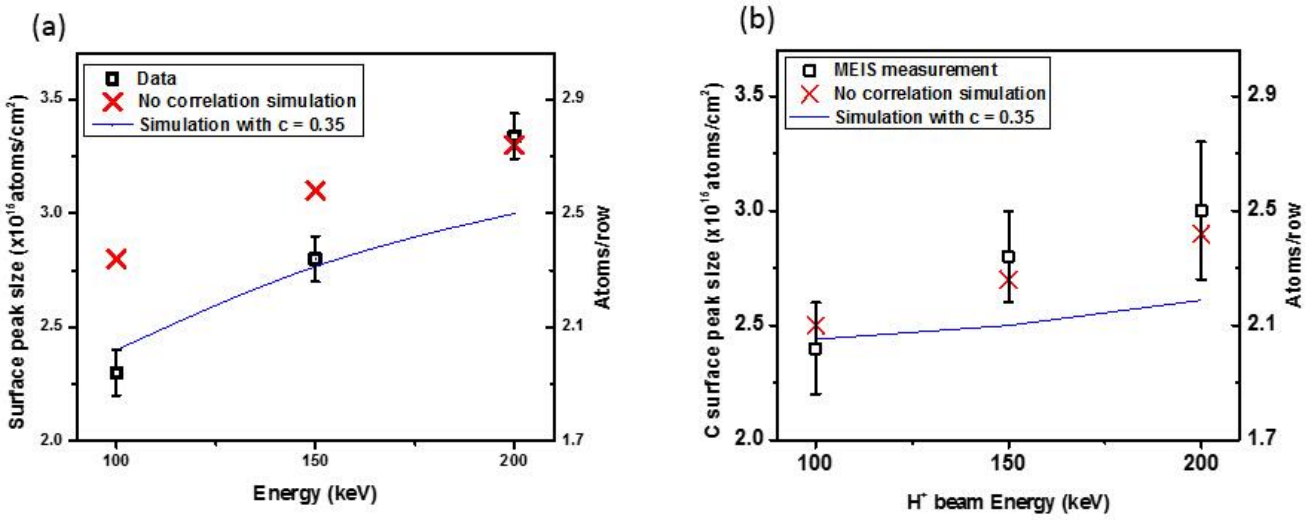

Figure 3.2.4 (a) Silicon surface peak size for the silicon face of SiC (0001). The blue curve is two-atom model calculation with a correlation coefficient of 0.35. (b) Carbon surface peak on the same surface as (a).

The data in Figure 3.2.4 (a) are compared to a VEGAS simulation with a correlation coefficient of 0.35 for every atom in the string (the blue curve) which agrees well at 100keV and 150keV. At higher energy, due to the small shadow cone and the increased vibrational amplitude, atoms in deeper layers have a better chance to interact with the ion beam, causing the surface peak to increase. In the VEGAS model, the probability for the deeper layer of Si (for example the 7th layer in the model) to collide with the beam is 0.6% at 100keV, and this number increases to 5.0% at 200keV. At higher energy, contributions from deeper atoms are no longer negligible, so that it is difficult to study

the interaction only between the first two atoms. An ion beam in the 100keV range is preferred for such a study since at this energy range, only a few layers of atoms are involved, and the interaction between the first two atoms is then most easy to study.

We attribute all measured silicon peaks in MEIS to silicon from an ideally terminated crystal. LEED was done to check for surface reordering but no evidence of reconstruction was observed. If on the surface the silicon atoms form silicon dioxide (or some other kind of surface disorder), those surface atoms are not in lattice sites, so they cannot block the beam flux incident on the deeper atoms. As a result, more silicon atoms will contribute to the surface peak compared to a case without surface disorder. We should therefore expect a larger surface peak size if there is surface disorder in contradiction to our data. The small surface peaks in the data indicate a lower bound on the vibrational correlation coefficient of 0.35.

There is no direct theoretical estimate of vibrational correlations in the transverse direction. The vibration in the longitudinal direction has been studied theoretically with the Debye model[8]. Following these authors and using the SiC Debye temperature (1300K) gives a vibrational correlation in the longitudinal direction at room temperature of 0.93 between the nearest neighbor S-C pair. Nielsen and Weber found that in Si (111), which has the same crystal structure as SiC, the *ratio* of the vibrational correlation coefficient for nearest neighbors in the longitudinal direction (0.7 at room temperature) and the transverse direction (0.25 at room temperature) is 2.8[23]. Taking the same ratio for SiC, the vibrational correlation coefficient in the transverse direction should be 0.33, very close to our value of 0.35.

The carbon surface peak data together with the simulation are plotted in Figure 3.2.4 (b). From Figure 3.2.3 (a), the carbon atoms sit on top of row B and row C. Since they are on the topmost layer directly open to the incident beam, the probability for these atoms to interact with the ion beam is unity. The contribution of these atoms to the surface peak size is always 1.2×10^{15} per cm^2 from each of these two layers regardless of the thermal vibration amplitude. Other carbon layers possibly need to be taken into account is the 6^{th} layer carbon in row B (Figure 3.2.3 (a), the third atom in row B). Its hitting probability is 8% with a 100keV H^+ beam, and this number increase to 31% for a 200keV H^+ beam (no correlation). Another one is the 8^{th} layer carbon, the second atom in row A. Its hitting probability is 1% at 100keV H^+ beam, and 10% for 200keV H^+ beam. The contribution of those atoms makes the surface peak (especially at higher energy) more than two full layers. Those two carbon atoms have no chemical bond with the Si atoms above them, and the distance to the silicon atoms above is father than the distance between the bonded C-Si. The correlation between those carbon atoms and the silicon on top of them must therefore be small. A strong correlation only exists between the silicon-carbon pair that is connected with a bond while there is no correlation between the bonded silicon-carbon pairs. In the correlated VEGAS model, the vibration of every carbon atom is reduced by the same amount. The correlated VEGAS model will then underestimate the vibration amplitudes of the carbon atoms that are not correlated with the Si atoms on top of them. To evaluate the hitting probability of those carbon atoms, the uncorrelated VEGAS model is more reasonable. The carbon surface peak fits the VEGAS simulation (w/o correlations, Figure 3.2.4 (b)). We also note that the value of

the carbon surface peak size at 100keV beam energy agrees well with a previous report from our group[24].

Parallel experiments were done on the carbon face, SiC (000-1) (Figure 3.2.3 (b)). On this face, silicon atoms are top most on rows B and C, directly open to the beam. There is no shadowing effect needed to calculate the silicon surface peak, so then correlation effects should not affect the silicon surface peak size. Figure 3.2.5 (a) shows the data. The agreement between the VEGAS simulation and the MEIS data meets the expectations.

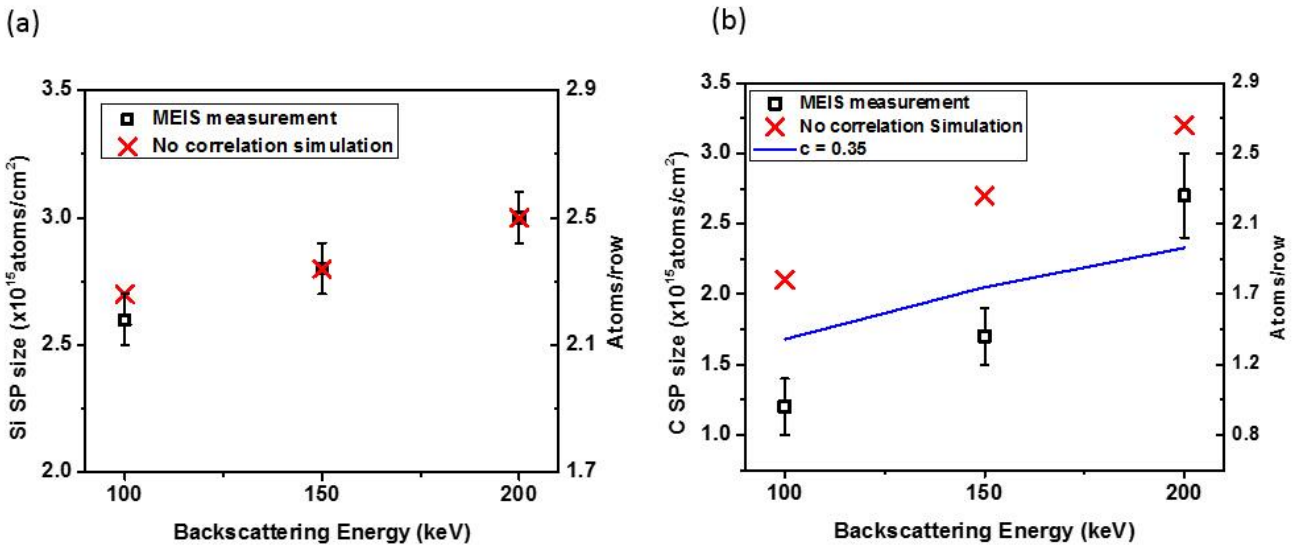

Figure 3.2.5, (a) Energy dependence of the silicon surface peak on carbon face SiC (000-1). (b) Carbon surface peak on the same surface. The blue curve is VEGAS simulation with c=0.35.

Figure 3.2.5 (b) shows the carbon surface peak size as a function of energy. The surface peak is significantly smaller than the VEGAS simulation w/o correlation. On this face, the carbon atoms are under the shadow cone of the top most silicon atoms on rows B and C, so a shadowing effect together with correlated vibrations may be observable. The VEGAS simulation gives the expected carbon amount to be detected by the ion beam, first considering non-correlated thermal vibrations. Obviously, the correlation effect is important. The blue curve in the figure is the VEGAS simulation with correlation coefficient of 0.35. The fitting is not as good as it is on the Si terminated face. One possible reason for that is that on the carbon face, the first layer of carbon atoms has dangling bonds which may bind with oxygen and hydrogen from the ambient. As a result, some of the measured (by XPS) $1.8 \times 10^{15} atoms/cm^2$ of C-O and C-H bonds may come from the first layer of carbon atoms in the carbon terminated SiC (000-1) bonded to oxygen and hydrogen. If we take all C-O and C-H bonded carbon as adventitious carbon, we possibly underestimate the MEIS measured carbon surface peak size here.

It has been reported that carbon terminated SiC (000-1) forms a $\left(\sqrt{3} \times \sqrt{3}\right)R30°$ surface structure under wet etching at 1400° for 15 minutes with pure hydrogen gas flow [25]. A simulation shows that if this reconstruction happens on our sample, the Si atoms' contribution to the surface peak will be $3.4 \times 10^{15} atoms/cm^2$.Oxygen atoms are involved in this type of surface reconstruction, and the number of oxygen atoms needed is $1.2 \times 10^{15} atoms/cm^2$. MEIS measurement on carbon terminated SiC (000-1) in this study gives $2.6 \times 10^{15} atoms/cm^2$silicon atoms, and $7 \times 10^{14} atoms/cm^2$

oxygen atoms. Considering that the sensitivity of MEIS near the surface is $1 \times 10^{14} atoms/cm^2$, the reported reconstruction did not form on our sample. The reason for that could be the purity of hydrogen (5% hydrogen mixed with Ar were used) and shorter annealing time.

3.2.5 MEIS data – temperature dependence

Thermal vibration amplitudes change with temperature, so the surface peak size is a function of temperature. To see this effect, the sample was heated in-situ, and MEIS channeling measurements with a 100keV H^+ beam were done at different temperatures. The difference between data and non-correlated VEGAS calculations decreases with increasing temperature (Figure 3.2.6 (a)). The reason is that the amplitudes of the lattice vibrations at high temperature, both with and without correlation, are large compared to the shadow cone radius which does not change with temperature. Therefore, vibrational correlations are not a main factor affecting the surface peak size. Following the calculation of the correlation coefficient in the longitudinal direction with the Debye model[8], and assuming the ratio of longitudinal and transverse direction correlation does not change with temperature, the correlation coefficient of SiC in transverse direction is 0.33 at 300K, and 0.34 at 1000K[23]. Therefore, for high Debye temperature materials like SiC, the correlation coefficient does not change much with temperature in the temperature range of this study. A VEGAS simulation with a correlation coefficient of 0.35 is plotted in Figure 3.2.6 (a). The lower temperature data fits well with coefficient of 0.35 (as above), while the higher temperature data fall between no

correlation and room temperature correlation, suggesting that the correlations are indeed affecting the surface peak size less at higher temperatures

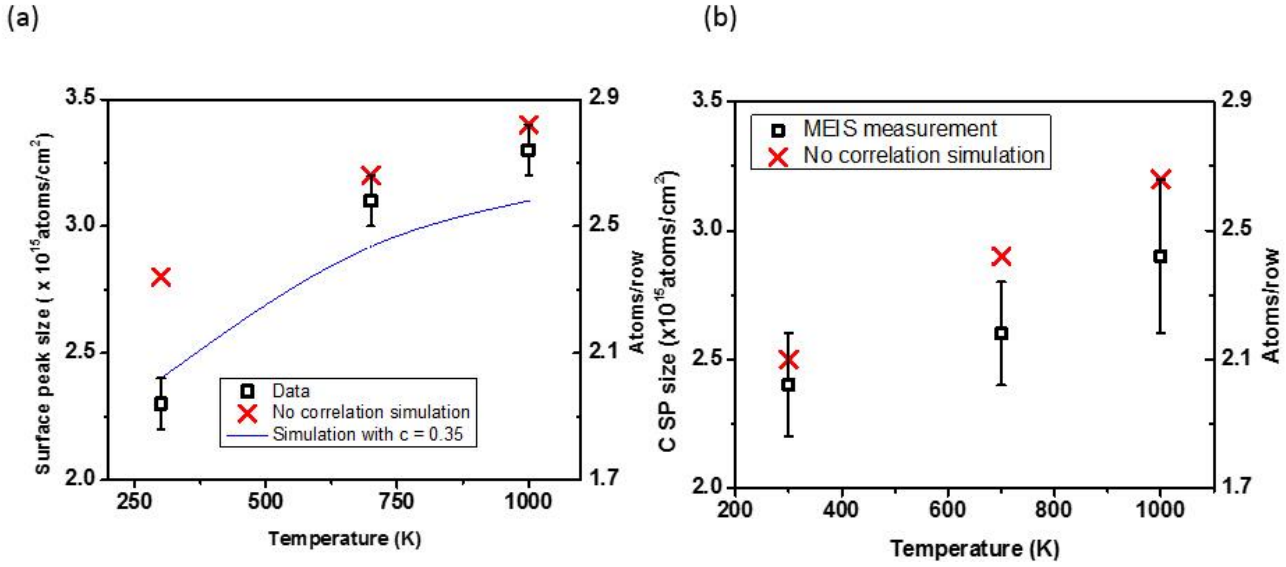

Figure 3.2.6, (a) The silicon surface peak on the silicon face of SiC (0001) as a function of temperature with simulations (see figure). (b) Similar results for the carbon surface peak. The H^+ beam energy was 100keV.

As discussed above, the carbon surface peak on the silicon face is determined by the top most atoms. Correlation effects should not be detected in the carbon surface peak. The measured numbers (Figure 3.2.6 (b)) are in reasonable agreement with the simulation at all temperatures considering that the poor statistics due to the increased background noise at high temperature and the low signal strength.

The temperature dependent measurements on the carbon face SiC (000-1) are shown in Figure 3.2.7. The silicon data agree with the VEGAS simulation, implying no correlation as expected. The difference between the VEGAS simulation and the MEIS data for the carbon surface peak (Figure 3.2.7 (b)) implies that a correlation effect is observed for the carbon atoms at all three temperatures. Adventitious carbon of $1.8 \times 10^{15} atoms/cm^2$ is removed from the MEIS measured carbon number for all temperatures. It is expected that at higher temperature, the adventitious carbon will be partially removed. As a result, other than correlated vibrations, one of the effects causing the difference between the MEIS measured carbon atoms and the VEGAS simulation in figure 3.2.7 (b) could be an over counting of adventitious carbon at high temperatures.

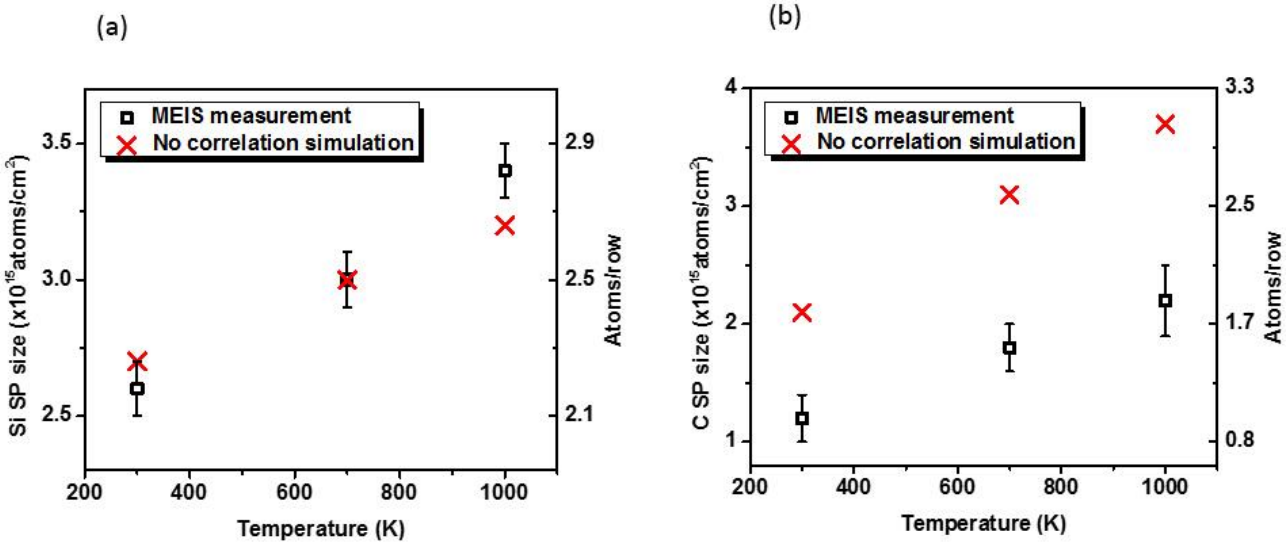

Figure 3.2.7, (a) Silicon surface peak and (b) Carbon surface peak on the carbon face SiC (000-1) as a function of temperature. The H^+ beam energy was 100keV in both cases.

3.2.6 Summary of the study of the surface peak and correlation effects in vibrations.

Both the silicon face SiC (0001) and the carbon face SiC (000-1) were studied with ion beam channeling measurements. A large correlation effect of the thermal motion of the surface atoms is required to account for the measured surface peak intensities. The measured correlation coefficient (as defined by equation 3.2.2) for the Si face is 0.35, which agrees well with theoretical estimate of 0.33. The carbon signal on the silicon face SiC and the silicon signal on the carbon face SiC, where correlations should not be observed, showed no such effect. At higher temperature, the effect of correlations on the channeling surface peak size is not as significant as at room temperature. These results illustrate a number of broader points. Dynamic properties of surface species, particularly the correlation effects, can be extracted by ion scattering probes. In particular the transverse component is not directly accessible experimentally by other established techniques. The thermal properties of the surface/and interfacial regions particularly are of intrinsic interest and also play a role in device science where phonon scattering may be a limiting transport mechanism. Finally the correlation effect in SiC may be particularly strong because of the strong Si-C bonding and accompanying short spacing. Thus the correlation effects must be included in ion scattering studies of the surface and interface science of SiC.

3.3 Applications of the SiC surface peak measurement.

3.3.1 Excess carbon measurement

The relatively poor inversion layer mobility in SiC devices has been attributed to defects at the oxide/semiconductor interface. One hypothesized source is the possible existence of excess carbon at the interface. In the following we describe how surface peak measurements contribute to detecting interface excess carbon.

The oxidation of SiC forms SiO_2 and no detectable carbon was found in the bulk of the oxide. During oxidation carbon atoms in the SiC forms mainly CO during oxidation, which is released into the atmosphere and/or into the SiO_2/SiC interface [26]. However, the physical structure of the SiO_2/SiC interface remains unclear. One major debate concerns the amount of and the influence of excess carbon near the interface. K. C. Chang et al. reported the existence of a carbon rich transition layer near the surface of SiC after oxidation [27-30]. The C/Si ratio in the transition layer varied from 1.2 to 1.5 for different oxidation temperatures [27], and the thickness of the transition layer is 10 to 15 Å. Nitric oxide (NO) anneal has been reported to reduce the C/Si ratio and increase the channel mobility [31]. A simple estimate of the carbon surface peak if the transition layer exists gives $3.4{\sim}4.8 \times 10^{15} atoms/cm^2$. The ideal carbon surface peak of SiC is $2.4 \times 10^{15} atoms/cm^2$. This difference is significant in ion scattering with our sensitivity of $1.8 \times 10^{14} atoms/cm^2$. MEIS channeling is therefore an ideal technique to probe the transition layer.

Zhu et al. applied MEIS channeling on silicon terminated SiC(0001), and concluded that the excess carbon is no more than $1.8 \times 10^{14} atoms/cm^2$ (the detection limit) by measuring the surface peak intensity[24]. The carbon surface peak reported by Zhu is $2.35 \times 10^{15} atoms/cm^2$ after oxidation, and $2.31 \times 10^{15} atoms/cm^2$ after an additional NO anneal, which are close to the surface peak of ideal SiC reported in our study.

3.3.2 Detecting near surface disorder

Heating the carbon face of SiC to a high temperature (1300^{o}C or above) drives silicon out of the surface and forms a surface layer of graphene. The quality of the SiC surface then has an impact on the properties of the graphene [32]. We have applied MEIS channeling to characterize the carbon face of SiC before and after H_2 anneal (Figure 3.3.1 (a)).

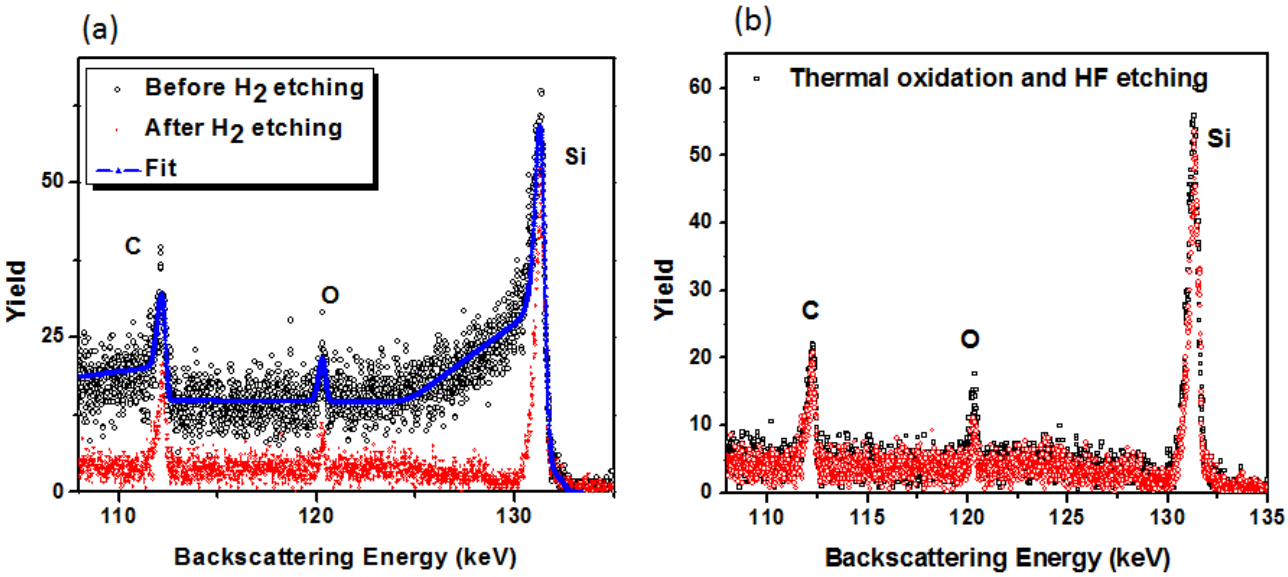

Figure 3.3.1, (a) MEIS channeling on an as received carbon face SiC crystal and after H_2 anneal. (b) Channeling on H_2 etched SiC and SiC after sacrificial oxidation.

The 4-H SiC crystal in this study was obtained from Cree. Inc. MEIS channeling with 150keV H^+ beam was performed on the as received carbon face (000-1) and the energy spectrum is shown in figure 3.3.1 (a). The broad Si surface peak and the slope after the peak indicate a thick disordered layer. An estimate from the energy position suggests that the disorder layer is about 15nm deep. Then the sample was annealed at 1400^{o}C in 5% H_2 mixed with Ar. The red curve in the figure 3.3.1 (a) is the channeling spectrum after the H_2 anneal. A clear surface peak with reduced background is achieved after the H_2 anneal, indicating the removal of the disordered layers. Thermal oxidation is a critical step in MOS device fabrication, and the thermal oxidation itself consumes SiC crystal. If the oxidation time is long enough, the damaged layers can be removed by the oxidation.

Figure 3.3.1 (b) is the MEIS channeling on the carbon face after 14 hour oxidation at 1150^{o}C followed by HF etch of the oxide. On the carbon face, this process is supposed to grow 400nm SiO_2, and consume 200nm SiC. The channeling spectrum after the oxidation is very close to the H_2 annealed one, suggesting that thermal oxidation itself is an effective way to remove near surface roughness and form a high quality single crystal.

3.3.3 Damage from reactive ion etching (RIE) and its recovery

One of the next generation of SiC devices is the trench MOSFET, also known as the U MOSFET. The side wall of the Si-face wafer is used as the device conduction channel for a higher current density and a better mobility. The side walls may correspond to crystalline a-faces, the (11-20) face. The device fabrication starts with the Si-face wafer and Reactive Ion Etch (RIE) is employed to form the trench. However, RIE is reported to enhance the surface roughness and create defects [33]. We have applied MEIS channeling together with AFM measurement to evaluate the RIE damage. Electric properties including the channel mobility and the interface defect density were measured by I-V, C-V and were correlated to those physical measurements.

Three on-axes, a-face 4-H SiC samples were used as substrates in this study, Epi (as received SiC substrate with an n-type SiC epitaxy layer), Epi + RIE and Epi + RIE + H_2 anneal. In the RIE process, SF_6 10sccm, Ar 40sccm, RF power 150W was applied and the DC bias formed by the plasma is 250V. The RIE process combines chemical reactions and physical sputtering. In the RIE process, SF_6 decomposes in the plasma to fluorine

radicals. The fluorine radicals then react with Si atoms in the SiC. The product of this reaction is SiF_4, which is removed by gas flow. Ar was added to sputter possible organic coatings formed during the RIE process.

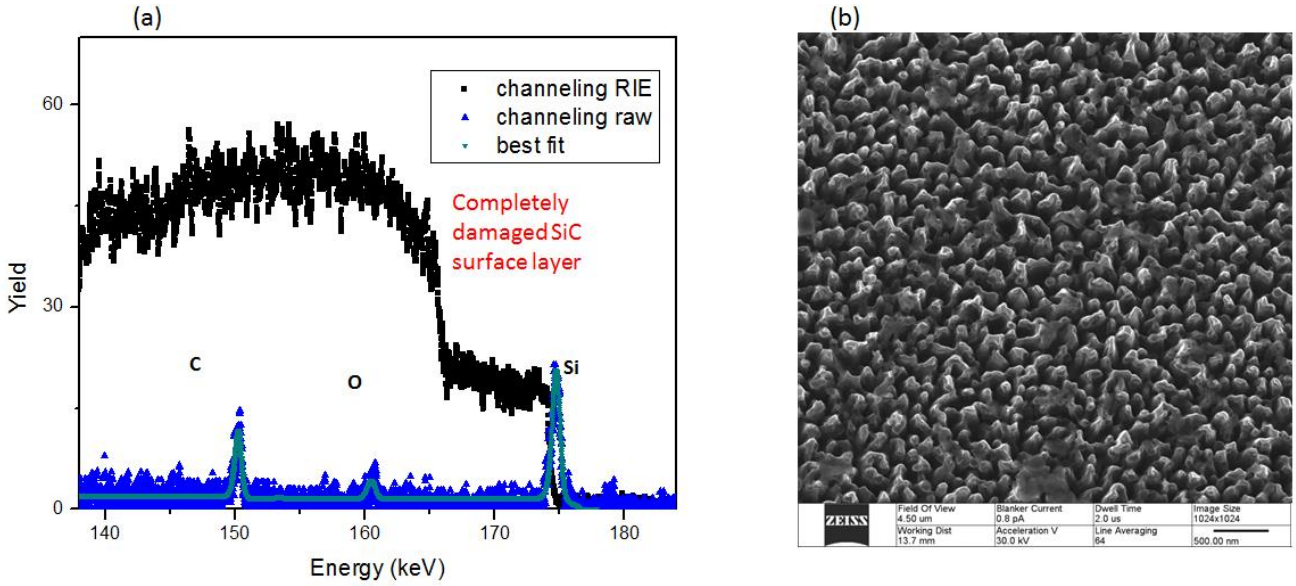

Figure 3.3.2, (a) MEIS channeling on Epi ready a-face SiC (blue) and RIE damaged SiC (black). (b) Helium Ion Microscope (HIM) image of RIE SiC.

Figure 3.3.2 (a) shows the MEIS channeling spectrum of the RIE roughened surface (black) and the regular a-face channeling on the Epi SiC (blue). The plateau after the Si leading edge is a reflection of a completely damaged crystal structure. A possible coating layer formed on top of the SiC crystal during the RIE process makes the leading edge energy lower than on the Epi. The step in the RIE spectrum fits the energy of fluorine, indicating that in the current RIE process, fluorine related material was not completely removed. Figure 3.3.2 (b) is the Helium Ion Microscope (HIM) image of the

RIE damaged SiC. The surface is rough and ~20nm spikes form on the surface. AFM was applied to calculate the surface root-mean-squire (RMS) roughness in the vertical direction. The Epi a-face SiC has a RMS value of 0.25nm, after RIE, the roughness increased to 4.57nm [34]. The RIE process on the a-face SiC damages near the surface crystal structure and leaves a rough surface.

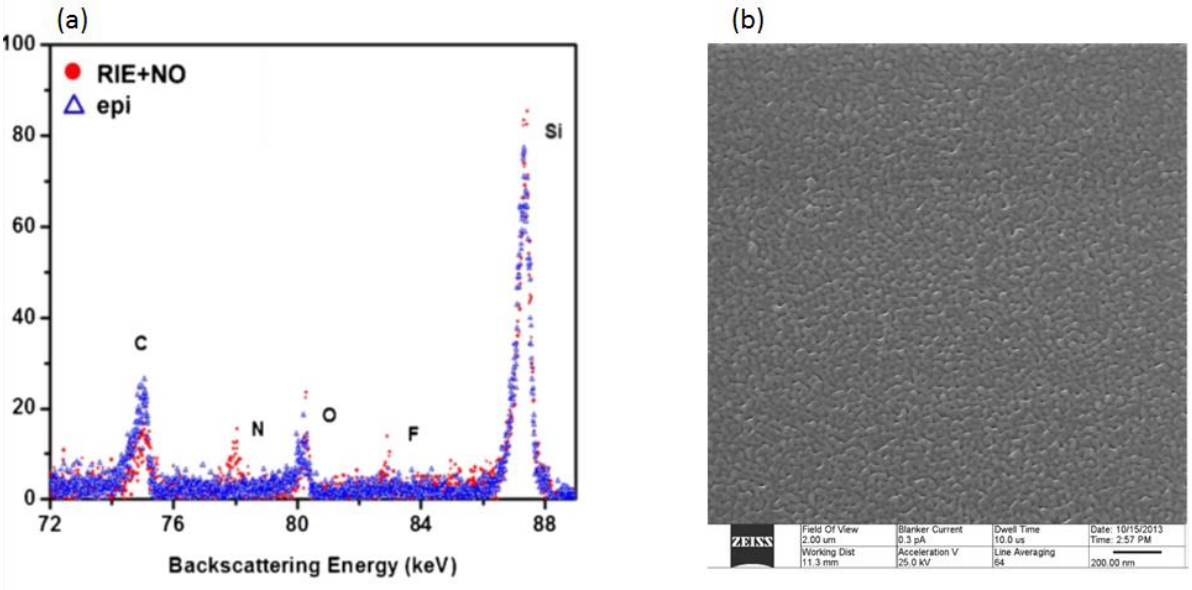

Figure 3.3.3, (a) MEIS channeling on Epi ready a-face SiC (blue) and RIE SiC after standard NO process (red). (b) Helium Ion Microscope (HIM) image of RIE+NO SiC.

The standard device fabrication includes: 1) RCA clean 2) thermal oxidation at 1150^{o}C for 1 hour 2) NO anneal at 1175^{o}C for 2 hours. This process is referred as the standard NO process. The gate was formed by patterned Al. After the C-V and I-V measurement, the gate and oxide was removed by wet etch, leaving the interface as a new surface for MEIS channeling. The results are shown in figure 3.3.3 (a). The Si peak in the RIE + NO spectrum overlap with the Epi one, meaning that after NO anneal, the crystal damage

was completely recovered, resulting an ideal Si surface peak. The NO process introduces less than one monolayer of N on the surface [18]. Surprisingly, even after the standard NO process in which more than 20nm SiC is consumed, there is still $3 \times 10^{14} atoms/cm^2$ of fluorine left on the surface. Its bonding and effect on device performance needs more study. Figure 3.3.3 (b) is the HIM image of the RIE + NO SiC. The surface roughness is less compared to the RIE only sample, but is far from flat. ~20nm domains are observed. The NO process recovered the near surface crystal damage, and the surface roughness remains.

As discussed above, H_2 anneal at high temperature removes SiC layers and creates a flat surface. In this work, H_2 anneal recovered not only the near surface crystal structure, also the RMS roughness is reduced to 0.28nm, which is close to the Epi condition.

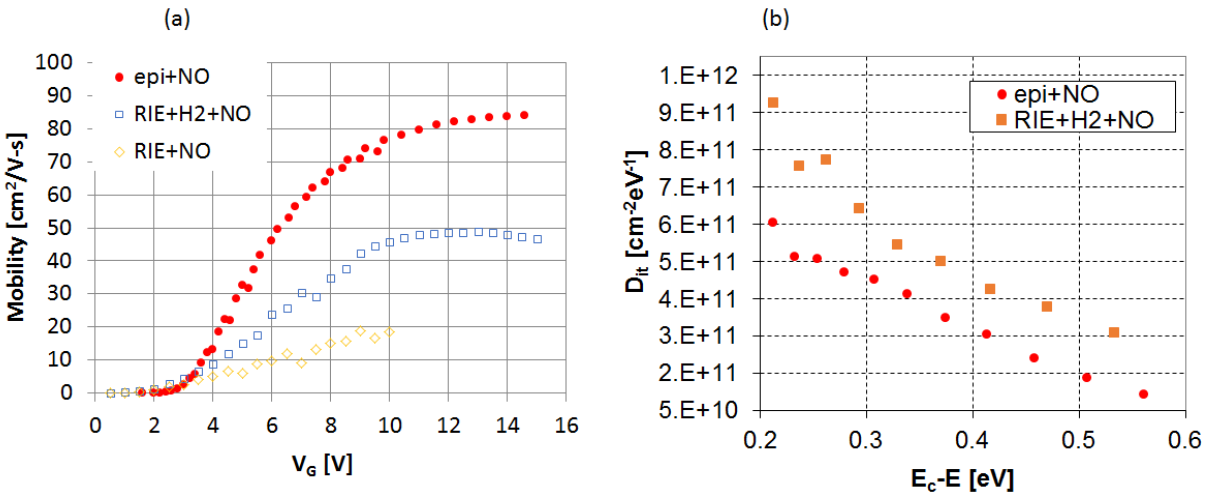

Figure 3.3.4 (a) Channel mobility of Epi (red), RIE (yellow) and RIE+H_2(blue) SiC. (b) Defect density of Epi (red) and RIE+H_2(orange).

Figure 3.3.4 shows the electrical measurement involving the device channel mobility and the interface defect density. Compared to the Epi condition which has a high peak mobility of 85 cm^2/V-s, the RIE process reduces the channel mobility significantly to 20 cm^2/V-s. The H_2 anneal process recovers the near surface crystal structure and the surface roughness, resulting in a higher mobility than the RIE SiC, but still lower than the Epi SiC. Figure 3.3.4 (b) compares the interface defect density of the Epi SiC and the RIE+H_2 anneal SiC. Even though there is little difference between those two from MEIS channeling and AFM, the interface defect density after the RIE+H_2 anneal at 0.2eV below the conduction band edge is twice that of the Epi SiC. This could explain the lower mobility after the RIE+H_2. There is no study so far on the type of defects introduced by RIE. A clue from MEIS is that compared to the Epi condition, RIE leaves fluorine on the surface, and that could be a source of defects.

References:

1. Feldman, L.C., P.J. Silverman, and I. Stensgaard, *Si(001) surface studies using high energy ion scattering.* Nuclear Instruments and Methods, 1980. **168**(1–3): p. 589-593.
2. Feldman, L.C., R.L. Kauffman, P.J. Silverman, R.A. Zuhr, and J.H. Barrett, *Surface Scattering from W Single Crystals by MeV He^+ Ions.* Physical Review Letters, 1977. **39**(1): p. 38-41.
3. Feldman, L.C. and J.W. Mayer, *Fundamentals of surface and thin film analysis*. 1986: North-Holland.
4. Stensgaard, I., L.C. Feldman, and P.J. Silverman, *Calculation of the backscattering-channeling surface peak.* Surface Science, 1978. **77**(3): p. 513-522.
5. Jackson, D.P. and J.H. Barrett, *Approximation for the surface backscattering yield from an atomic row with correlated thermal vibrations.* Nuclear Instruments and Methods in Physics Research Section B: Beam Interactions with Materials and Atoms, 1984. **2**(1–3): p. 318-321.
6. Barrett, J.H. and D.P. Jackson, *Role of correlations of lattice vibrations in channeling.* Nuclear Instruments and Methods, 1980. **170**(1–3): p. 115-118.

7. Jackson, D.P. and J.H. Barrett, *Modelling displacement correlations in computer simulations of particle-solid collisions.* Computer Physics Communications, 1977. **13**(3): p. 157-166.
8. Beni, G. and P.M. Platzman, *Temperature and polarization dependence of extended x-ray absorption fine-structure spectra.* Physical Review B, 1976. **14**(4): p. 1514-1518.
9. Basar, K., S. Siagian, Xianglian, T. Sakuma, H. Takahashi, and N. Igawa, *Correlation effects among atomic thermal displacements in oscillatory diffuse neutron scattering of ZnSe.* Nuclear Instruments and Methods in Physics Research Section A: Accelerators, Spectrometers, Detectors and Associated Equipment, 2009. **600**(1): p. 237-239.
10. Sakuma, T., S.R. Mohapatra, N. Isozaki, H. Uehara, Xianglian, K. Basar, H. Takahashi, O. Kamishima, and N. Igawa, *Estimation of inter-atomic force constants and phonon dispersion using correlation effects among thermal displacement of atoms in Ge.* Journal of Non-Crystalline Solids, 2011. **357**(2): p. 559-562.
11. Sakuma, T., Xianglian, N. Shimizu, S.R. Mohapatra, N. Isozaki, H. Uehara, H. Takahashi, K. Basar, N. Igawa, and O. Kamishima, *Correlation effects among thermal displacements of atoms in KBr.* Solid State Ionics, 2011. **192**(1): p. 54-57.
12. Sakuma, T., Xianglian, S. Siagian, K. Basar, H. Takahashi, N. Igawa, and O. Kamishima, *Correlation effects among thermal displacements of atoms in VSe by diffuse neutron scattering measurement.* Journal of Thermal Analysis and Calorimetry, 2010. **99**(1): p. 173-176.
13. Xiangliang, S. Siagian, K. Basar, T. Sakuma, H. Takahashi, N. Igawa, and Y. Ishii, *Inter-atomic distance and temperature dependence of correlation effects among thermal displacements.* Solid State Ionics, 2009. **180**(6–8): p. 480-482.
14. Gustafsson, T., *Medium Energy Ion Scattering for Near Surface Structure and Depth Profiling*, in *Ion Beams in Nanoscience and Technology*, R. Hellborg, H.J. Whitlow, and Y. Zhang, Editors. 2010, Springer Berlin Heidelberg. p. 153-167.
15. Okazawa, T., F. Takeuchi, and Y. Kido, *Enhanced and correlated thermal vibrations of Cu(111) and Ni(111) surfaces.* Physical Review B, 2005. **72**(7): p. 075408.
16. Ramachandran, V., M.F. Brady, A.R. Smith, R.M. Feenstra, and D.W. Greve, *Preparation of atomically flat surfaces on silicon carbide using hydrogen etching.* Journal of Electronic Materials, 1998. **27**(4): p. 308-312.
17. Bernhardt, J., J. Schardt, U. Starke, and K. Heinz, *Epitaxially ideal oxide–semiconductor interfaces: Silicate adlayers on hexagonal (0001) and (000$\bar{1}$) SiC surfaces.* Applied Physics Letters, 1999. **74**(8): p. 1084-1086.
18. Xu, Y., X. Zhu, H.D. Lee, C. Xu, S.M. Shubeita, A.C. Ahyi, Y. Sharma, J.R. Williams, W. Lu, S. Ceesay, B.R. Tuttle, A. Wan, S.T. Pantelides, T. Gustafsson, E.L. Garfunkel, and L.C. Feldman, *Atomic state and characterization of nitrogen at the SiC/SiO2 interface.* Journal of Applied Physics, 2014. **115**(3): p. 033502.
19. Ziegler, J.F., J.P. Biersack, and U. Littmark, *The Stopping and Range of Ions in Solids*. 1985: Pergamon.
20. Robinson, M.T. and I.M. Torrens, *Computer simulation of atomic-displacement cascades in solids in the binary-collision approximation.* Physical Review B, 1974. **9**(12): p. 5008-5024.
21. Frenken, J.W.M., R.M. Tromp, and J.F. van der Veen, *Theory and simulation of high-energy ion scattering experiments for structure analysis of surfaces and interfaces.* Nuclear Instruments and Methods in Physics Research Section B: Beam Interactions with Materials and Atoms, 1986. **17**(4): p. 334-343.

22. Gemmell, D.S., *Channeling and related effects in the motion of charged particles through crystals.* Reviews of Modern Physics, 1974. **46**(1): p. 129-227.
23. Nielsen, O.H. and W. Weber, *Displacement correlations in covalent semiconductors.* Journal of Physics C: Solid State Physics, 1980. **13**(13): p. 2449.
24. Zhu, X., H.D. Lee, T. Feng, A.C. Ahyi, D. Mastrogiovanni, A. Wan, E. Garfunkel, J.R. Williams, T. Gustafsson, and L.C. Feldman, *Structure and stoichiometry of (0001) 4H–SiC/oxide interface.* Applied Physics Letters, 2010. **97**(7): p. 071908.
25. Tochihara, H., T. Shirasawa, T. Suzuki, T. Miyamachi, T. Kajiwara, K. Yagyu, S. Yoshizawa, T. Takahashi, S. Tanaka, and F. Komori, *Scanning tunneling microscopic and spectroscopic studies on a crystalline silica monolayer epitaxially formed on hexagonal SiC(0001¯) surfaces.* Applied Physics Letters, 2014. **104**(5): p. 051601.
26. Ervin, G.U.Y., *Oxidation Behavior of Silicon Carbide.* Journal of the American Ceramic Society, 1958. **41**(9): p. 347-352.
27. Chang, K.C., J. Bentley, and L.M. Porter, *Nanoscale characterization of the silicon dioxide-silicon carbide interface using elemental mapping by energy-filtered transmission electron microscopy.* Journal of Electronic Materials, 2003. **32**(5): p. 464-469.
28. Chang, K.C., N.T. Nuhfer, L.M. Porter, and Q. Wahab, *High-carbon concentrations at the silicon dioxide–silicon carbide interface identified by electron energy loss spectroscopy.* Applied Physics Letters, 2000. **77**(14): p. 2186-2188.
29. Chang, K.-C., Y. Cao, L.M. Porter, J. Bentley, S. Dhar, L.C. Feldman, and J.R. Williams, *High-resolution elemental profiles of the silicon dioxide ／4H-silicon carbide interface.* Journal of Applied Physics, 2005. **97**(10): p. 104920.
30. Chang, K.-C., L.M. Porter, J. Bentley, C.-Y. Lu, and J. Cooper, *Electrical, structural, and chemical analysis of silicon carbide-based metal-oxide-semiconductor field-effect-transistors.* Journal of Applied Physics, 2004. **95**(12): p. 8252-8257.
31. Dhar, S., S. Wang, A.C. Ahyi, T. Isaacs-Smith, S.T. Pantelides, J.R. Williams, and L.C. Feldman, *Nitrogen and hydrogen induced trap passivation at the SiO2/4H-SiC interface*, in *Silicon Carbide and Related Materials 2005, Pts 1 and 2*, R.P. Devaty, Editor. 2006. p. 949-954.
32. Hannon, J.B., M. Copel, and R.M. Tromp, *Direct Measurement of the Growth Mode of Graphene on SiC(0001) and SiC(000-1).* Physical Review Letters, 2011. **107**(16): p. 166101.
33. Khan, I.A., J.A. Cooper, Jr., M.A. Capano, T. Isaacs-Smith, and J.R. Williams. *High-voltage UMOSFETs in 4H SiC*. in *Power Semiconductor Devices and ICs, 2002. Proceedings of the 14th International Symposium on*. 2002.
34. Liu, G., Y. Xu, C. Xu, A. Basile, F. Wang, S. Dhar, E. Conrad, P. Mooney, T. Gustafsson, and L.C. Feldman, *Effects and mechanisms of RIE on SiC inversion layer mobility and its recovery.* Applied Surface Science, 2015. **324**(0): p. 30-34.

Chapter 4

Deturium absorption in the SiC/SiO_2 interface

4.1 Introduction to SiC technology

4.1.1 A brief review of SiC

As briefly discussed in Chapter 3, SiC is a wide bandgap (WBG) semiconductor that has been employed for high temperature, high power application. SiC based light emitting diodes and UV photodiodes has been developed and fabricated [1]. Moreover, annealing SiC at high temperature leads to sublimation of Si atoms and formation of large area graphene [2]. It therefore provides a promising method for the fabrication of graphene device.

There are more than 200 polytypes of SiC and a variety of crystal structures including cubic (C), hexagonal (H) and rhombohedric (R). The electrical properties including bandgap and mobility vary significantly with polytype. The 4-H polytype is of current interest due to its attractive electrical performance. Unless otherwise stated, this thesis focuses on the 4-H polytype.

Material	E_g (eV)	μ_n ($cm^2/V.s$)	E_c (MV/cm)	V_{sat} ($10^7 cm/s$)	λ (W/cm.K)
Si	1.1	1350	0.3	1.0	1.5
4-H SiC	3.26	720	3.0	2.0	4.9
GaN	3.39	900	3.3	2.5	1.3
Diamond	5.45	1900	5.6	2.7	20

E_g: bandgap μ_n: electron mobility E_c: critical electrical field
V_{sat}: saturation velocity λ: thermal conductivity

Table 4.1.1. Important parameters of common semiconductors.

4-H SiC is marked in red.

Table 4.1.1 summaries some important parameters of common semiconductors. Compared to Si, 4-H SiC has many advantages. The wide bandgap decreases the leakage current, and at high temperature, reduces thermal generated intrinsic carriers. Its critical electrical field is three times that of Si, and the saturation velocity is twice as large. The high thermal conductivity is a significant advantage for high temperature applications of SiC devices. SiC is the only wide bandgap semiconductor that thermally grows SiO_2 as its native oxide, making it a promising candidate for fabricating the next generation of high temperature, high power MOSFETs. Ion implantation of nitrogen followed by activation anneal is applied to form n type doping, while p type usually involves aluminum. Phosphorous and boron are also used as donors and acceptors [3, 4].

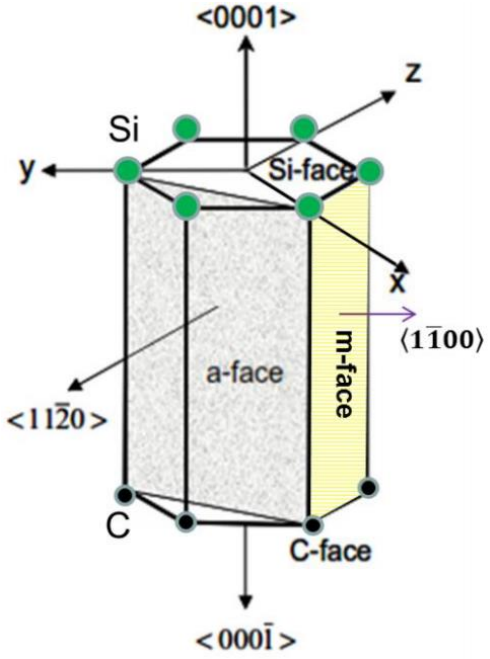

Figure 4.1.1. (adapted from [5]) Crystal faces of 4-H SiC.

Figure 4.1.1 illustrates the crystal faces of 4-H SiC. As discussed in Chapter 3, SiC has a bi-layer structure. In the (0001) plan, the bilayer terminates with silicon atoms, and this face is referred as the Si-face. The bilayer in (000-1) plan terminates with carbon atoms, and it is named C-face. The side wall forms the a-face. It is known that the defect density and the electron channel mobility of SiC are highly face dependent.

4.1.2 Thermal oxidation of SiC and possible defects at the interface

Thermally oxidized SiC forms SiO_2, and in general terms, the oxidation of SiC is very similar to that of Si. In this work, thermal oxides are thermally grown in a high temperature furnace. 5cm x 5cm SiC samples were cleaned with the standard RCA

method [6], then transferred into a furnace at 900^{o}C with Ar flowing at 500 sccm. The temperature was increased to 1150^{o}C in 1 hour. After the furnace reaches the desired temperature, the Ar flow is shut off and replaced with an oxygen flow at 500 sccm. To obtain the desired oxide thickness, the growth time has to vary with crystal face. The oxidation process can be illustrated as follows: 1) The O_2 molecules penetrate through the oxides and reach the SiC/SiO_2 interface. 2) The O-O bond in O_2 breaks and reacts with SiC to form the Si-O-C bond. 3) The carbon atoms in SiC are removed as a CO molecule, leaving Si-O-Si bonds [7].

The oxidation rate therefore depends on: 1) the oxide thickness. The time for the O_2 molecules to diffuse to the interface depends on the oxide thickness. The thicker the oxide is, the slower the growth rate. 2) The crystal face. Oxygen atoms break the Si-C bond and form the Si-O-C. Under the same conditions, the oxidation rate on the Si-face is slower than the a-face, and the C-face has the highest oxidation rate [5].

A striking difference between thermal oxidation of Si and of SiC is the properties of the interface. It has been reported that HF completely etches all SiO_2 grown thermally on Si, leaving no detectable oxygen at the interface, while on SiC, wet etch with HF leaves one monolayer of oxygen atoms at the interface that is not dissolved in HF [8].

The oxidation process on SiC leaves an interface with stable defects [9-11]. A physical detection of these defects is challenging because the density of electrically active defects measured by C-V is on the order of ~10^{12} cm^{-2}, which means one defect per 1000 SiC units, much smaller than the detection limit of most methods. However, a defect

related study is important because a small concentration of defects affect the electrical performance significantly [12].

The interface carbon atoms in SiC are released in the form of CO during oxidation. Research suggested that a small amount of C injects into the near interface of SiC, forming carbon interstitial defects [13]. MEIS channeling was employed to study the excess carbon and the results were discussed in Chapter 3. From these MEIS experiments, the excess carbon, if it exists, is less than $1.8 \times 10^{14} atoms/cm^2$. The MEIS results do of course not rule out the existence of a small amount of excess carbon below the physical detection limit. A small amount not detectable by physical techniques is enough to affect the device performance.

Another important defect are the carbon vacancies which usually are present at the interface of SiC/SiO_2. This type of defect results in Si dangling bonds which serve as electron traps. Equivalently, oxygen vacancies in the oxide near the interface create Si dangling bonds. Other types of defects like carbon clusters and carbon dimers at the interface have also been considered [14].

Collectively, the electronically active defects are described as “interface trap density”, which usually are measured by capacitance-voltage (C-V) measurement. Those defects originated from atomic imperfection cannot follow high frequency electric field. By comparing high frequency and low frequency electrical data, one gets a quantitative measure of the number of interface traps.

The bandgap of 4H-SiC is 3.26eV, allowing many defects at a wide range of energy levels to be present within its bandgap. The oxidation process involves carbon release, and the SiC/SiO_2 interface is not abrupt [15]. All these factors result in more interface defects than at the Si/SiO2 interface. MOS capacitor fabricated with the unpassivated 4H-SiC interface leaves an interface trap density on the order of 10^{13} cm^{-2} [16].

4.1.3 Interface passivation with NO anneal

One of the most widely used methods to reduce the interface trap density in SiC/SiO_2 structure is annealing in nitric oxide (NO). For 4-H SiC, it was reported that NO anneal after dry oxidation significantly reduces the number of interface defects and increases the device channel mobility, thereby enhancing the device performance [17-19]. On the Si face of 4-H SiC, the N coverage from the NO process has been reported to correlate with the interface defect density and the channel mobility, as shown in figure 4.1.2 [12]. The interface defect density decreases to ~10^{11} cm^{-2} at 0.2eV below the conduction band edge with half a monolayer N coverage and the device channel mobility increases from less than 5 $cm^2/(Vs)$ to ~50 $cm^2/(Vs)$.

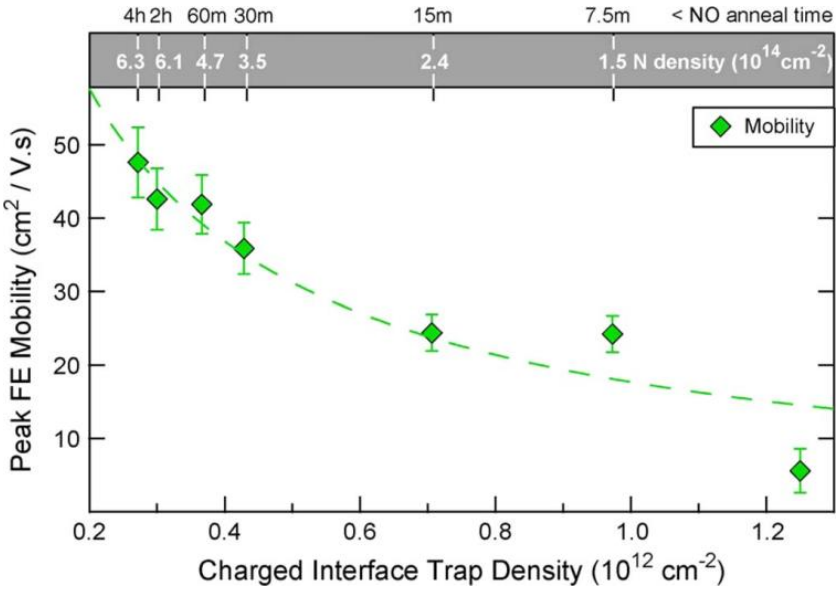

Figure 4.1.2, correlation between interface trap density, device channel mobility and interface N coverage. (Adapted from Rozen et al, 2011 [12])

A complete physical analysis on the NO process has been given by Xu, Y et al [8]. SIMS profiles suggest that N accumulates near the interface of SiC/SiO_2. No N was detected in the SiO_2 or deep in the SiC substrate. MEIS analysis provided a high resolution N depth profile and indicated that less than one layer of N atoms are at the interface layer within a depth uncertainty of less than 0.5nm. A systematic study of N coverage changes with NO anneal time reveals that, the interface N amount saturates at about ~$4 \times 10^{14} atoms/cm^2$, about 1/3 monolayer in SiC units. X-ray photoelectron spectroscopy

(XPS) was applied for the chemical bonding analysis. The N atoms directly bond with the SiC substrate and N-Si_3, O-N-Si_2, O_2-N-Si, and N-C bonds were found.

The mechanism of the NO process and how it reduces the defect density is not well understood. Based on a physical analysis, a possible explanation is that NO gas molecules diffuse through the oxide reaching the SiC/SiO_2 interface. Then the NO decomposes into N and O atoms. The O atoms further oxidize SiC forming SiO_2 and CO just like any other oxygen sources. The CO leaves the interface through the SiO_2. The N atoms at the interface compete with the O atoms to bond with Si. Some of the N atoms also bond with C [20]. The NO process significantly reduces the electrically active defects near the conduction band edge by more than one order of magnitude, and increases the device channel mobility. Therefore it is widely used in the SiC industry.

4.2 Water absorption in the SiC/SiO_2 system

4.2.1 The effect of H in Si/SiO_2 and SiC/SiO_2

In Si technology, the defects at the Si/SiO_2 interface are mainly related to the Si dangling bonds. The H_2 anneal process is well known to passivate those dangling bonds by forming Si-H bonds at the interface [21-23]. The H_2 anneal process is widely used in Si based technology as one of the standard processing steps. H_2 anneal has also been studied for SiC/SiO_2, but no positive effect was observed [24]. Another way of introducing H atoms into Si/SiO_2 and SiC/SiO_2 is to anneal in water vapor. It is known that in Si technology, exposure to water vapor can have detrimental effects due to accumulation of water in the oxide. In some conditions, water diffuses into the Si/SiO_2

interface and performs like H passivation. It is not a choice in Si technology because water vapor in the oxide may affect device reliability [25]. SiC based devices are designed to operate at high temperature and high power. Under such conditions, water vapor present during device fabrication or normal device operation could affect the electrical performance. The wet oxidation process in which the water vapor is involved has been demonstrated to improve the channel mobility of the C-face SiC and the a-face SiC 4-H SiC MOSFETs [26, 27]. So that the study of the effect of water vapor on SiC/SiO_2 based structure is essential.

In this chapter, we combine nuclear reaction analysis (NRA) and electrical measurements to study the effect of water exposure (D_2O) on several oxidized 4H-SiC MOS systems and compare to standard silicon based structures.

4.2.2 Nuclear reaction analysis (NRA)

Water (D_2O) absorbed in the SiC/SiO_2 and Si/SiO_2 system is represented by deuterium (D) content measured by NRA. NRA measures only the areal density of deuterium in the sample, giving no chemical analysis. Therefore all the analyses in this chapter are based on deuterium distribution. Deuterium can exist in the form of -D, -OD, or D_2O and they are not distinguished in this discussion.

The D(^{3}He, p)α reaction is used for quantitative analysis of D. During the measurement, a $^3He^+$ beam was directed to the target. $^3He^+$ introduces nuclear reaction with the deuterium nuclei

$$^3_2He + ^2_1D \rightarrow ^4_2He + ^1_1p \qquad Q = 18.35MeV \qquad \text{Equation (4.2.1)}$$

High energy protons were detected in this analysis.

The Q factor of the D(^{3}He, p)α reaction is calculated from the loss of mass during the reaction.

$$\mathrm{Q} = \mathrm{c}^2\left(M_f - M_i\right) = c^2\left(m_{He} + m_D - \left(m_\alpha + m_p + 2m_e\right)\right) = 18.3526MeV$$

Equation (4.2.2)

As Q >0, this reaction is exothermic, meaning the initial state always reacts to the final state. The energy gained in the reaction becomes the kinetic energy of the reaction products, the proton and the α particle.

In the center of mass system, the conservation of energy and momentum is applied to solve the energy of reaction products.

$$E_{He} + Q = E_p + E_\alpha, \qquad \overrightarrow{p_{He}} = \overrightarrow{p_p} + \overrightarrow{p_\alpha}$$ Equation (4.2.3)

The kinetic energy of the proton is a function of detection angle and the incident He energy and is plotted in figure 4.2.1 [28].

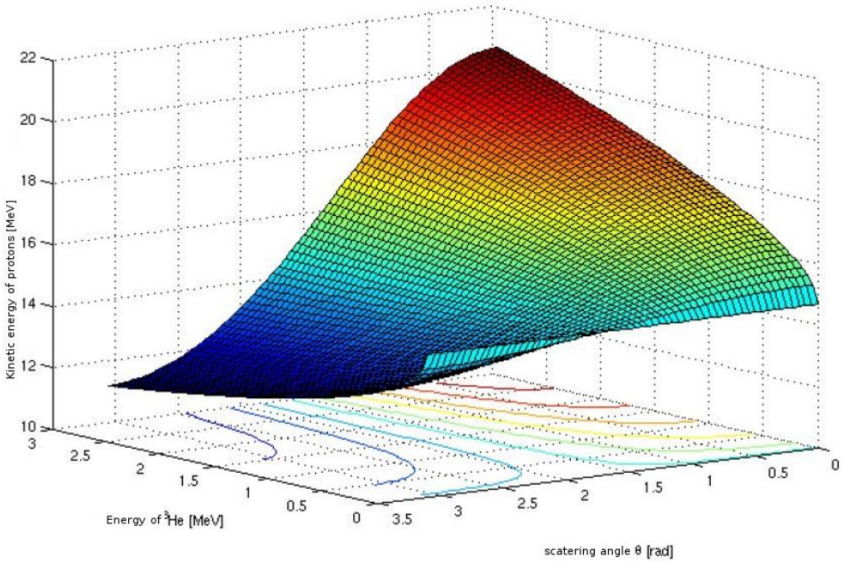

Figure 4.2.1, The kinetic energy of protons, resulting from a nuclear reaction D(^{3}He,p)α as a function of the scattering angle θ and the energy of the incident helium ion [28].

From figure 4.2.1, the proton takes most of the energy produced by the reaction since the α particle is heavier than the proton. The scattering angle in our NRA setup is close to 180^o and the incident He particle energy is ~750keV, giving the proton an energy of ~13MeV. A 100μm stainless steel foil is mounted in front of the detector as a filter for low energy particles, mostly α particles from the product of the nuclear reaction and He particles elastically backscattered from the sample, leaving almost zero background. Roughly, after the stopping foil, the energy of the protons reaching the detector is ~ 2MeV.

The proton yield collected is proportional to the solid angle of the detector Ω, the cross section $\sigma(E)$, the beam dose Q and the areal density of deuterium Nt.

$$Proton\ Yield \propto Q\Omega\sigma(E)\boldsymbol{Nt} \qquad \text{Equation (4.2.4)}$$

The statistical uncertainty is $1/\sqrt{Proton\ Yield}$. To minimize the statistical uncertainty and increase the detection limit, a large number of detected particles is desired. Increasing the total beam dose is not a realistic choice since it results in a long data taking time. Too high a beam dose could also damage the sample. We modified the existing system by adding two more detectors to increase the total solid angle Ω. The D detection sensetivity with the new setting is $2 \times 10^{12} atoms/cm^2$, comparable to the reported value [29].

The cross section of the D(^{4}He,p)α reaction is plotted in figure 4.2.2 as a function of the He beam energy [30]. It is a resonant reaction with FWHM of ~700keV. In our NRA analysis, the He beam energy used is 750keV, in the peak region of the cross section curve.

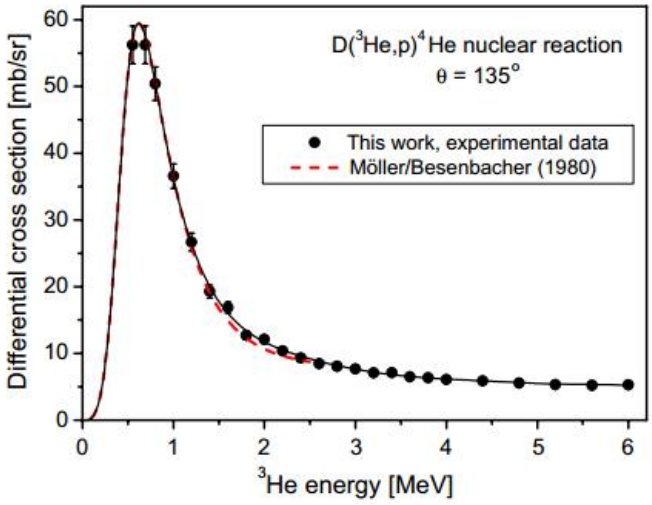

Figure 4.2.2 Differential cross-section of the D(^{3}He, p)^{4}He nuclear reaction [30].

The reaction cross section is highly energy dependent. In the case that the D(^{3}He, p)^{4}He nuclear reaction happens not only on the surface but also deep in the bulk. Similar as discussed in chapter 2, energy loss due to inelastic scattering to electrons and small angle scattering from nuclei need to be taken into account. In our experiment, the depth of D varies from the surface to a depth of 400nm. SRIM simulates the stopping process for ^{3}He particles traveling in SiO_2 [31]. The average stopping power is 25ev/Å. So that after 750keV ^{3}He beam passing through 400nm SiO_2, the energy of ^{3}He particles reacting the deepest D is 650keV. According to the cross section curve, the cross section of a 650keV beam is within 10% the same as at750keV. In the analysis of this chapter, the cross section is taken as a constant for all reactions.

Exact calculations of the solid angle and cross section is a tedious process and may yield more uncertainties. To quantitatively measure the D concentration, we compare the proton counts from the sample to a standard target. The standard is a D-doped Si, with a D areal density of $3 \times 10^{16}\ atoms/cm^2$. The areal density of D in the sample is then calculated from

$$\frac{Nt_{standard}}{Nt_{sample}} = \frac{Yield_{standard}}{Yield_{sample}} \qquad \text{Equation (4.2.5)}$$

A typical NRA spectrum is shown is figure 4.2.3, and the total yield is calculated as an integral from channel 700-1700.

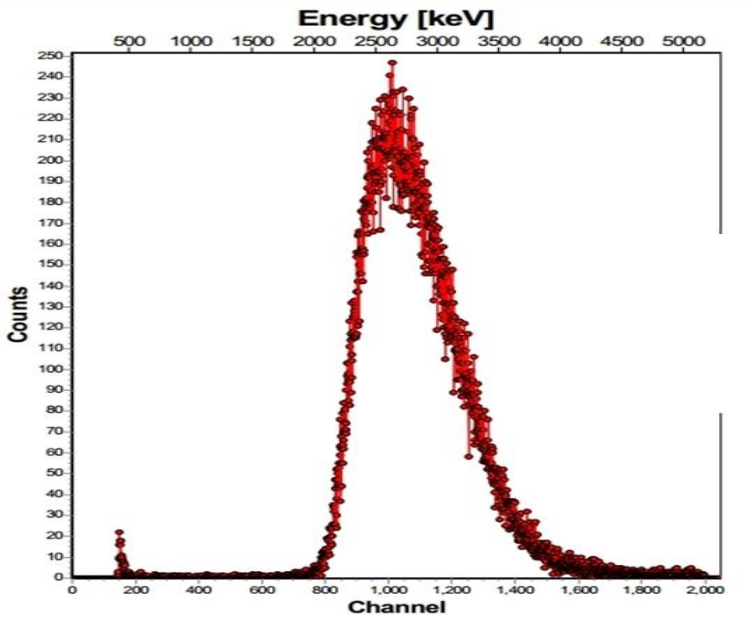

Figure 4.2.3, a typical NRA spectrum.

4.2.3 Deuterium absorption on C-face SiC - experiment

Most of the work on 4-H SiC have been on the Si-face because of its easy availability and the relatively low cost of the epi layer growth. Nevertheless, the C-face has some advantages over the Si-face as the oxide growth rate on the C-face is much higher. Dhar et al. made a comparison of the SiO_2 dry oxidation growth rate at 1150^{o}C on Si and the Si-face, the C-face and the a-face SiC in figure 4.2.4 [5]. In this study, 400nm SiO_2 was grown on SiC. Calculating from his formula, it takes 14hrs to grow 400nm SiO_2 on the C-face. On the Si-face of SiC, the time has to be measured in days. To minimize the statistical uncertainty of the D measurement, it is desirable to study thick oxides which possibly contain more D after processing.

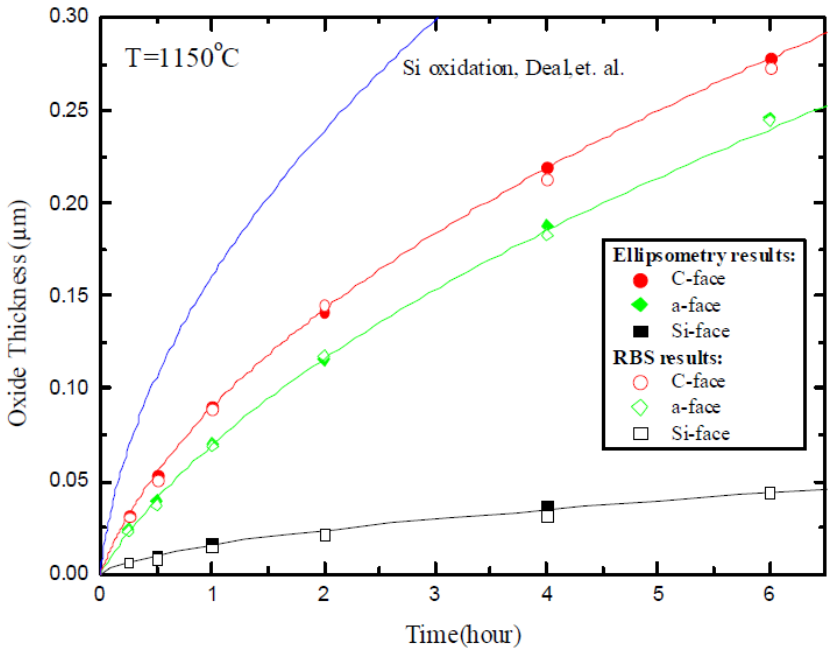

Figure 4.2.4 [5], Oxide thickness as a function of time for dry thermal oxidation of the (0001) C-, (11 2 0) a- and (0001) Si-terminated faces of 4H-SiC at 1150°C. The solid symbols indicate ellipsometer results and the opened symbols indicate RBS results.

Though the oxidation rate is high on the C-face, its interface with SiO_2 is reported to display a higher defect density under the same interface passivation conditions [32]. Water vapor introduced in the Si technology is known to passivate the Si dangling bonds and form a Si-H terminated surface [33]. One may therefore expect that similar to that of Si, water vapor exposure may change the electrical properties on C-face SiC by introducing D at the interface and changing the defect states. Recent studies show that the interaction with water between the SiO_2 grown on Si and Si-face SiC are significantly

different [34-36]. A more complete study of the interaction of water vapor in SiC devices, especially to physically understand the behavior of water vapor and to correlate the physical property and electrical performance would be desirable.

The standard oxidation process was done following the steps described in the earlier paragraph. A picture of the oxidation furnace is in figure 4.2.5.

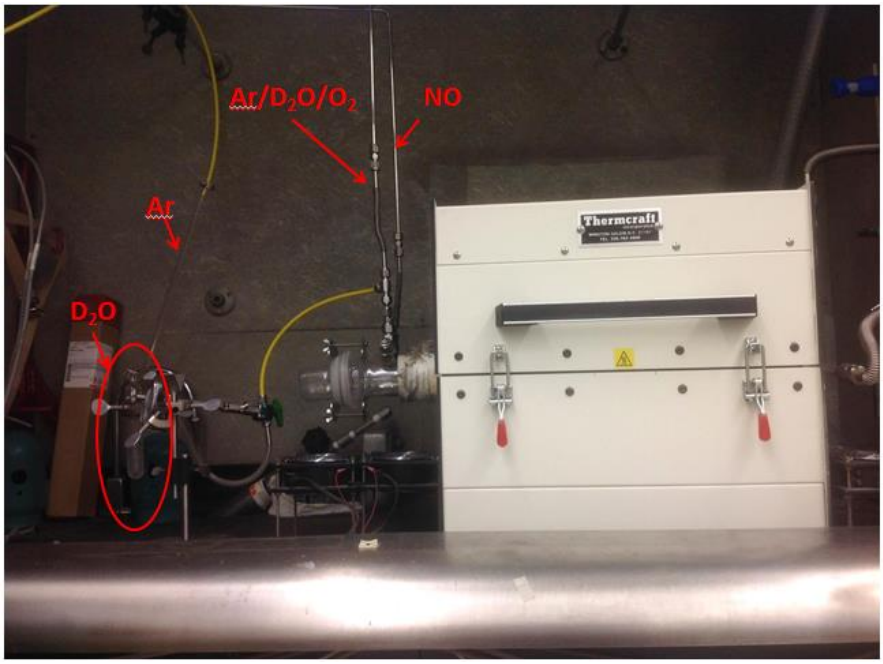

Figure 4.2.5, oxidation furnace with Ar, O_2, NO gas line and D_2O bubbler.

The desired thickness in this study is 400nm, which took 6 hours to grow on Si and 14 hours on C-face SiC. Then the samples were cooled down in the furnace to 900^{o}C with Ar flow of 500 sccm and then taken out of the furnace for further processing.

In addition to the dry oxidation samples, two types of post oxidation anneal were performed. The Si and C-face SiC samples with the same oxide thickness were annealed in nitric oxide (NO) at 1175^{o}C for 2 hours and in Ar under the same conditions.

Water exposure was performed in the same furnace. Ar flow of 100 sccm through the bubbler filled with D_2O liquid carried D_2O vapor into the furnace. The water exposure time was 15 hours.

In this study, the depth profile of D in the oxide and at the interface is obtained by controlled etch with buffered oxide etcher (BOE). Using D detection as a probe, there are two major questions to answer. 1) Are the oxides grown on Si and C-face SiC the same in terms of absorbing D? 2) Are the interfaces of SiO_2/Si and SiO_2/C-face SiC the same in terms of D absorption? To answer those two questions, the D absorbed at the interface and the D absorbed in the bulk oxide have to be distinguished. The interface D was measured by BOE etch off. The D in the oxide was obtained from subtracting the interface D from the total D measured in the SiO_2/Si and SiO_2/C-SiC structures.

MOS capacitors were fabricated on a comparison C-face SiC with ~ 2 x 10^{16}/cm^3 n-type epi layer grown on the surface. The same oxidation, post oxidation anneal and D_2O exposure processes were performed on those samples. The gate metal was Al deposited with E-beam evaporation. The capacitors were ~600 μm in diameter.

Several preliminary experiments were done to establish the parameters.

1) The oxide thickness was chosen to be 400nm.

The D absorbed in the oxide is ~4 x10^{18}/cm^3. To obtain a good statistics in NRA measurement, a thick oxide is desired for more D absorption. However, the He beam

energy loss is a significant effect for a thick oxide. Figure 4.2.2 indicates that the cross section of the D(^{3}He, p)^{4}He reaction is small when the He beam energy is lower than 500keV. The time required to grow the desired thickness is another factor limiting the oxide thickness. Considering all those factors, the thickness of 400nm oxide on both Si and C-face SiC was chosen.

2) The water exposure temperature was set to 400^{o}C.

There are many considerations when selecting the water exposure temperature. First of all, SiC devices are designed to work at high temperatures, so that a temperature higher than 100^{o}C makes practical sense. Secondly, the water exposure at 800^{o}C and higher could cause wet oxidation. The wet oxidation process could create a new interface containing possible D-Si or DO-Si bonds. It is difficult to separate the effect of the water exposure and the wet oxidation. Moreover, this study focuses on the D absorption at the interface and in the bulk oxide. Therefore a temperature that could clearly separate the interface and the bulk effect is preferable. Three temperatures (25^{o}C, 200^{o}C and 400^{o}C) of water exposure were tested on 400nm SiO_2/Si and 400nm SiO_2/C-face SiC. The total amount of the D absorbed are plotted in figure 4.2.6, and the bulk and the interface D amount of C-face SiC system are calculated in table 4.2.1.

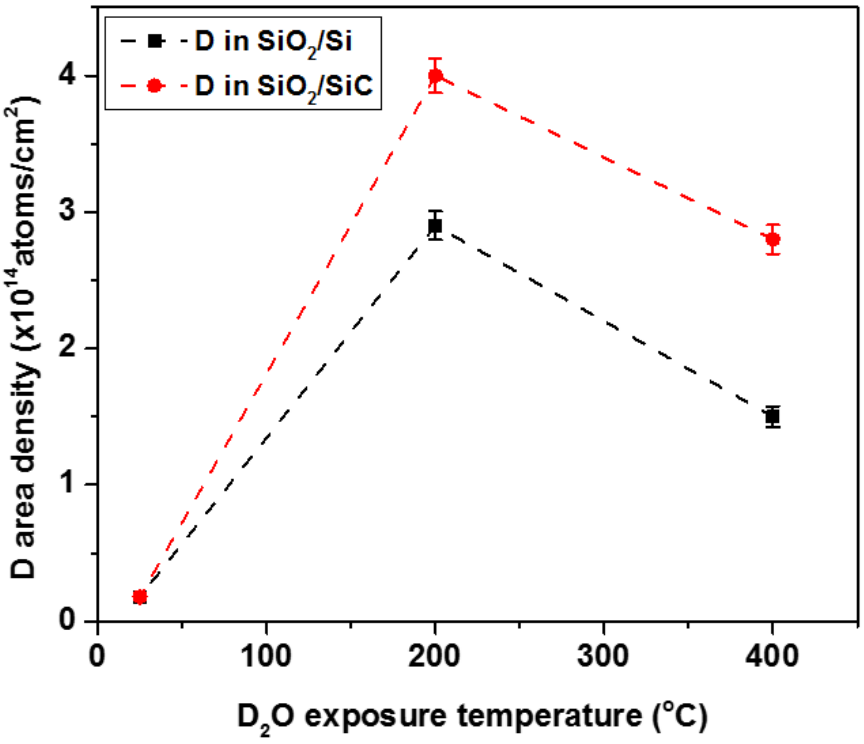

Figure 4.2.6, D absorption of 400nm SiO_2/Si and 400nm SiO_2/C-face SiC at 25°C, 200°C and 400°C.

Temperature	D at the interface (E14 atoms/cm^2)	D in the bulk oxide (E14 atoms/cm^2)
25°C	**N/A**	**0.2**
200°C	**0.3**	**3.7**
400°C	**1.0**	**1.8**

Table 4.2.1, the bulk and the interface D amount of C-face SiC at 25°C, 200°C and 400°C

Figure 4.2.6 indicates that the D uptake in both SiO_2/Si and SiO_2/SiC system are highly temperature dependent. The D uptake in both structures increases with temperature at the low temperatures and decreases at high temperatures. Similar behavior has been reported on H passivated Si [37]. The reason for this nonlinear behavior can be explained as there are two D related mechanisms taking place at the same time. One is the D absorption, which could involve the absorption as D_2O, -D to passivate defects in the bulk and at the interface, or –OD. The other one is D desorption, which means the passivated defects release their bonds with D and D goes into the vacuum. The reaction rate for both of the reactions changes with temperature. At low temperature, the D absorption dominates. At high temperature, the D desorption dominates. The D uptake at the interface and in the bulk oxide behave differently. Table 4.2.1 suggests that at 400^{o}C, more D reaches the interface and less D remains in the bulk compared to the 200^{o}C case. One of our primary questions to answer is how does D absorption behave in the bulk oxide compared to at the interface. The 400^{o}C experiments show significant amounts of D both at the interface and in the bulk. Considering all the issues discussed, 400^{o}C was chosen as the water exposure temperature.

3) The water exposure time is 15 hours.

Water absorption in SiO_2 follows the behavior of diffusion from the atmosphere to a planar sample [38]. Figure 4.2.7 shows the depth profile of D in SiO_2 on Si and on C-face SiC after a 10 min D_2O exposure at 200^{o}C. The thicknesses were achieved by controlled BOE etch and measured with an ellipsometer. Within uncertainty, the D diffusion profiles are the same in the oxide on Si and on C-face SiC. The 10mins water exposure

does not introduce any D at the interface and the bulk D concentration is far from the saturation value (compare to figure 4.2.8).

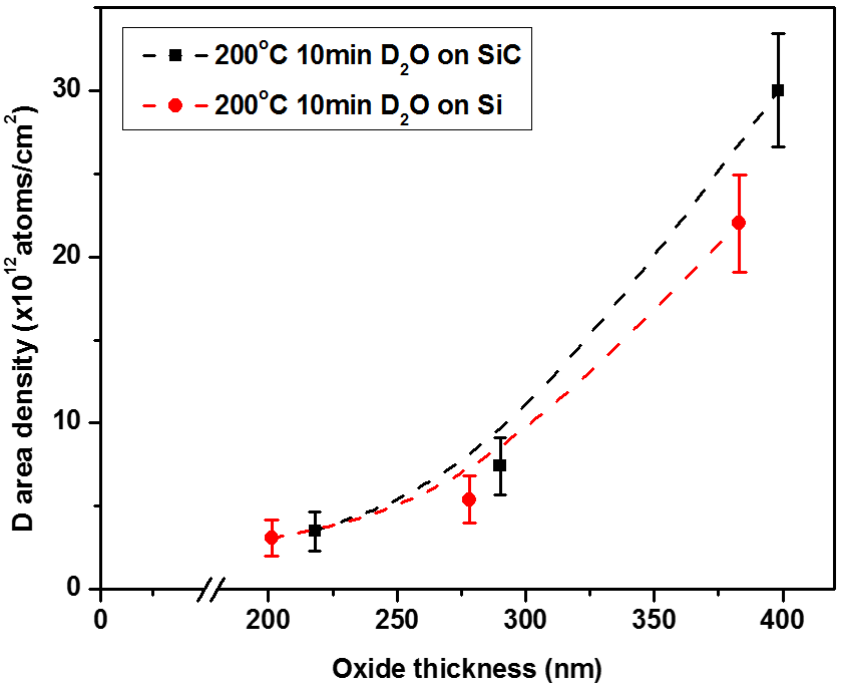

Figure 4.2.7, depth profile of D in SiO_2 on Si and on C-face SiC with 10 min D_2O exposure at 200°C.

In this study, the saturation D amounts in the oxide and at the interface are of interest. Figure 4.2.8 shows the total D content in the SiO_2/Si and SiO_2/C-face SiC as a function of water exposure at 400°C. For both Si and C-face SiC, the D absorption does not saturate at 27 hours. An exposure time of 15 hours introduces a similar level of D as 27 hours exposure. Considering the time budget, 15 hours water exposure was selected for all the following experiment.

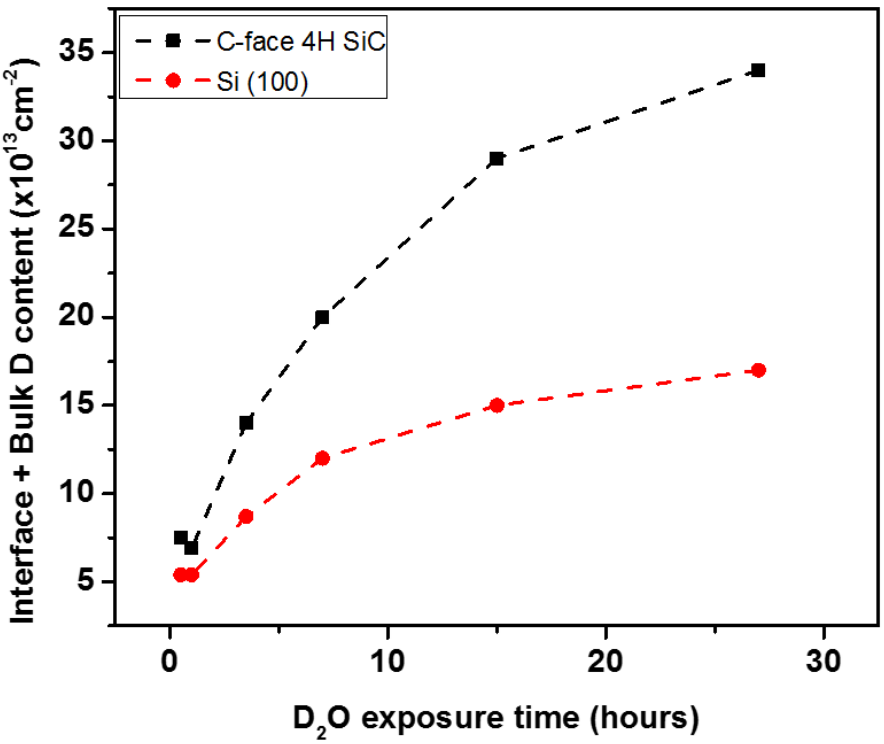

Figure 4.2.8, areal density of D in SiO_2/Si and SiO_2/C-face SiC structure as a function of time. The oxides are 400nm thick and the exposure temperature is 400°C.

4.2.4 Deuterium absorption on C-face SiC – results and discussion

400 nm SiO_2 on Si and on C-face SiC were exposed in water vapor in 400°C for 15 hours. Three identical samples were made on Si and C-face SiC. The two of them were etched to 200nm and fully etched for a D depth profiling study. The D contents as a function of oxide thickness are plotted in Figure 4.2.9. In the case of the 400nm oxide on Si and C-face SiC, the C-face SiC structure absorbs almost twice as much D as the Si structure. The absolute difference in the D content is roughly the same for the 120nm oxide as for the

400nm set. In the case of a fully etched oxide the difference remains the same. This result suggests that 1) the D distribution in the bulk oxide on Si is the same as in C-face SiC. This is consistent with other properties of the two SiO_2: The two oxides have the same etch rate, the same breakdown field and the same dielectric constant. 2) The difference of D absorption between the two systems occurs at the interface. The oxide/C-face SiC interface absorbs more D than the oxide/Si interface.

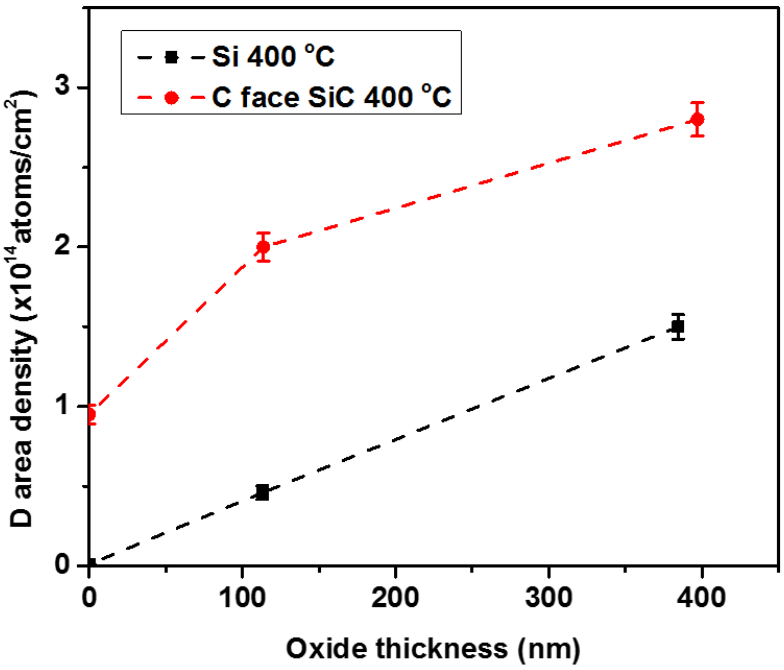

Figure 4.2.9, depth profile of D absorption in SiO_2/Si and SiO_2/C-face SiC.

It is known that the interface of SiO_2/SiC is different than that of SiO_2/Si. It has been reported that HF fully etches all the oxide on Si, but leaves one layer of oxygen on SiC

[8]. Electrical measurements observed a high interface defect density on SiC [14]. The difference in D absorption could be related to the interface structure and defects.

As discussed earlier, a NO anneal introduces N into the interface and changes the defect states. Therefore the NO anneal process could be an effective way to control D accumulation at the interface.

Treatment	D on C-face SiC (× 10^{13} atoms/cm^2)	D on Si (× 10^{13} atoms/cm^2)
regular	9.5	< 0.3
NO	1.6	< 0.3
Ar	14.0	

Table 4.2.2, the effect of post oxidation anneal on D accumulation at the interface.

NO and Ar annealed samples were exposed to water vapor at the same conditions and were etched off to study the interface. The interface D content of the C-face SiC and the Si in the three conditions, the oxidation, the NO and the Ar post oxidation anneal cases, are summarized in table 4.2.2. The Ar anneal was performed at the same temperature and for the same time as NO anneal as a control experiment. The NO anneal is known to introduce half a monolayer of N at the interface [39]. The results show that the D content at the NO annealed interface is significantly reduced. The Ar anneal under the same conditions slightly increases the interface D.

For a power device running at high temperature, the effect of water vapor is inevitable. It is therefore essential to study the correlation between the water absorbed (represented in

D content previously) and its effect on the device electrical performance. The effect of D on the electrical properties is represented by the shift of MOSCAP C-V curve. The C-V curve is affected by the oxide charges. Oxide charges include the fixed oxide charge Q_f, the mobile ion charge Q_m, and the oxide trapped charge Q_{ot} [40]. The oxide charges in the oxide and near the interface induce an electric field in the oxide. The voltage created by these charges is $-Q_{ox}/C_{ox}$.

The fixed oxide charge Q_f is very close to the interface and can be modeled as a sheet charge at the interface [41]. It is not affected by the oxide thickness and the defects in the bulk semiconductor. Its properties and density are decided by the oxidation and annealing conditions. At the SiO_2/Si interface, the excess Si atoms near the interface are believed to be the origin.

The mobile ion charge Q_m is induced mostly by alkali ions [42]. It moves in the oxide layer with the voltage applied. The C-V shift caused by the mobile ion charge increases under high temperature and high voltage operation. Thus the presence of the mobile ions causes device reliability issues, especially for high temperature and high voltage applications.

The trapped oxide charge is related to oxide defects.

The total voltage shift is

$$\Delta V = -\frac{Q_{ox}}{C_i} = -\frac{Q_f + Q_m + Q_{ot}}{C_i} \qquad \text{Equation (4.2.6)}$$

The MOSCAPs were fabricated with n-type C-face SiC. Figure 4.2.10 shows the flat band voltage of C-face SiC MOSCAPs after dry oxidation, NO anneal and Ar anneal. The absolute number of the flat band voltage for the carbon face MOSCAP (the black cross in the O_2 box) is large due to the high density of interface traps [39]. The NO

anneal reduces the interface defects therefore the flat band voltage after NO (the black cross in the NO box) has a lower value.

After NO anneal, the D accumulation at the interface is the smallest. Though not shown here, the D absorbed in the bulk oxide is on the same level as in the other two cases. The flat band voltage does not change before and after the water anneal. This is an indication that the D absorbed in the bulk does not respond to the C-V measurement. In other words, the D absorbed in the oxide does not create any charge and stays neutral.

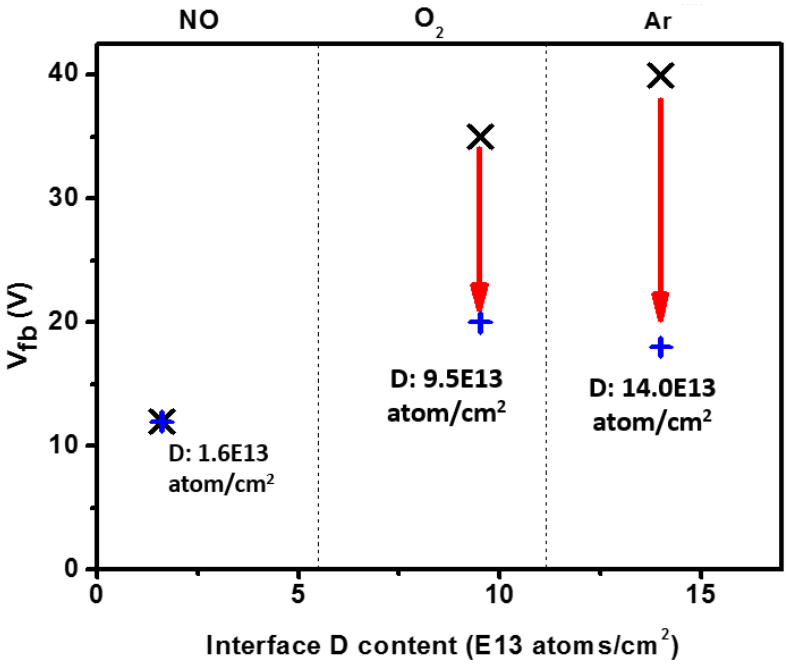

Figure 4.2.10, the flat band voltage before (black crosses) and after (blue +) water exposure after dry oxidation (the first box), dry oxidation + NO anneal (the second box) and dry oxidation + Ar anneal (the third box) as a function of the interface D content.

In the dry oxidation condition, there is $9.5x10^{13}/cm^2$ D at the interface introduced from the water vapor anneal. Also, the flat band voltage before the water exposure drops after the water exposure. Since the D remaining in the bulk oxide does not reflect any shift of the C-V curve, it is the D at the interface that changes the charge state and shifts the V_{fb}. The reduction of large positive flat band voltage after water exposure suggests that the D at the interface reduces the negative charge at the interface.

Water exposure for the Ar annealed sample introduces more D to the interface. As a result, the flat band voltage shift is larger.

The shift of flat band voltage as a function of the D detected at the interface is plotted in figure 4.2.11 for C-face SiC under all of the three conditions. It is clear that the change of the flat band voltage is linearly related to the D content at the interface.

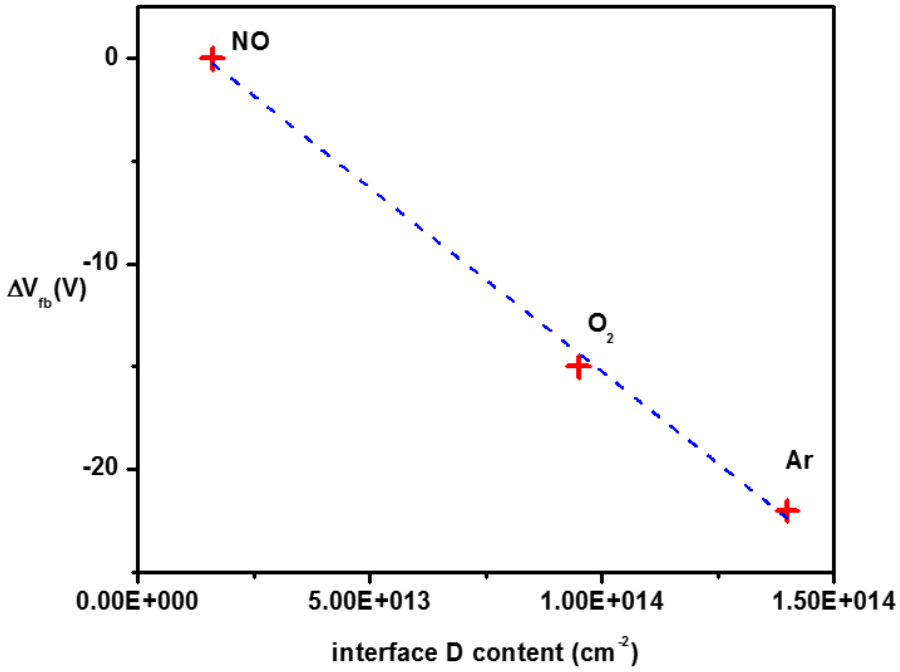

Figure 4.2.11, the shift of flat band voltage as a function of the interface D content.

The reduction of the large positive flat band voltage implies passivation of negatively charged states. The amount of negative charge reduced is calculated from

$$\mathrm{N} = \Delta \mathrm{V} \times C_{ox}/q \qquad \text{Equation (4.2.7)}$$

In which C_{ox} is the capacitance of the oxide and q is the charge of an electron. Based on equation 4.2.7, in the dry oxidation case, the amount of negative charge reduced is $8\text{x}10^{11}/\text{cm}^2$ while there is $9.5\text{x}10^{13}/\text{cm}^2$ D at the interface. In the Ar anneal case, the reduction of charge is $1.2\text{x}10^{12}/\text{cm}^2$, and the D content at the interface is $1.4\text{x}10^{14}/\text{cm}^2$. The change of charge states is negligible in the NO cases since ΔV is close to zero. Obviously the reduction of charge and the D content at the interface is not a one to one relation. Roughly only one percent of D is responsible to reduce the interface negative charge. This is not a surprise if one compares the reduction of interface defect and the nitrogen introduced in the NO process. On the carbon face, a NO anneal introduces $6\text{x}10^{14}/\text{cm}^2$ N at the interface [43], while the reduction of defects is $\sim 10^{13}/\text{cm}^2$ [8, 44]. The ratio of the defect reduced and the interface N is about 1%.

The deuterium at the interface reduces the negative charge states. It is natural to relate the defect density N_{it} to the interface D content. For as oxidized C-face SiC, the defect density at the interface is about $3\text{x}10^{13}/\text{cm}^2$ [44]. The D content we measure is $9.5\text{x}10^{13}/\text{cm}^2$. The NO anneal reduces the defect density to $\sim 10^{13}/\text{cm}^2$ [39] while the interface D content is reduced to $1.6\text{x}10^{13}/\text{cm}^3$. The interface defect density at the SiO_2/Si interface is $\sim 5\text{x}10^{11}/\text{cm}^2$ [45] and the amount of D at this interface is below the NRA detection limit. Therefore the deuterium accumulation at the interface is linearly related to the interface defect density.

It is not clear how the D related species interact with the interface. It has been reported that in the wet oxidation process in which water vapor is used for the source of oxygen, the defect density reduces near the valence band edge [46, 47]. A DFT study of H passivation suggests that H passivates the dangling bonds on the carbon atoms, which were created by Si vacancy formation [48]. The H passivation of carbon dangling bonds reduces the defect states near the valence band edge. The DOS plot obtained by Saleme et al is shown in figure 4.2.12 [48].

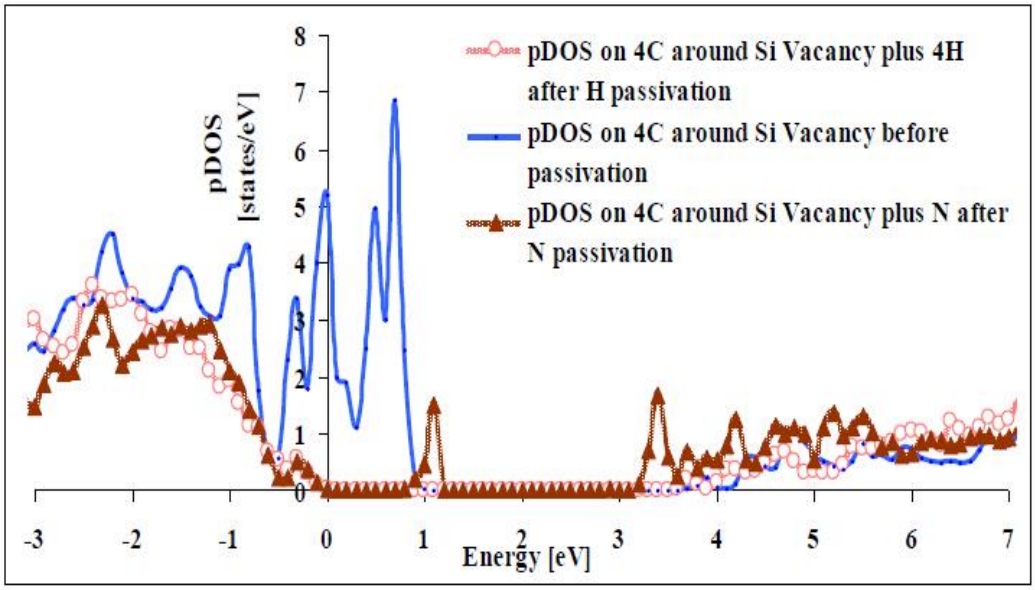

Figure 4.2.12, adapted from [48], pDOS of C atoms around a silicon vacancy before passivation (the blue line), pDOS of all carbon atoms together with four hydrogen atoms after H passivation (the pink line), and pDOS of all carbon atoms together with a nitrogen atom after N passivation (the brown line).

Figure 3.2.12 implies that for the carbon dangling bond defect, the H passivation works similarly as the N passivation. Those two passivation method possibly involve the same defect sites. If so, this explains the fact that the interface D content is reduced after N passivation.

The following conclusions can be made:

1) The C-face SiC structure absorbs more D at the interface than the SiO_2/Si structure. Equal amounts are absorbed in the bulk of these two oxides.
2) The NO anneal reduces the D content at the interface.
3) The shift of flat band voltage scales lineally with the amount of D at the interface.
4) The D at the interface is strongly correlated with the defect density. Many reports suggest that the deuterium passivates defects close to the valence band edge.

4.2.5 Deuterium absorption at Si-face SiC and a-face SiC.

The C-face SiC was selected as for the water absorption study in the previous section due to its high defect density at its interface with SiO_2 and its high oxidation rate. Ideally, the Si-face SiC (0001) has no carbon atoms in the top most layer. The C-face SiC (000-1) has only carbon atoms in the topmost layer. The a-face SiC (11-20) has 50% carbon atoms. Yoshioka et al. have reported that the defect states are different on the three faces [49]. They found that dry oxidation and NO post oxidation anneal reduces D_{it} and increases the election mobility on all three faces. The a-face has the highest

mobility. Pyrogenic oxidation which uses oxygen and H_2 for wet oxidation was employed in their study. The pyrogenic oxidation followed by the H_2 anneal creates an interface with even lower D_{it} and higher mobility on both the a-face and the C face. The same treatment on the Si-face has negligible effect. It is therefore important to study the physical and electrical behavior of hydrogen on the Si-face and the a-face. In this section, the same dry oxidation, post oxidation anneal and water anneal condition are performed on the Si-face SiC and the a-face SiC. Nuclear reaction analysis was applied to detect the D amount in the oxide and at the interface. The D content was correlated with C-V data.

The D content in the bulk oxide (total D – interface D) on the Si-face SiC, the a-face SiC is plotted with the C-face and the Si results in figure 4.2.13. No significant differences in D absorption were found. This agrees with the fact that the physical properties and electrical properties of SiO_2 bulk grown on Si and SiC are reported to be the same [50, 51].

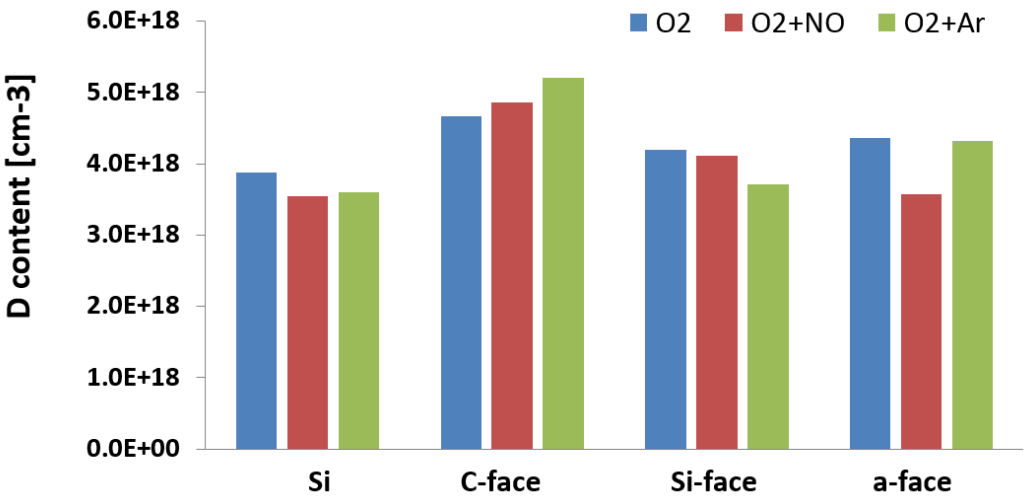

Figure 4.2.13, the deuterium content in the bulk oxide on the Si, the C-face SiC, the Si-face SiC and the a-face SiC. The blue bar represents dry oxidation only, the red bar represents dry oxidation + NO, and the green bar dry oxidation followed by Ar anneal.

The interface D content on Si and three crystal faces of SiC is plotted in Figure 4.2.14. For the case of dry oxidation only, the Si and Si-face SiC cases absorb more than one order less D than do the C-face and the a-face. These results agree well with the work of Yoshioka et al [49] on pyrogenic oxidation. Their observation of D_{it} reduction on the C-face and the a-face after pyrogenic oxidation + H_2 anneal while negligible effect on the Si-face could be understood as hydrogen passivates the surface on the C-face and the a-

face. The effect of D at the oxide/semiconductor interface is further studied by C-V measurements below.

NO post oxidation annealing reduced the D uptake at C-face SiC and a-face SiC. On Si and Si-face SiC, the D content before and after the NO process are both negligible. It is known that all crystal faces of SiC take up roughly the same amount of N at the interface in the NO anneal process [8, 43]. The Si face contains $4x10^{14}/cm^2$ while the C-face SiC and a-face SiC contain ~ $5x10^{14}/cm^2$ [43]. It is clear that interface nitrogen atoms bind with some defect sites on C-face and a-face SiC. Therefore the number of sites for D at the interface is highly reduced. Both the N and D at the interface passivate the interface defects. The types of defects those two atoms bind to are probably different. The N passivation is known to reduce the D_{it} while the water anneal in this study does not improve D_{it} much. One possible explanation is that the deuterium at the interface introduced by water vapor anneal mainly passivate the defect sites near the valence band edge. Therefore the D_{it} measurement is not sensitive to the D passivation. Nitrogen at the interface not only reduces the D_{it}, but also populate the defect sites that would otherwise be taken by D. Therefore nitrogen at the interface passivates defects all over the band gap.

The D contents increase in all of the four cases after Ar anneal. The conditions for the Ar and NO anneals were identical. It is obvious that the anneal temperature and time is not the reason for the reduction of the D absorption after NO anneal. The mechanism for the increasing D content on the Ar annealed sample is not clear. It is possible that during the high temperature Ar anneal (1175^{o}C), a small portion of oxygen remaining in the

environment creates a new oxide/semiconductor interface that contains more defect sites for deuterium.

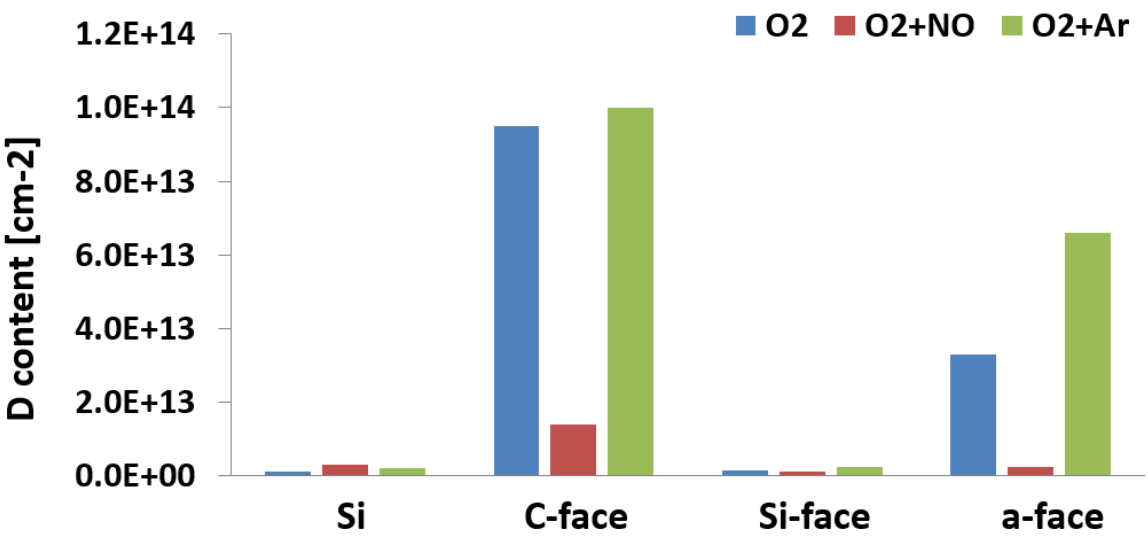

Figure 4.2.14, the interface D content on Si and three crystal faces of SiC. The blue bar represents dry oxidation only, the red bar represents dry oxidation + NO anneal, and the green bar is dry oxidation + Ar anneal.

Like in the C-face case, the effect of the D_2O vapor anneal on device performance was studied by the shift of the C-V curve. The shifts of the flat band voltage before and after D_2O vapor anneal as a function of the D interface content are plotted in figure 4.2.15. The negative value of the flat band voltage change implies a reduction of negative oxide/interface charge.

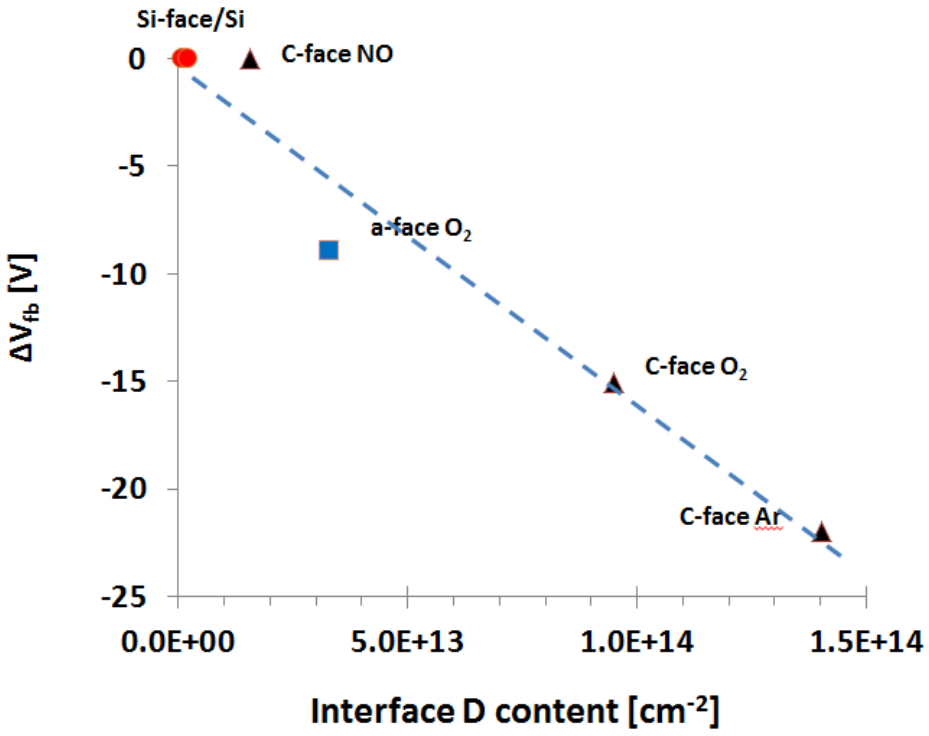

Figure 4.2.15, the shifts of the flat band voltage before and after D_2O vapor anneal as a function of the D content at the interface. The Si, the Si-face SiC, the C-face SiC and the a-face SiC are included.

For the Si and Si-face SiC cases, there are little D measured at the interface, and no C-V shift was observed. The C-V shift is lineally correlated with the interface D amount. The C-face SiC Ar anneal has the largest C-V shift, as well as the most interface D. It is

followed by the C-face dry oxidation, the a-face dry oxidation and C-face NO anneal in order.

As discussed in the beginning of this chapter, the NRA study does not reveal the state of the deuterium atoms, which could be –D, -OD, D_2O etc. On the carbon face, it has been reported that after HF etch, the C-face surface terminates with O-H groups. The Si face terminates with a layer of oxygen and no evidence of O-H bonding at the interface [52]. The different behavior between the crystal faces further complicates the determination of the state of the deuterium atoms.

4.3 Summary

The SiO_2 grown on the Si, the Si-face SiC, the C-face SiC and the a-face SiC structures were exposed to heavy water vapor (D_2O) to study the absorption of hydrogen (or more specifically deuterium). The D content in the structure was measured by NRA and was correlated to the shift of the C-V curve. We find that: (1) The bulk of the oxides on Si and all faces of SiC behave essentially the same with respect to deuterium accumulation; (2) there is a significant difference in accumulation of deuterium at the semiconductor/dielectric interface, the C-face SiC/SiO_2 and a-face SiC/SiO_2 structures absorb one order of magnitude more deuterium than the Si-face SiC/SiO_2 and Si/SiO_2 structures (3) standard interface passivation schemes such as NO annealing greatly reduce the interfacial D accumulation; and (4) the effective interfacial charge after D_2O exposure is proportional to the total D amount at the interface.

References:

1. Kimoto, T. and J.A. Cooper, *Unipolar Power Switching Devices*, in *Fundamentals of Silicon Carbide Technology*. 2014, John Wiley & Sons Singapore Pte. Ltd. p. 301-352.
2. Gaskill, D.K., *Epitaxial Graphene*, in *Handbook of Crystal Growth: Thin Films and Epitaxy*, T. Kuech, Editor. 2014, Elsevier Science. p. 755.
3. Sudarshan, T.S. and S.I. Maximenko, *Bulk growth of single crystal silicon carbide.* Microelectronic Engineering, 2006. **83**(1): p. 155-159.
4. Peter Friedrichs, T.K., Lothar Ley, and Gerhard Pensl, in *Silicon Carbide: Volume 1: Growth, Defects, and Novel Applications.* 2011, John Wiley & Sons, .
5. Dhar, S., *Nitrogen and Hydrogen Induced Trap Passivation at the SiO2/4H-SiC Interface*, in *Materials Science and Engineering*. 2005, Vanderbilt University.
6. Kern, W., *The Evolution of Silicon Wafer Cleaning Technology.* Journal of The Electrochemical Society, 1990. **137**(6): p. 1887-1892.
7. Soukiassian, P. and F. Amy, *Silicon carbide surface oxidation and SiO2/SiC interface formation investigated by soft X-ray synchrotron radiation.* Journal of Electron Spectroscopy and Related Phenomena, 2005. **144–147**(0): p. 783-788.
8. Xu, Y., et al., *Atomic state and characterization of nitrogen at the SiC/SiO2 interface.* Journal of Applied Physics, 2014. **115**(3): p. 033502.
9. Deak, P., et al., *The mechanism of defect creation and passivation at the SiC/SiO2 interface.* Journal of Physics D-Applied Physics, 2007. **40**(20): p. 6242-6253.
10. Devynck, F., et al., *Charge transition levels of carbon-, oxygen-, and hydrogen-related defects at the SiC/SiO2 interface through hybrid functionals.* Physical Review B, 2011. **84**.
11. Shen, X. and S.T. Pantelides, *Oxidation-induced epilayer carbon di-interstitials as a major cause of endemically poor mobilities in 4H-SiC/SiO2 structures*, in *Silicon Carbide and Related Materials 2011, Pts 1 and 2*, R.P. Devaty, et al., Editors. 2012. p. 445-448.
12. Rozen, J., et al., *Scaling Between Channel Mobility and Interface State Density in SiC MOSFETs.* Electron Devices, IEEE Transactions on, 2011. **58**(11): p. 3808-3811.
13. Shen, X., et al., *Excess carbon in silicon carbide.* Journal of Applied Physics, 2010. **108**(12): p. 123705.
14. Afanasev, V.V., et al., *Intrinsic SiC/SiO2 Interface States.* physica status solidi (a), 1997. **162**(1): p. 321-337.
15. Harris, G.L. and INSPEC, *Properties of Silicon Carbide*. 1995: INSPEC, Institution of Electrical Engineers.
16. Pennington, G. and C.R. Ashman, *Nitrogen passivation of (0001) 4H-SiC silicon-face dangling bonds.* Applied Physics Letters, 2007. **91**(7): p. 072106.
17. Chung, G.Y., et al., *Effect of nitric oxide annealing on the interface trap densities near the band edges in the 4H polytype of silicon carbide.* Applied Physics Letters, 2000. **76**(13): p. 1713-1715.
18. Chung, G.Y., et al., *Improved inversion channel mobility for 4H-SiC MOSFETs following high temperature anneals in nitric oxide.* Electron Device Letters, IEEE, 2001. **22**(4): p. 176-178.

19. Chung, G.Y., et al., *Interface state density and channel mobility for 4H-SiC MOSFETs with nitrogen passivation.* Applied Surface Science, 2001. **184**(1–4): p. 399-403.
20. Li, H.F., et al., *Interfacial characteristics of N2O and NO nitrided SiO2 grown on SiC by rapid thermal processing.* Applied Physics Letters, 1997. **70**(15): p. 2028-2030.
21. Afanas'ev, V.V. and A. Stesmans, *Hydrogen-Induced Valence Alternation State at SiO2 Interfaces.* Physical Review Letters, 1998. **80**(23): p. 5176-5179.
22. Afanas'ev, V.V. and A. Stesmans, *Positively charged bonded states of hydrogen at the (111)Si/SiO2 interface.* Journal of Physics: Condensed Matter, 1998. **10**(1): p. 89.
23. Afanas'ev, V.V. and A. Stesmans, *H-complexed oxygen vacancy in SiO2: Energy level of a negatively charged state.* Applied Physics Letters, 1997. **71**(26): p. 3844-3846.
24. Wang, S., et al., *Bonding at the SiC/SiO2 Interface and the Effects of Nitrogen and Hydrogen.* Physical Review Letters, 2007. **98**(2): p. 026101.
25. Sze, S.M.N.K.K., *Physics of semiconductor devices*. 2007, Hoboken, N.J.: Wiley-Interscience.
26. Endo, T., et al., *High Channel Mobility of MOSFET Fabricated on 4H-SiC (11-20) Face Using Wet Annealing.* Silicon Carbide and Related Materials 2007, Pts 1 and 2, 2009. **600-603**: p. 691-694.
27. Okamoto, M., et al., *Improvement of Channel Mobility in 4H-SiC C-face MOSFETs by H-2 Rich Wet Re-Oxidation.* Silicon Carbide and Related Materials 2013, Pts 1 and 2, 2014. **778-780**: p. 975-978.
28. Mihovilovic, M., *Dolocanje globinske porazdelitve devterija z jedrsko reakcijo D(3He, p)α.* Univerzav Ljubljani, podiplomski seminar, 2008.
29. Baumvol, I.J.R., et al., *Nuclear reaction analysis of deuterium in ultrathin films of SiO2 on Si.* Nuclear Instruments and Methods in Physics Research Section B: Beam Interactions with Materials and Atoms, 1998. **136–138**(0): p. 204-208.
30. Alimov, V.K., M. Mayer, and J. Roth, *Differential cross-section of the D(3He,p)4He nuclear reaction and depth profiling of deuterium up to large depths.* Nuclear Instruments and Methods in Physics Research Section B: Beam Interactions with Materials and Atoms, 2005. **234**(3): p. 169-175.
31. Ziegler, J.F., J.P. Biersack, and U. Littmark, *The Stopping and Range of Ions in Solids*. 1985: Pergamon.
32. Dhar, S., et al., *Interface trap passivation for SiO2 ／(0001 ¯) C-terminated 4H-SiC.* Journal of Applied Physics, 2005. **98**(1): p. 014902.
33. Nicollian, E.H., et al., *Electrochemical Charging of Thermal SiO2 Films by Injected Electron Currents.* Journal of Applied Physics, 1971. **42**(13): p. 5654-5664.
34. Soares, G.V., et al., *H Quantification and Profiling in SiO2 / SiC Submitted to Annealing in Water Vapor.* Electrochemical and Solid-State Letters, 2010. **13**(11): p. G95-G97.
35. Corrêa, S.A., et al., *Unraveling the role of SiC or Si substrates in water vapor incorporation in SiO2 films thermally grown using ion beam analyses.* Nuclear Instruments and Methods in Physics Research Section B: Beam Interactions with Materials and Atoms, 2012. **273**(0): p. 139-141.
36. Pitthan, E., et al., *SiO2/SiC structures annealed in D218O: Compositional and electrical effects.* Applied Physics Letters, 2014. **104**(11): p. 111904.
37. Stesmans, A., *Interaction of Pb defects at the (111)Si/SiO2 interface with molecular hydrogen: Simultaneous action of passivation and dissociation.* Journal of Applied Physics, 2000. **88**(1): p. 489-497.
38. Crank, J., *The mathematics of diffusion*. Oxford science publications. 1975: Clarendon Press.

39. Chen, Z., *Electrical Properties of Mos Devices Fabricated on 4h Carbon-Face Silicon Carbide*. 2011: BiblioBazaar.
40. Sze, S.M. and K.K. Ng, *Physics of Semiconductor Devices*. 2006: Wiley.
41. Nicollian, E.H. and J.R. Brews, *MOS (metal oxide semiconductor) physics and technology*. 1982: Wiley.
42. Snow, E.H., et al., *Ion Transport Phenomena in Insulating Films.* Journal of Applied Physics, 1965. **36**(5): p. 1664-1673.
43. Chen, Z., et al., *Kinetics of nitrogen incorporation at the SiO2/4H-SiC interface during an NO passivation.* Applied Surface Science, 2014. **317**(0): p. 593-597.
44. Afanas'ev, V.V., et al., *Contributions to the Density of Interface States in SiC MOS Structures*, in *Silicon Carbide*, W.J. Choyke, H. Matsunami, and G. Pensl, Editors. 2004, Springer Berlin Heidelberg. p. 343-371.
45. White, M.H. and J.R. Cricchi, *Characterization of thin-oxide MNOS memory transistors.* Electron Devices, IEEE Transactions on, 1972. **19**(12): p. 1280-1288.
46. Okamoto, M., et al., *Effect of the oxidation process on the electrical characteristics of 4H-SiC p-channel metal-oxide-semiconductor field-effect transistors.* Applied Physics Letters, 2006. **89**(2): p. 023502-023502-3.
47. Palmieri, R., et al., *Effect of the oxidation process on SiO2/4H-SiC interface electrical characteristics.* Applied Surface Science, 2008. **255**(3): p. 706-708.
48. Salemi, S., et al., *The effect of defects and their passivation on the density of states of the 4H-silicon-carbide/silicon-dioxide interface.* Journal of Applied Physics, 2013. **113**(5): p. 053703.
49. Yoshioka, H., et al., *Effects of interface state density on 4H-SiC n-channel field-effect mobility.* Applied Physics Letters, 2014. **104**(8): p. 083516.
50. Johnson, M.B., M.E. Zvanut, and O. Richardson, *HF chemical etching of SiO2 on 4H and 6H SiC.* Journal of Electronic Materials, 2000. **29**(3): p. 368-371.
51. Gurfinkel, M., et al., *Time-Dependent Dielectric Breakdown of 4H-SiC/SiO2 MOS Capacitors.* Device and Materials Reliability, IEEE Transactions on, 2008. **8**(4): p. 635-641.
52. Dhar, S., et al., *Chemical Properties of Oxidized Silicon Carbide Surfaces upon Etching in Hydrofluoric Acid.* Journal of the American Chemical Society, 2009. **131**(46): p. 16808-16813.

Chapter 5

Indium and bismuth inter-diffusion

and its influence on the mobility in In_2Se_3/Bi_2Se_3

5.1 Some properties of topological insulators

Topological insulators have insulating election states in the bulk just as ordinary insulators, but have conducting surface states [1, 2]. These states originate in a strong spin orbit coupling. These edge states have definite electron spin properties. Due to the spin orbit coupling, the spin up electrons on the edge see an effective B-field in the opposite direction as the spin down electrons do [3]. Therefor the spin and the momentum are coupled and the spin up and the spin down electrons flow in the opposite directions. The total spin current flows in one direction and is immune to back scattering. This phenomenon is called the quantum spin hall effect. The quantum spin hall effect was first predicted in graphene by Kane et al. [4]. However, Min et al. showed that the bandgap in graphene is not large enough to observe the quantum spin hall effect [5]. A 2-D structure of $Hg_xCd_{1-x}Te/HgTe/ Hg_xCd_{1-x}Te$ was proposed Zhang et al. to observe the quantum spin hall effect [6] and that was the first experimental observation [7].

Among all of the 3-D topological insulators, Bi_2Se_3 is of interest because of its relatively large band gap of 0.3eV. In_2Se_3 is used in some conditions as band insulator on Bi_2Se_3 based devices due to its good chemical and structural compatibility with Bi_2Se_3. In_2Se_3

has a band gap of 1.2-1.3eV [8, 9]. It has been reported that indium in the Bi_2Se_3 causes a phase transition of the $(Bi_{1-x}In_x)_2Se_3$ structure from a topological insulator to a traditional band insulator [10]. Therefore for the In_2Se_3/Bi_2Se_3 structure, it is important to study if indium diffuses into the Bi_2Se_3 and how it affects the corresponding electrical properties.

In this chapter, the inter diffusion of indium and bismuth in the In_2Se_3/Bi_2Se_3 structure is studied by MEIS. The content of the indium diffused in to the Bi_2Se_3 layer is correlated with the transport properties.

5.2 Experiment

The unit cell of the Bi_2Se_3 contains five layers in the order of Se-Bi-Se-Bi-Se along the c axis. This is known as a quintuple layer (QL). The thickness of a quintuple layer is about 9.6 Å. It has been reported that Bi_2Se_3 grown on an Al_2O_3 substrate is more uniform than on a Si substrate [11]. A uniform film with minimum roughness is critical for MEIS depth profile modeling. In this work, 3 QL of Bi_2Se_3 are grown on the Al_2O_3 substrate by molecular beam epitaxy (MBE) at 110^{o}C. After that, the film is further annealed at 220^{o}C for 20 min to form a better crystal structure. 5 QL of In_2Se_3 was grown on top of the Bi_2Se_3. To study the behavior of In and Bi inter diffusion as a function of temperature, three temperatures were used for the In_2Se_2 growth, 50^{o}C, 125^{o}C and 220^{o}C.

The four probe van der Pauw method [12] was used to measure the carrier density and the mobility. The average resistivity of a sample is given by

$$\rho = R_s \times t \qquad \text{(Equation 5.2.1)}$$

in which R_s is the sheet resistance and t is the sample thickness. We assume the sample is square, and the four corners are labeled as 1,2,3,4 in order. In the van der Pauw method, a current is applied across one edge of the sample I_{12}, and the voltage is measured on the opposite edge V_{34}. The resistance is by Ohm's law then $R_{12,34}= V_{12}/I_{34}$. The corresponding measurement on the vertical two edges gives $R_{23,41}=V_{23}/I_{41}$. The van der Pauw formula is used to calculate the sheet resistance [12].

$$e^{-\pi R_{12,34}/R_S} + e^{-\pi R_{23,41}/R_S} = 1 \qquad \text{(Equation 5.2.2)}$$

When $R_{12,34}=R_{23,41}=R$, the formula is rearranged to

$$R_s = \frac{\pi R}{Ln2} \quad . \qquad \text{(Equation 5.2.3)}$$

The resistance of a semiconductor is

$$\rho = \frac{1}{q(n\mu_n + p\mu_p)} \qquad \text{(Equation 5.2.4)}$$

Generally, one type of doping dominates, and the doping level and doping type can be measured from the Hall measurement.

$$V_H = \frac{IB}{qnd} = \frac{IB}{qn_s} \qquad \text{(Equation 5.2.5)}$$

where V_H is the Hall voltage, I is the current, B is the magnet field, n is the doping level in atoms/cm^3 and n_s is defined to be the sheet density, the doping density times the thickness.

Assuming it is an n-type with doping level n, the expression of the resistance is further reduced to

$$\rho = \frac{1}{qn\mu_n} \quad \text{(Equation 5.2.6)}$$

From equation 5.2.1, the sheet resistance is the resistance per thickness. Using the definition of sheet density, the sheet resistance is

$$R_s = \frac{1}{qn_s\mu_n} \quad \text{(Equation 5.2.7)}$$

Therefore the mobility after rearrangement is

$$\mu_n = \frac{1}{qn_sR_s} \quad \text{(Equation 5.2.8)}$$

In which n_s is measured from the Hall Effect and calculated from equation 5.2.5 and R_s is calculated from equation 5.2.3.

The transport measurements were done at 6K. The magnetic field varied from -0.6T to +0.6T.

After the transport measurements, the samples were measured by MEIS with a 190keV He^+ beam. The ion beam channeling measurement was done to study the surface structure and the degree of crystallinity. Random incident measurements were performed at 5 degree off the normal direction to measure the absolute amounts of In, Bi and Se as well as their depth distribution. The scattering angle for both the channeling and the random incident measurements was 139°.

To simulate the energy spectrum, the thin film is divided into ~1nm thin. The yield from each slice is calculated from equation 2.2.4 and the energy loss is from an available data base by Ziegler [13]. Straggling is calculated with Lindhard and Scharff model (equation

2.2.18). The MEIS simulation program used in this work is written by Tomoaki Nishimura [14]. The parameters of those thin slices in the model as an input include, aside from the layer thickness, density, the composition of each layer and the channeling probability of each element if the channeling effect in a crystal needs to be considered. The absolute concentration and depth profile of species in the film is determined from the best fit of the experimental energy spectrum.

5.3 Results and discussion

Figure 5.3.1 shows the random incidence MEIS spectrum of the sample with 220^{o}C In_2Se_3 growth temperature together with a simulation for an ideal model (sharp interface) of 5QL In_2Se_3 on 3QL Bi_2Se_3.

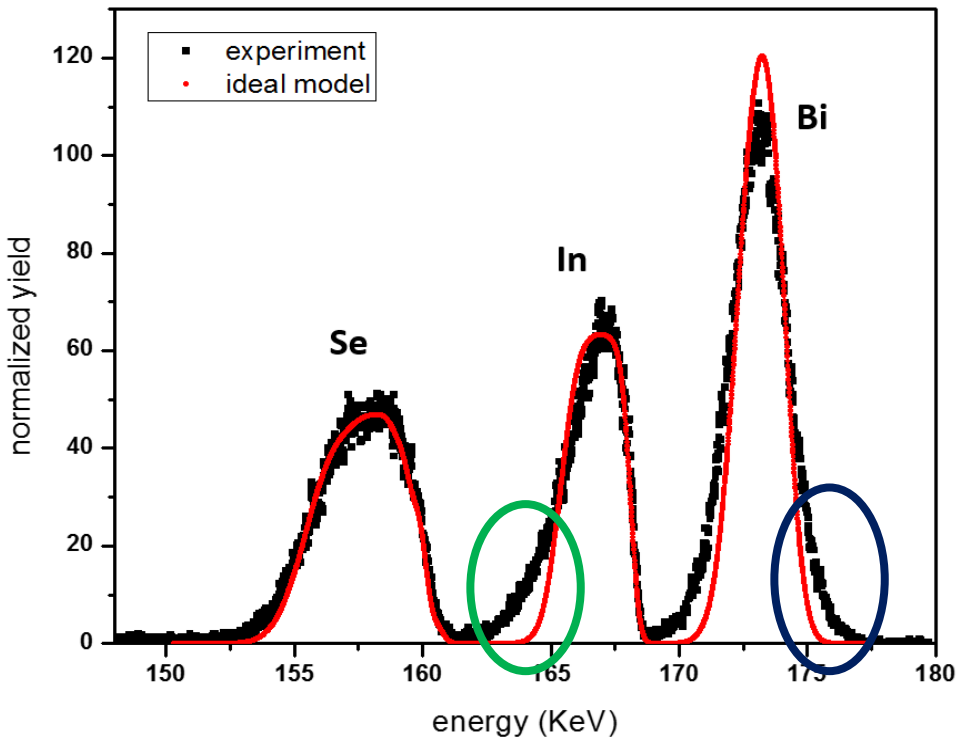

Figure 5.3.1 MEIS random incidence spectrum of the sample at 220°C In_2Se_3 growth temperature. The red line is the simulation with an ideal model.

The ideal model simulation assumes an abrupt In_2Se_3/Bi_2Se_3 interface with no indium and bismuth interdiffusion. The Bi peak is broader than the simulated one, in particular it extends to higher energies (the blue circle). This indicates that bismuth diffuse up into the In_2Se_3 layer above it. The lower energy part of the indium peak extends to lower energies than calculated (the green circle), meaning that indium diffuses into the Bi_2Se_3 layer below. Therefore the MEIS spectrum is a strong evidence that a layer of $(Bi_{1-x}In_x)_2Se_3$ exists at the In_2Se_3/Bi_2Se_3 interface. Similar results were observed for samples

grown at 130°C and the 50°C. Quantitatively, the amount of inter diffusion is smaller at lower growth temperature.

The energetic He^+ particles may collide with the atoms in the sample target and cause a collision cascade. Therefore it is possible that the diffusion observed here is partially due to the ion beam effect. The He^+ beam dose applied in this experiment was ~ $2x10^{16}$ atoms/cm^2. SRIM simulation was used to simulate the collision cascade [15]. The distribution of the dislocated indium atoms is shown in figure 5.3.2.

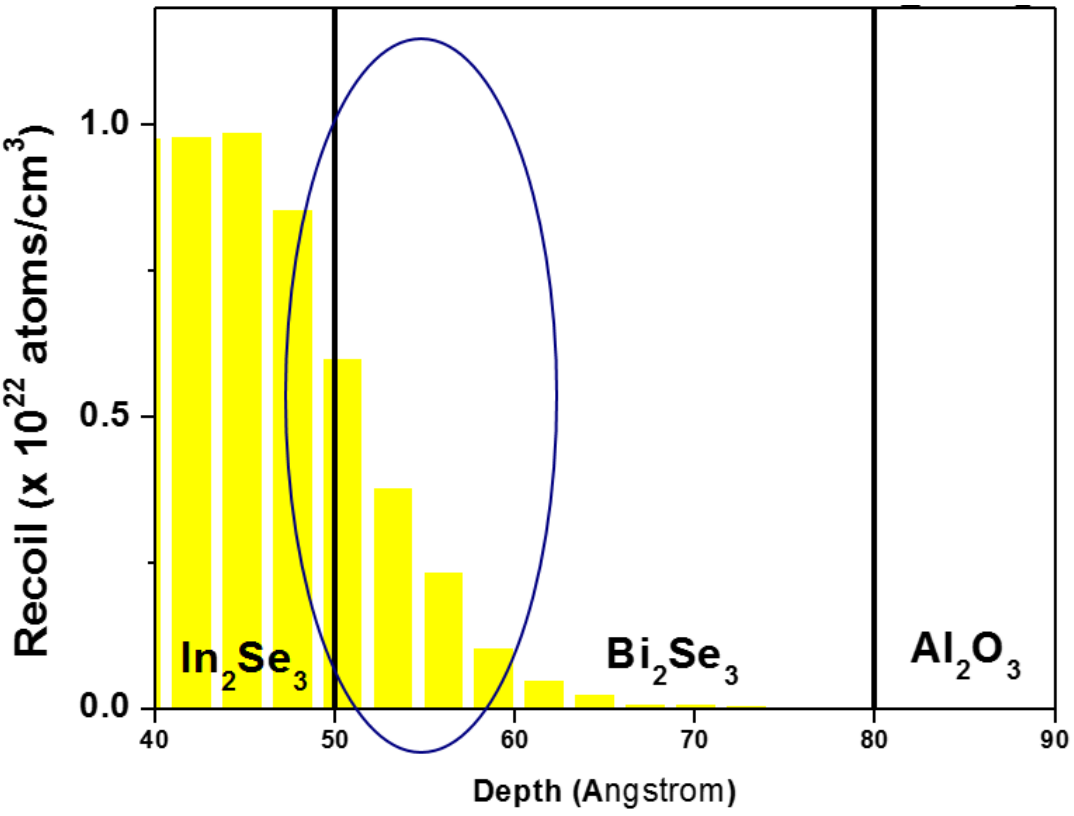

Figure 5.3.2, SRIM simulation of the distribution of the dislocated Indium atoms by ion beam.

As seen in figure 5.3.2, there is a small amount of indium scattered into the Bi_2Se_3 layer due to the ion beam collision cascade (the blue circle). This dislocation is largely confined to ~1nm in the in Bi_2Se_3 layer. Figure 5.3.3 shows the simulation of an ideal model involving the ion beam recoil effect for Bi and In peak, together with the experiment and the ideal model without considering recoils.

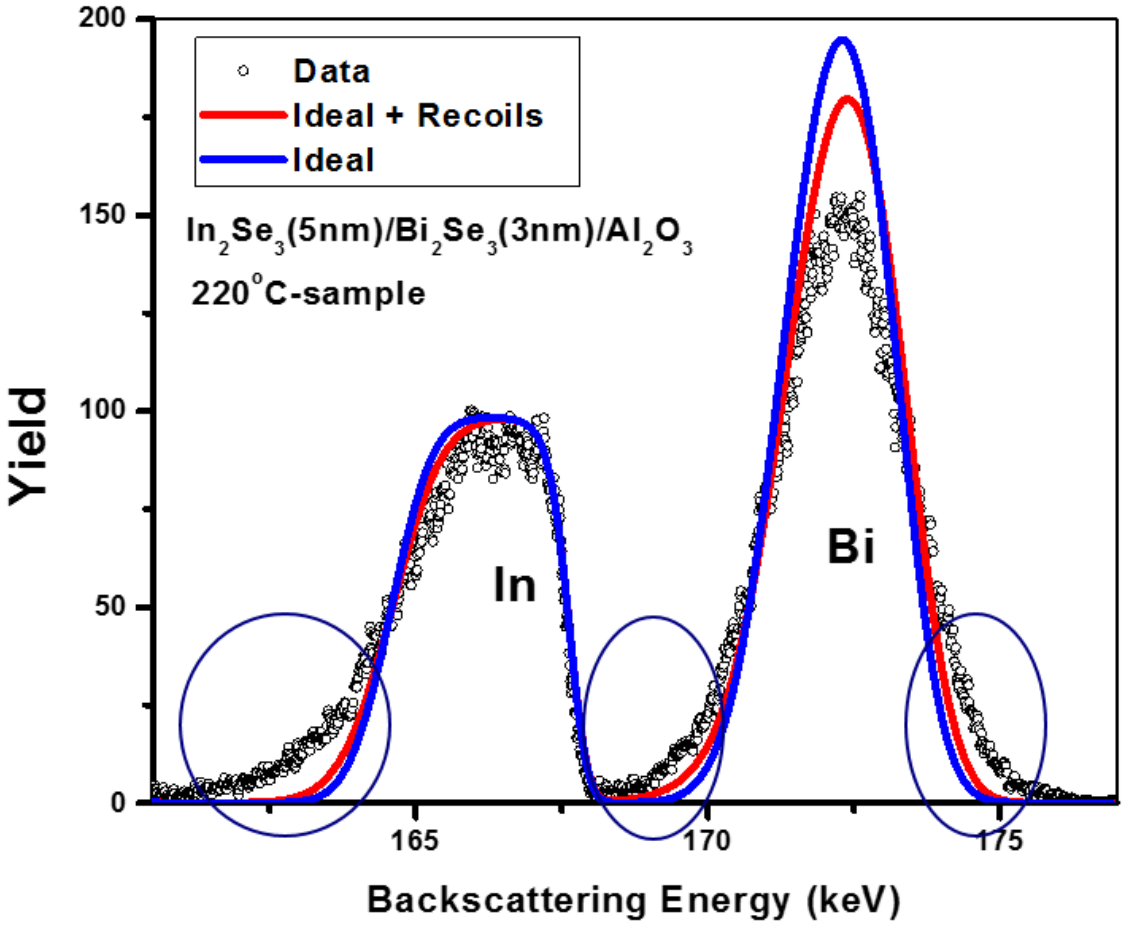

Figure 5.3.3, a comparison of ideal+recoil model with the ideal model and the data.

Figure 5.3.3 suggests that the recoil effect introduces a small correction to the ideal model but is not enough to explain the difference between the ideal model and the data. It is clear that the In and Bi inter diffusion is the reason for the lack of agreement. The ion beam effect is proportional to the beam dose. To experimentally prove that the ion beam recoil effect is not critical in this experiment, a separate measurement with a dose of ~1.3×10^{15} atoms/cm^2 was applied on another sample to compare with the regular measurement with a dose of ~2×10^{16} atoms/cm^3. The comparison is shown in figure 5.3.4 with the small dose measured indium peak in the blue dots, the small dose measured bismuth peak in the red dots and the regular measurement in black.

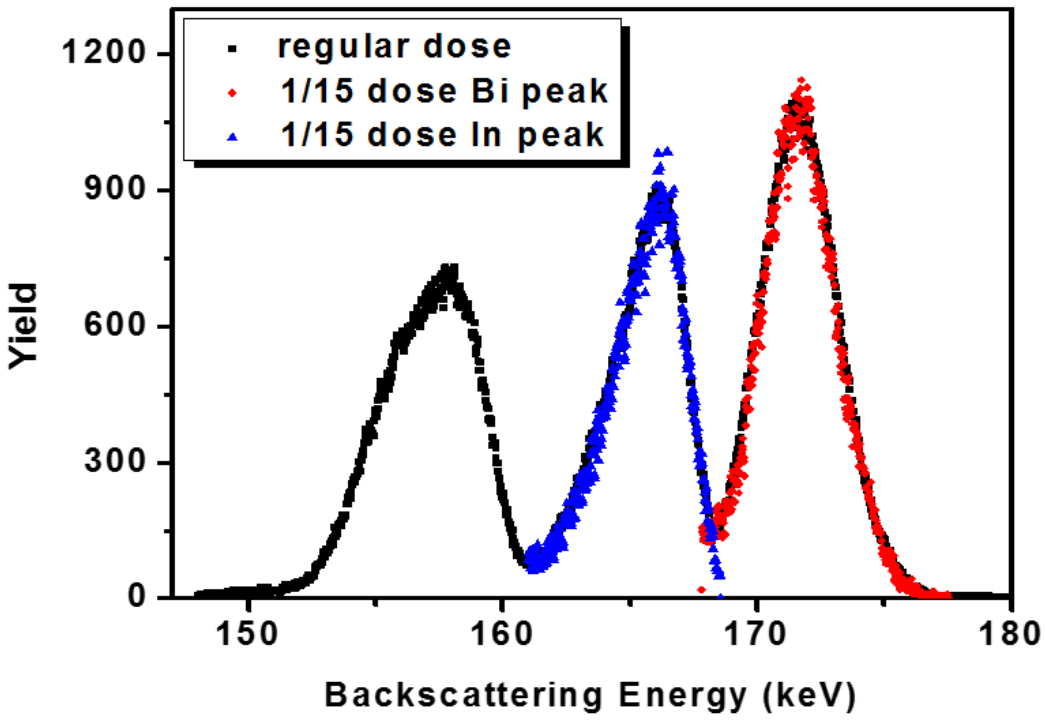

Figure 5.3.4, comparison of small beam dose measurement and regular beam dose measurement.

The small dose measurement and the regular dose measurement show no observable differences. This is a further evidence that ion beam induced recoil dose not contribute much to the inter diffusion.

The MEIS channeling spectrum contains information about the crystal structure. For an ideal crystal, the channeling spectrum shows only the surface peak, as discussed in detail in Chapter 3. The channeling spectrum is the same as the random spectrum for an amorphous film. Therefore the ratio of the peak height in the channeling spectrum and in the random spectrum reflects the degree of crystallinity - the lower the channeling intensity, the better the crystallinity. The channeling spectrum (the red dots) is plotted together with the random spectrum (the black dots) for 50^{o}C (figure 5.3.5 (a)), 135^{o}C (figure 5.3.5 (b)) and 220^{o}C (figure 5.3.5 (c)) growth of In_2Se_3. Note that for all of the three samples, the growth and the annealing temperature are the same.

At 50^{o}C, the indium peak in channeling incidence and random incidence almost overlap. This suggests that at this temperature the In_2Se_3 layer has close to an amorphous structure. At 135^{o}C, the indium peak in the channeling spectrum has much lower intensity than at random incidence. It means that at higher temperature, the In_2Se_3 film has better crystallinity. The film grown at 220^{o}C has the best crystallinity of the three.

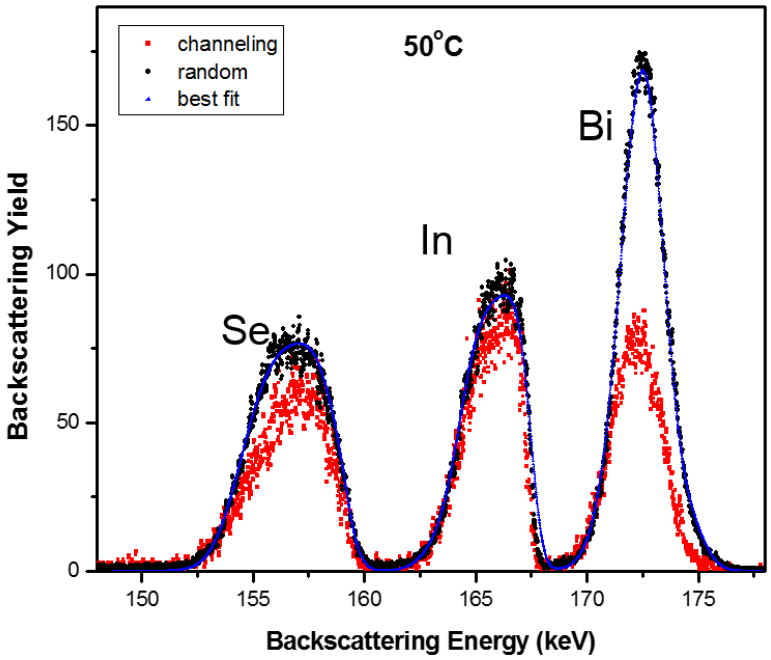

Figure 5.3.5 (a), channeling and random incidence spectrum of 50°C growth In_2Se_3.

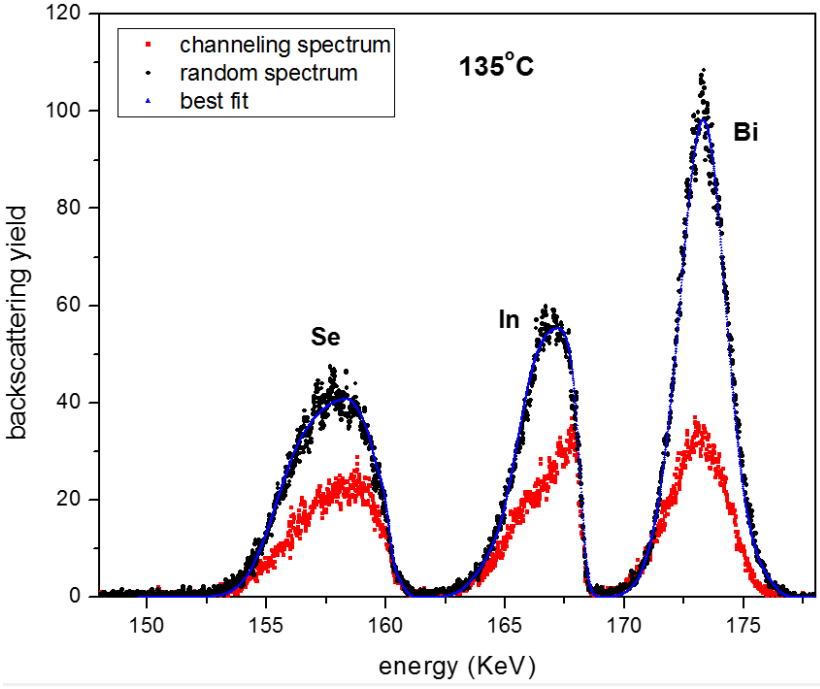

Figure 5.3.5 (b), channeling and random incidence spectrum of 135°C growth In_2Se_3.

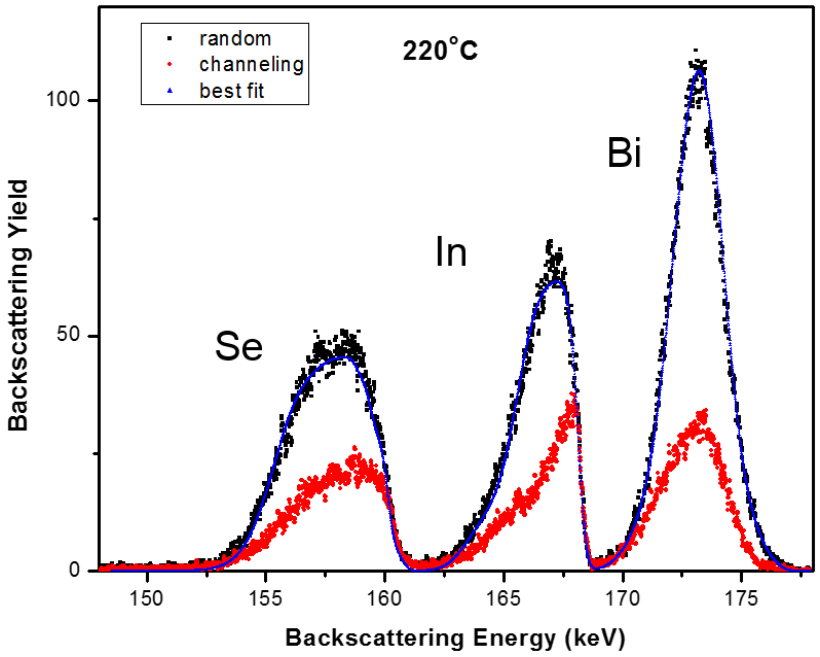

Figure 5.3.5 (c), channeling and random incidence spectrum of 220°C growth In_2Se_3.

The depth resolution of MEIS near the surface is sub nanometer. Therefore it is possible to estimate the amount of indium and bismuth in every single quintuple layers by dividing the film into thin slices of one quintuple layer (~1nm) thickness. Figure 5.3.6 shows the Indium content diffuses into every Bi_2Se_3 quintuple layers for all the three growth temperatures. In the first QL, the indium content is almost the same for all the three growth temperatures. In the second and the third quintuple layer, the film grown at 50^{o}C shows less diffusion.

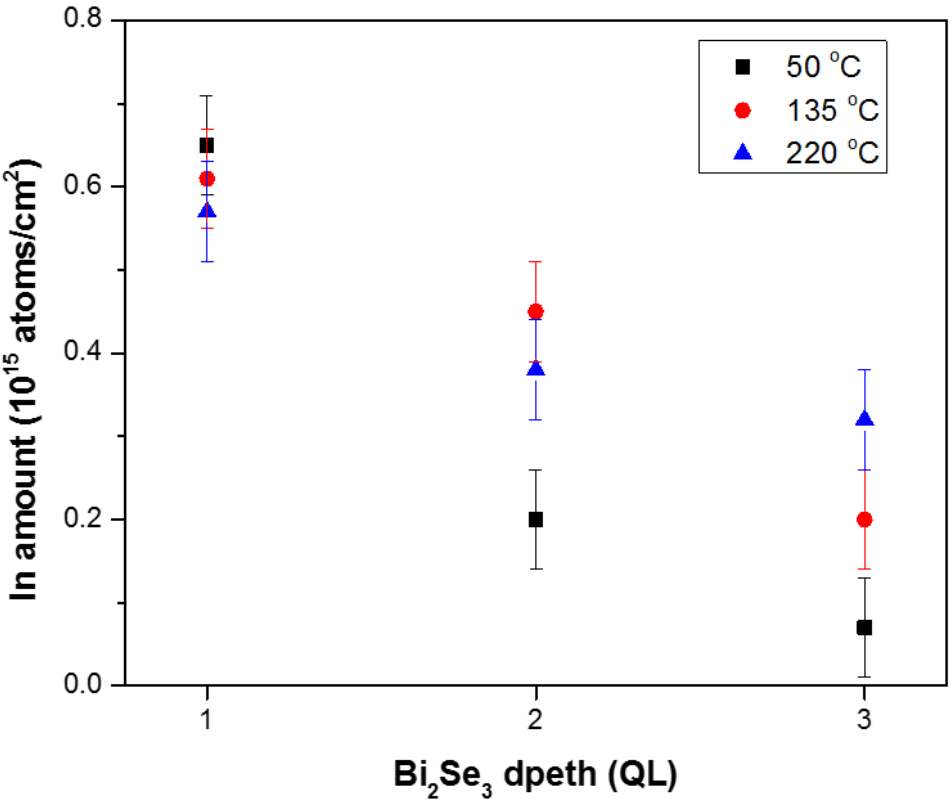

Figure 5.3.6, layer by layer depth profile of indium diffusion into the 3QL Bi_2Se_3.

Table 5.3.1 summarizes the total amount of bismuth in the Bi_2Se_3 film and the total indium content diffused into the Bi_2Se_3 film. The x in the $(Bi_{1-x}In_x)_2Se_3$ structure is calculated in the last column to compare with the report of phase transition as a function of x [10]. Due to the bismuth up-diffusion into the In_2Se_3 layer, the bismuth amount is smaller than in the ideal Bi_2Se_3 structure: The higher the In_2Se_3 growth temperature, the more bismuth diffusion. For all the In_2Se_3 growth temperatures, the x values in $(Bi_{1-x}In_x)_2Se_3$ are larger than 0.2.

Sample	Bi in Bi_2Se_3 layer ($x10^{15}/cm^2$)	In in Bi_2Se_3 layer ($x10^{15}/cm^2$)	X in $(Bi_{1-x}In_x)_2Se_3$
ideal	3.96	0	0
50°C	3.73	0.92	0.20
135°C	3.20	1.26	0.28
220°C	2.91	1.27	0.30

Table 5.3.1, total amount of Bismuth and Indium in the Bi_2Se_3 layer.

The mobility measured by van der Pauw method is plotted as a function of x in $(Bi_{1-x}In_x)_2Se_3$ for the three samples in figure 5.3.7. As expected, the more indium diffuses in to the Bi_2Se_3 layer, the lower the mobility, in agreement with a previous report [10].

However, it was earlier claimed that for x larger than 0.2, the $(Bi_{1-x}In_x)_2Se_3$ behaves like an insulator [10]. We observed high mobility as well as metallic behavior (resistance increase with temperature) as shown in the inset for the 50^oC growth In_2Se_3. The higher growth temperature samples show similar metallic behavior though lower mobility. A possible reason is that though the average x value is greater than 0.2, the indium atoms are concentrated in the first QL of Bi_2Se_3 layer, leaving the 2nd and the 3rd layers close to the ideal structure as shown is figure 5.3.6.

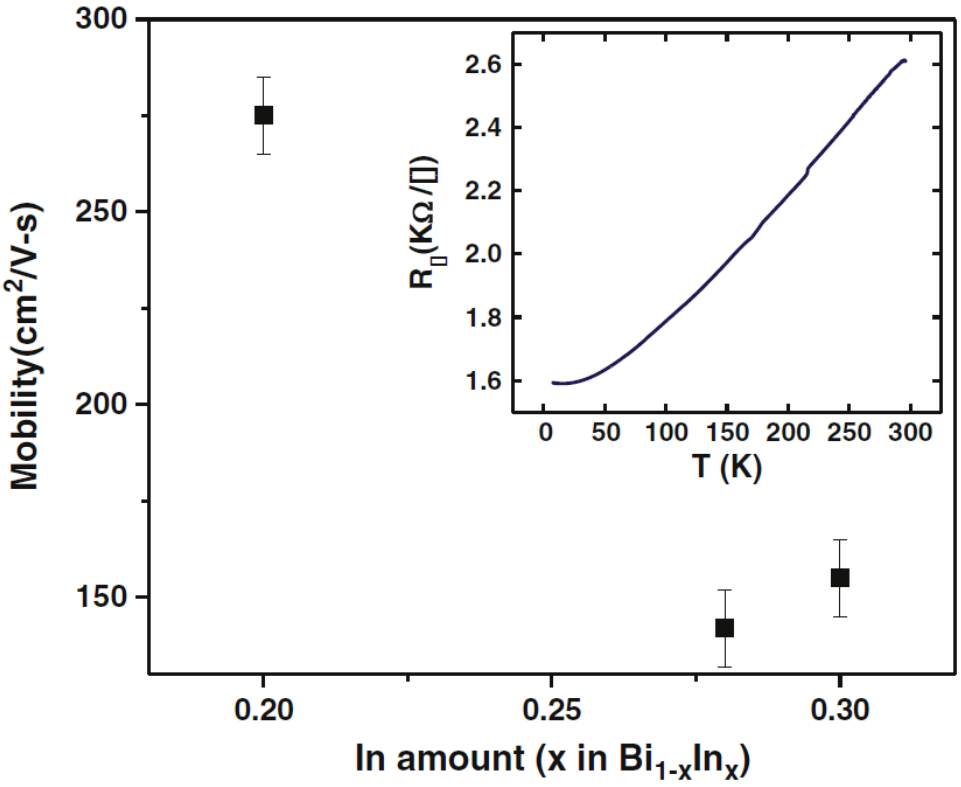

Figure 5.3.7, mobility as a function of Indium amount in the Bi_2Se_3 layer, represented by x value in the $(Bi_{1-x}In_x)_2Se_3$. The inset shows the temperature dependence of the sheet resistance for the film grown at 50°C.

Indium diffuses to the last layer of Bi_2Se_3 even at the lowest growth temperature (figure 5.3.6). A question is how deep the indium diffuses to if the Bi_2Se_3 layer is thick. To answer this question, a 7 QL Bi_2Se_3 was grown. In_2Se_3 was then grown on the 7QL Bi_2Se_3 at 50°C. The depth distribution of indium in the Bi_2Se_3 layers was studied by MEIS and the layer by layer indium concentration is plotted in figure 5.3.8 together with the 3QL Bi_2Se_3 case (the same as the black dots in figure 5.3.6).

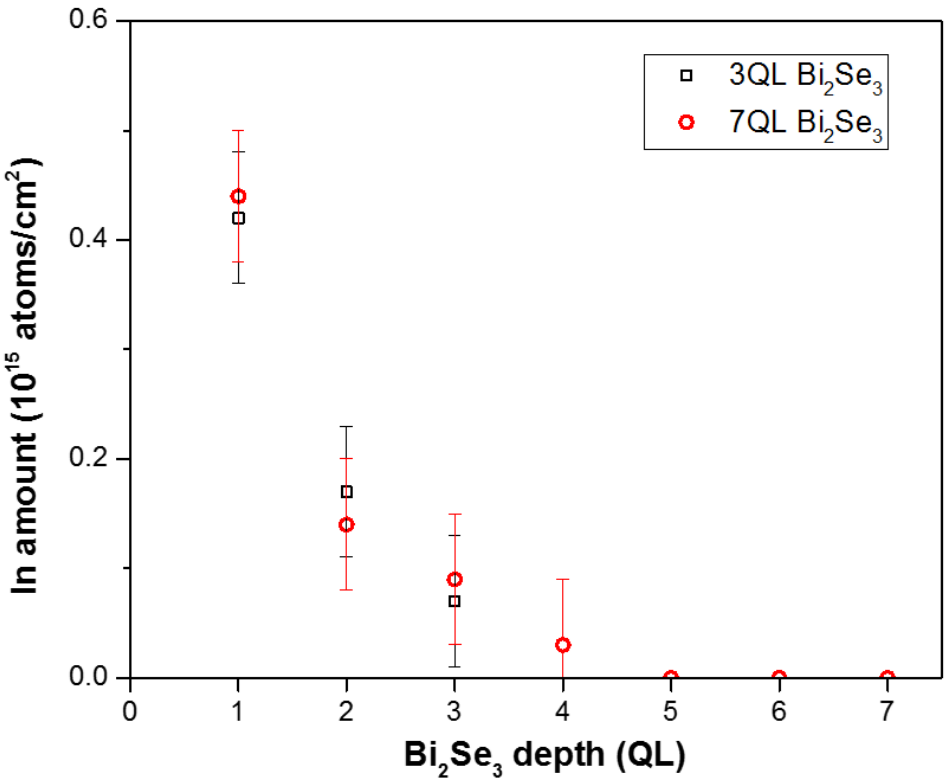

Figure 5.3.8, layer by layer depth profile of Indium diffuses in to the 7QL Bi_2Se_3.

The indium diffusion profile for the In_2Se_3 grown on 7QL Bi_2Se_3 is the same as for the 3QL Bi_2Se_3 case in the first 3QL Bi_2Se_3. After the 4th QL, the indium amount is negligible.

5.4 Conclusions

We have grown In_2Se_3/Bi_2Se_3 thin films on sapphire by Molecular Beam Epitaxy at three different temperatures. Medium Energy Ion Scattering measurements showed that the higher growth temperature resulted in more indium diffusion while our transport measurements showed that the Bi_2Se_3 mobility increases as the amount of indium diffused into Bi_2Se_3 decreases. The mobility of the Bi, Se and In intermixing layer at the In_2Se_3/Bi_2Se_3 interface shows similar indium content dependence as the $(Bi_{1-x}In_x)_2Se_3$ reported [10].

References:

1. Moore, J.E., *The birth of topological insulators.* Nature, 2010. **464**(7286): p. 194-198.
2. Hasan, M.Z. and C.L. Kane, *Topological insulators.* Reviews of Modern Physics, 2010. **82**(4): p. 3045-3067.
3. Kane, C.L. and E.J. Mele, *A New Spin on the Insulating State.* Science, 2006. **314**(5806): p. 1692-1693.
4. Kane, C.L. and E.J. Mele, *Quantum Spin Hall Effect in Graphene.* Physical Review Letters, 2005. **95**(22): p. 226801.
5. Min, H., J.E. Hill, N.A. Sinitsyn, B.R. Sahu, L. Kleinman, and A.H. MacDonald, *Intrinsic and Rashba spin-orbit interactions in graphene sheets.* Physical Review B, 2006. **74**(16): p. 165310.
6. Bernevig, B.A., T.L. Hughes, and S.C. Zhang, *Quantum spin Hall effect and topological phase transition in HgTe quantum wells.* Science, 2006. **314**(5806): p. 1757-61.
7. Bernevig, B.A., T.L. Hughes, and S.-C. Zhang, *Quantum Spin Hall Effect and Topological Phase Transition in HgTe Quantum Wells.* Science, 2006. **314**(5806): p. 1757-1761.
8. Emziane, M., S. Marsillac, and J.C. Bernède, *Preparation of highly oriented α-In2Se3 thin films by a simple technique.* Materials Chemistry and Physics, 2000. **62**(1): p. 84-87.

9. Jiping Ye, Sigeo Soeda, Yoshio Nakamura, and Osamu Nittono, *Crystal Structures and Phase Transformation in In2Se3 Compound Semiconductor.* Japanese Journal of Applied Physics, 1998. **37**(8R): p. 4264.
10. Brahlek, M., N. Bansal, N. Koirala, S.-Y. Xu, M. Neupane, C. Liu, M.Z. Hasan, and S. Oh, *Topological-Metal to Band-Insulator Transition in (Bi(1-x)In(x))2Se3 Thin Films.* Physical Review Letters, 2012. **109**(18): p. 186403.
11. Bansal, N., Y.S. Kim, E. Edrey, M. Brahlek, Y. Horibe, K. Iida, M. Tanimura, G.-H. Li, T. Feng, H.-D. Lee, T. Gustafsson, E. Andrei, and S. Oh, *Epitaxial growth of topological insulator Bi2Se3 film on Si(111) with atomically sharp interface.* Thin Solid Films, 2011. **520**(1): p. 224-229.
12. van der Pauw, L.J., *A method of measuring specific resistivity and Hall effect of discs of arbitrary shape.* Philips Research Reports, 1958. **13**: p. 1–9.
13. Ziegler, J.F., J.P. Biersack, and U. Littmark, *The Stopping and Range of Ions in Solids*. 1985: Pergamon.
14. Kido, Y. and T. Koshikawa, *Ion scattering analysis programs for studying surface and interface structures.* Journal of Applied Physics, 1990. **67**(1): p. 187-193.
15. Frenken, J.W.M., R.M. Tromp, and J.F. van der Veen, *Theory and simulation of high-energy ion scattering experiments for structure analysis of surfaces and interfaces.* Nuclear Instruments and Methods in Physics Research Section B: Beam Interactions with Materials and Atoms, 1986. **17**(4): p. 334-343.